VON KARMAN INSTITUTE FOR FLUID DYNAMICS
TURBOMACHINERY AND PROPULSION DEPARTMENT

UNIVERSITÉ CATHOLIQUE DE LOUVAIN
DEPARTMENT SCIENCES DE L'INGÉNIEUR

Ph.D. Dissertation - Giulia Dell'Era

Experimental characterization of instability onsets in a high speed axial compressor

April 25, 2017

"Accadono cose che sono come domande.
Passa un minuto oppure anni, e poi la vita risponde."

A. Baricco

Acknowledgements

During these years spent at VKI I had the chance to meet a number of fantastic people, who I would like to acknowledge, not only for their contribution in this project, but also, and especially, for their presence.

Without any doubt, the first "thank you" goes to my parents and my family, for being a rock solid reference for me, and for your continuous and loving support. And I feel very grateful to all my friends too: during these years you made my life lighter, in a lot of different ways. I am happy to have met you, and I am glad to have you as friends.

A sincere and big acknowledgement goes to Prof. Paolo Gaetani, for always being a reference in my working path and encouraging me in my career.

I would like to thank also Prof. Jean-Francois Brouckaert: without you I would not have started this project, nor enter the world of the compressors aerodynamics. Thank you for giving me this opportunity.

This thesis would not exist without the "Dream team": in alphabetical order Prof. Tony Arts, Prof. Fabrizio Fontaneto and Prof. Xavier Ottavy. I am just glad to have worked with you, you have always been capable of putting me back on the good track when I lost it, and I am grateful for giving me advises, guiding me in the project, but especially for putting your trust in me.

I also have to thank my VKI colleagues for their contribution in this work, and the LMFA team. Despite the small time spent in Lyon it was really easy to be involved in the team, and to become friends.

Last, but not least, my acknoledgements go to the members of the jury: Philippe Chatelain, Laurent Delannay and Stephane Hiernaux, for their precious advises.

To all of you, thanks.

Giulia
Brussels, 2017

Abstract

The last years have seen a considerable growth of the aviation sector together with more severe environmental constraints. In order to reduce the environmental footprint of aircrafts, a higher efficiency is demanded to engines, leading to more loaded compressor stages, being therefore more prone to stall. Rotating stall and surge are carefully avoided as they reduce the performance of the machine and affect its structural integrity. Since these phenomena appear at the limit of the stable operating range, they have to be taken into account in the design of a new stage. CFD predictions still differ from the actual stall occurrence, deriving the necessity for the experimental characterization of any new compressor stage.

This PhD thesis aims at providing an extensive experimental characterization of the stable and unstable operating range of a high speed low pressure axial compressor stage. The outcomes of the present research will shed light on the mechanisms leading this machine to stall and they will therefore contribute to the improvement of its design methodology with respect to its stability limit. Since a detailed characterization of the unstable range is only possible through the knowledge of the flow structures appearing at stable operating conditions, the stable operating range is also deeply investigated.

The global performance of the stage is defined at first with time-averaged measurements. The detailed description of the flow field in a stable regime is then provided with the time-resolved measurements: a typical blade passage is investigated by applying the phase locked average technique to the data acquired on the rotor casing and at the rotor outlet. What emerges is that the rotor is hub loaded and that the tip leakage flow remains in the blade passage also at near stall condition. The hub corner separation is likely to develop into hub corner stall, whereas the tip region is the most affected by losses, which appear to be due to both the tip leakage flows and rotating instabilities. The flow field at the stator outlet is also represented and shows a lower impact on the stage pressure ratio.

The time-resolved data related to the unstable conditions have been acquired while continuously closing the throttling valve from the near stall operating point and quickly reopening it when the stage enters in stall condition. Five speed lines have been investigated and various stall inception patterns appear at each rotational speed. The compressor stage tested exhibits an abrupt stall inception behavior at higher speeds, while modal waves dominate the lower rpm range. Modal waves are affected by an acoustic mode of the facility, resulting therefore to be modulated by a low frequency component at first, and then to become continuous. One of the speed lines investigated presents a sadle type characteristic with a second stability zone

preceding the flow breakdown. The post-stall behavior is characterized: only one stall cell occupying approximately 50% of the annulus and travelling at around 20% of the rotational speed appears at all the rotational speeds investigated. The stall cell shape is shown in its radial, circumferential and axial extension, highlighting the presence of defined flow patterns at the rotor inlet.

The analysis of the experimental data results to be useful to improve not only the blade design, but also the analysis tools to employ for the conception of new compressors. Ameliorations are proposed for the experimental set-up, and for the application of numerical tools utilized for the definition of the aerodynamic and mechanical design.

List of Publications

List of journal publications

G. Dell'Era, M. Mersinligil, J.-F. Brouckaert

Assessments of unsteady pressure measurements uncertainty - Part 1: Single Sensor Probe, Journal of Engineering for Gas Turbine and Power 2015, vol. 138(4), 041601

(Presented at ASME Turbo Expo 2015 - Paper GT2015-42608)

G. Dell'Era, M. Mersinligil, J.-F. Brouckaert

Assessments of unsteady pressure measurements uncertainty - Part 2: Virtual three hole probe, Journal of Engineering for Gas Turbine and Power 2015, vol 138(4), 041602

(Presented at ASME Turbo Expo 2015 - Paper GT2015-42615)

G. Dell'Era, N. Habotte, J. Desset, J.-F. Brouckaert, S. Hiernaux

Experimental characterization of stall phenomena in a single stage low pressure axial compressor stage, Journal of Power and Energy 2015, vol. 229(5), 549-559

(Presented at ETC11)

List of conference publications

J. Sans, G. Dell'Era, J. Desset, J.-F. Brouckaert, S. Hiernaux

Time-resolved measurements of the unsteady flow field in a single stage low pressure axial compressor, ASME Turbo Expo 2013, San Antonio, TX, USA - June 2013

J. Sans, G. Dell'Era, J. Desset, J.-F. Brouckaert, S. Hiernaux

Performance testing of a low pressure compressor, European Turbomachinery Conference 2013, Lapeeranta - Finland, April 2013

Contents

Nomenclature **xxi**

1. Introduction **1**
1.1. Context . . . 1
1.2. Motivation: the Dream test section . . . 3
1.3. Literature survey . . . 5
1.3.1. Aircraft engines . . . 5
1.3.2. Aerodynamic structures present in a compressor . . . 9
1.3.3. Aerodynamic instabilities . . . 12
1.4. Objective . . . 27
1.5. Methodology and Thesis organization . . . 29

2. Experimental set-up **31**
2.1. VKI-R4 facility . . . 31
2.1.1. The facility . . . 31
2.1.2. Dream test section . . . 31
2.1.3. The experimental set-up . . . 33
2.2. Uncertainty calculation method . . . 34
2.3. Time-averaged measurements . . . 35
2.3.1. Pressure measurements and uncertainty . . . 35
2.3.2. Temperature measurements and uncertainty . . . 37
2.3.3. Efficiency measurements and uncertainty . . . 39
2.4. Time-resolved measurements . . . 39
2.4.1. Fast-response pressure probe . . . 39
2.4.2. Wall fast-response pressure sensors . . . 52
2.5. Measurements employed as reference for the blade row numerical characterization . . . 54
2.5.1. Temperature measurements . . . 54
2.5.2. Pressure measurements . . . 54
2.5.3. Global performance assessments . . . 58

3. Characterization of the stable operating range **59**
3.1. Experimental set-up employed in the stable operating points 59
3.2. Global performance of the stage . . . 61
3.2.1. Performance map . . . 61
3.2.2. Performance of the single blade rows . . . 62
3.3. Detailed characterization of the flow field . . . 75
3.3.1. Rotor flow field description . . . 75
3.3.2. Stator flow field description . . . 88

3.4. Conclusions 91

4. Characterization of the unstable operating range 93
4.1. Experimental set-up adapted to the unstable range 93
4.2. Overview on the unstable range 95
4.2.1. Frequency analysis 101
4.3. Stall inception 105
4.3.1. Characterization of the instabilities 105
4.3.2. Explanation of the low frequency component 111
4.3.3. Redistribution of the flow field at 80% rpm 117
4.4. Characterization of the stall cell 120
4.4.1. Number of stall cells 120
4.4.2. Shape of the stall cell 122
4.5. Conclusions 134

5. Conclusions 137
5.1. Conclusions 137
5.2. Future perspectives 139

Appendices 143

A. Uncertainty calculation method 145

B. Post-processing techniques 149
B.1. Phase-locked average 149

Bibliography 153

List of Figures

1.1. Real Joule-Brayton cycle in an enthalphy - entropy diagram and performance of the real cycle [1]. 2
1.2. Compressor performance map, unstable range classification according to Day [2] for multi-stage axial compressors. 3
1.3. Experimental performance map comparing the Dream baseline blade with its optimized version. 4
1.4. Typical jet engine and trends for the various flow quantities [3]. 5
1.5. Ideal Joule cycle [4]. 5
1.6. Turbofan [4] and open rotor architecture. 6
1.7. Efficiency of the different engines architectures [3]. 6
1.8. Compressor stage, velocity triangles [5]. 7
1.9. Sketch of a direct drive turbofan engine. 8
1.10. Top: Tip clearance flow as sketched in Vavra [6]. Bottom: Correspondence between three-dimensional steady tip clearance flow and unsteady-two dimensional flow [7]. 10
1.11. casing static pressure ensemble average and standard deviation plots for varying tip clearance (ξ) and last stable operating point (Φ) [8]. 10
1.12. Endwall and suction surface streamlines showing 3D separated flow [9]. 11
1.13. Hub and vane suction side flow visualization at various blade loadings [10]. 11
1.14. Propagation mechanism of the rotating instabilities [11]. . . . 13
1.15. Top: Spectrum of pressure measurements retrieved in presence of rotating instabilities, the modes are highlighted [12]. Central: typical spectrum retrieved with rotating instabilities [13] at different operating conditions (ϕ denotes the mass flow coefficient). Bottom: comparison between a spectrum retrieved in a shrouded rotor and a rotor with a tip gap [13]. 14
1.16. Compressor performance map of the machine showing mild stall [14]. 15
1.17. Time-resolved pressure signals near rotor leading edge in mild stall condition (corresponding to flow range A in Figure 1.16) and rotating stall one (corresponding to flow range C in Figure 1.16) [14]. 16
1.18. Flow mechanism of mild stall [15]. 16
1.19. Stall propagation mechanism [16], [17]. 17
1.20. Stalled and unstalled characteristic [18]. 18
1.21. Spikes and modal stall inception on the characteristic [19]. . . 19

1.22. Spike stall inception traces retrieved with sensors located near the leading edge of the blades in seven circumferential positions [20]. 20
1.23. The vortical structure and the formation of spikes [21]. 20
1.24. Effect of velocity perturbation on the wake size [16]. 21
1.25. Comparison between the predicted and the measured first harmonic of the axial velocity in the time evolution (left) and the spectrum (right) [22]. 22
1.26. Sketch of the flow lines retrieved across a stall cell in the absolute frame [18]. 23
1.27. Typical total pressure measurements retrieved in a stall cell at different rotational speeds (identified with different mass flow coefficients ϕ^*) [18]. In this case the data presented are acquired up- and down-stream the first rotor of a three stage configuration (respectively measuring planes 2 and 3). 24
1.28. Left: Pressure differences across the blade rows [23], Right: Outer wall static pressure inside a stall cell [24]. 25
1.29. Flow patterns on the meridional plane for different circumferential locations inside a stall cell [24]. 26
1.30. Left: typical performance map during surge [2], Right: typical time resolved signal retrieved during surge and comparison with rotating stall [25]. 28
1.31. Sketch of a typical compression system [26]. 28

2.1. Sketch of the VKI-R4 facility. 31
2.2. Dream test section, the measuring planes (0, 1, 2, 3, 4) are shown in the left Figure. 33
2.3. Circumferential locations in the test section in which it is possible to perform radial traversing. 34
2.4. Photo of the rakes, recovery factor of the inlet and the outlet rakes. 38
2.5. Left: AP1-FP3 fast-response total pressure probe head. Right: Active compensation amplifier circuit diagram. 40
2.6. Typical spectrum retrieved with the FP3 probe in the VKI-R4 facility. 41
2.7. Acoustic propagation of waves on the probe head in the bandwidth 120-220 kHz. 41
2.8. Temperature (left) and pressure (right) calibration surface fits – dots indicating actual calibration points 43
2.9. Right: Illustration of yaw and pitch axes of a pressure probe. Left: Pressure recovery coefficient of the AP1-FL3 at M=0.7. 45
2.10. Pressure recovery coefficient of the AP1-FL3 at M=0.7 together with expanded calibration uncertainties. 46
2.11. Histogram of example PLA classes for data acquired at midspan (left) and at tip region (right). 48

2.12. Normal probability plot of example PLA classes for data acquired at mid-span (left) and at tip region (right). 48
2.13. P_{RMS} (left) and expanded uncertainty (right) maps (left) of the PLA presented over two blade passages. 49
2.14. The derived aerodynamic calibration curve (expressed in terms of C_{p_0}, defined in equation 2.27) of the virtual three-hole mode probe at M=0.7. 50
2.15. Typical spectrum retrieved with the FP3 probe in the VKI-R4 facility. 51
2.16. Shallow cavity feedback to the Rossiter modes [27]. 51
2.17. Fast-response pressure sensors configuration and insert. . . . 53
2.18. Typical spectrum retrieved in the R4 facility with the fat-response pressure sensors on the casing. 53
2.19. Recovery factor calibration for the thermocouple probes employed in plane 1 and plane 4. 55
2.20. Left: Kiel pressure probe. Right: Kiel probe angular calibration. 56
2.21. Three-hole pressure probe. 56
2.22. Three-hole probe calibration coefficients K_{yaw} and K_{tot}. . . . 57

3.1. Left: sketch of the rotor outlet traversing. Right: measurement location along the radius at the rotor outlet. 60
3.2. Sketch of the measurement matrix retrieved at the stator outlet with the circumferential and radial traversing of the fast response pressure probe. 60
3.3. Stage total to static performance map retrieved with the rakes in the stable operating points. 61
3.4. Stage total to total performance map retrieved with the rakes in the stable operating points. 62
3.5. Numerical domain employed in the simulations. 63
3.6. Mesh sensitivity analysis and grid chosen (red circle). 64
3.7. Grid employed on the stage and zoom on the rotor blade row. 66
3.8. Inlet distributions employed as boundary conditions in the simulations, respectively total pressure (a), total temperature (b) and turbulent viscosity(c). 68
3.9. Comparison of measured and the computed total pressure distribution at the rotor outlet at design and near stall conditions at 100% Nn. 69
3.10. Top: Total pressure radial distribution at 100% Nn design operating condition retrieved numerically in the four measuring plane. Bottom: Total pressure radial distribution at 100% Nn near stall operating condition retrieved numerically in the four measuring plane. 70

3.11. Top: Total temperature radial distribution at 100% Nn design operating condition retrieved numerically in the four measuring plane. Bottom: Total temperature radial distribution at 100% Nn near stall operating condition retrieved numerically in the four measuring plane. 71

3.12. Top: Flow angle radial distribution at 100% Nn design operating condition retrieved numerically in the four measuring plane. Bottom: Flow angle radial distribution at 100% Nn near stall operating condition retrieved numerically in the four measuring plane. 72

3.13. Top: Entropy radial distribution at 100% Nn design operating condition retrieved numerically in the four measuring plane. Bottom: Entropy radial distribution at 100% Nn near stall operating condition retrieved numerically in the four measuring plane. 73

3.14. T-s diagram retrieved numerically at midspan at 100% rpm, design operating condition. 74

3.15. Total pressure phase locked average (PLA) map and corresponding RMS of the rotor outlet flow field at 100% Nn, design operating condition. 77

3.16. Total pressure phase locked average (PLA) map and corresponding RMS of the rotor outlet flow field at 100% Nn, near stall operating condition. 77

3.17. Total pressure skewness map and kurtosis of the rotor outlet flow field at 100% Nn, design operating condition. 78

3.18. Total pressure skewness map and kurtosis of the rotor outlet flow field at 100% Nn, near stall operating condition. 78

3.19. Rotor outlet total pressure at midspan, comparison between the raw signal (top) and phase locked average (bottom). . . . 79

3.20. Absolute Mach number distribution retrieved numerically on the rotor blade on the suction side (left) and on the pressure side (right). 79

3.21. Left: NASA rotor exit pressure ratio near tip (R/Rt = 0.91) for rotor as whole(A), an individual blade passage (B), and ensemble average of that individual blade passage [28]. Right: Same as Left, but for rotor hub (R/Rt = 0.68) [28]. 80

3.22. Phase locked averaged casing static pressure distribution and corresponding RMS at 100% Nn, design operating condition. The grid indicates the axial location of the sensors. 83

3.23. Phase locked averaged casing static pressure distribution and corresponding RMS at 100% Nn, near stall operating condition. 83

3.24. Top: Time resolved static pressure signal at the rotor inlet at 100% Nn, design operating condition. Bottom: Instantaneous static pressure distribution on the rotor casing at 100% Nn, design operating condition, and corressponding zoom on two blade passages. The grid indicates the axial location of the sensors. 84
3.25. Top: Time resolved static pressure signal at the rotor inlet at 100% Nn, near stall operating condition. Bottom: Instantaneous static pressure distribution on the rotor casing at 100% Nn, near stall operating condition, and corressponding zoom on two blade passages. 85
3.26. Standard deviation of static pressure and instantaneous axial velocity contours at rotor tip, at near stall condition in a one and half stage [29]. 86
3.27. Spectra of different sensors on the rotor casing at design (a), near stall (b) and stall (c) operating conditions. 87
3.28. Stator outlet total pressure (time averaged) and corresponding RMS. 89
3.29. Instantaneous values of stator outlet total pressure and corresponding RMS for three subsequent times. 90

4.1. Fast response pressure sensors axial and circumferential disposition. 94
4.2. Radial disposition of the sensors and probe FP3. 94
4.3. Stage static-to-total performance map retrieved with the rakes. 95
4.4. Stage total-to-total performance map retrieved with the rakes. 95
4.5. Time-resolved pressure signal at the casing rotor inlet, static-to-total performance map. 97
4.6. Time-resolved pressure signal at the casing rotor inlet, static-to-total performance map. 98
4.7. Time resolved pressure signals (low-pass filtered at 50 Hz) at 85% Nn. 99
4.8. Zoom of the time resolved pressure signals (low-pass filtered at 50 Hz) at 85% Nn shown in Figure 4.7 in the part highlighted in red. 100
4.9. Time-resolved signals (low pass filtered at 50Hz) and corresponding wavelet transformations for the cases 100% (top) and 90% Nn (bottom). 102
4.10. Time-resolved signals (low pass filtered at 50Hz) and corresponding wavelet transformations for the case 85% Nn, at the stall inception (top) and during the whole transient(bottom). 103
4.11. Time-resolved signals (low pass filtered at 50Hz) and corresponding wavelet transformations for the case 80% Nn, at the stall inception (top) and during the whole transient(bottom). 104

4.12. Ensemble average of the signals at the rotor outlet at hub, midspan and tip at choke (left) and near stall (right) condition. 105
4.13. Raw signal at hub and midspan corresponding to Part A (left) and part B (right) of the signal shown in Figure 4.7. 106
4.14. Zoom on the raw signals presented in Figure 4.13. 106
4.15. Zoom around the BPF of the spectra retrieved for Part A (left) and Part B (right) of Figure 4.7. 107
4.16. Carpet plot of the modulated modal waves at 85% Nn (bottom), the corresponding raw signal at the rotor inlet (K14) is presented on top. 109
4.17. Carpet plot of the continuous modal waves at 85% Nn (bottom), the corresponding raw signal at the rotor inlet (K14) is presented on top. 110
4.18. Time resolved total pressure signal (top) retrieved during the stall transient at 90%, 85% and 80% Nn and corresponding spectrum (bottom) obtained for the pert of the transient in which the low frequency component appears (in blue in the top graphs). 112
4.19. Time resolved pressure signals low-pass filtered at 50 Hz retrieved at 85% Nn, in the condition where the low frequency component appears. 113
4.20. Top: time-resolved static pressure signals retrieved with K14, K7 and K15 low pass filtered at 10 Hz. Bottom: top view of the 3D plot presented on the right. 114
4.21. Maxima of the curves shown in Figure 4.20, in black. The maxima of equivalent curves retrieved with the other sensors on the casing are also represented. 115
4.22. Corresponding representation of the one of Figure 4.21 for the shifted signals. 116
4.23. Signal retrieved at the casing rotor inlet (K14, top) in the second stability zone at 80% Nn and corresponding wavelet transformation (bottom). 117
4.24. a: Signal retrieved at the casing rotor outlet (K15, top) in the second stability zone at 80% Nn and corresponding wavelet transformation (bottom). b: Signal retrieved at midspan rotor outlet (FP3, top) in the second stability zone at 80% Nn and corresponding wavelet transformation (bottom). c: Signal retrieved at hub rotor outlet (KFP3hA, top) in the second stability zone at 80% Nn and corresponding wavelet transformation (bottom). 118
4.25. Signal retrieved at hub stator outlet (KFP4h, top) in the second stability zone at 80% Nn and corresponding wavelet transformation (bottom). 119

4.26. Top: Time resolved static pressure signal at the rotor inlet at 80% Nn, second stability zone. Bottom: Instantaneous static pressure distribution on the rotor casing at 80% Nn, second stability zone. 119
4.27. Graphic method to determine the number of cells. 121
4.28. Time-resolved pressure signal and interval to which the phase average has been applied. 123
4.29. Probe signal division for phase average computation. 124
4.30. Phase locked average of the stall cell retrieved at the rotor outlet at tip (K15), at midspan (FP3) and hub (KFP3hA) and corresponding RMS, skewness and kurtosis. 125
4.31. Phase locked average of the stall cell retrieved at the casing rotor inlet (K14) and corresponding RMS, skewness and kurtosis. 126
4.32. Phase locked average of the stall cell retrieved at the hub stator outlet (KFP4h) and corresponding RMS, skewness and kurtosis. 127
4.33. Top: Raw signal retrieved at the casing rotor inlet (top), and casing static pressure contour plot retrieved during rotating stall. The revolutions represented in the contour plot are highlighted in green in the raw signal. Bottom: zoom on revolution 832. 128
4.34. "Variation of ensemble-averaged pressure distribution on the casing" in the case presented by Inoue [14]. 129
4.35. Signal retrieved at casing rotor inlet (K14, top) during rotating stall at 85% Nn and corresponding wavelet transformation (bottom). 130
4.36. a: Signal retrieved at casing rotor outlet (K15, top) during rotating stall at 85% Nn and corresponding wavelet transformation (bottom). b: Signal retrieved at casing rotor outlet (FP3, top) during rotating stall at 85% Nn and corresponding wavelet transformation (bottom). c: Signal retrieved at casing rotor outlet (KFP3hA, top) during rotating stall at 85% Nn and corresponding wavelet transformation (bottom). 131
4.37. Signal retrieved at hub stator outlet (KFP4h, top) during rotating stall at 85% Nn and corresponding wavelet transformation (bottom). 132
4.38. Principle sketch of the shape of the cell up- and downstream the rotor, and across it. 132
4.39. Pressure differences across the blade rows. 133

A.1. Student's t distribution for 95% confidence interval with respect to degrees of freedom. 147

B.1. Top: Division of the pressure data in blade passages. Bottom: the PLA calculated value for one class in a blade passage. . . 150
B.2. Phase locked average and corresponding RMS variation for different number of classes employed across a blade passage. . 151

List of Tables

2.1. Quantities characterizing the stage. 32

3.1. Mesh sensitivity analysis. 65
3.2. RANS - NLH comparison. 65

4.1. Stall cell characteristics. 122

Nomenclature

Roman Symbols

0	Total Quantity, Measurement in axial location 0	
1	Measurement in axial location 1	
2	Measurement in axial location 2	
3	Measurement in axial location 3	
4	Measurement in axial location 4	
A	Area	
a	Speed of sound	
b	Systematic uncertainty	
B	Burner	
C	Compressor	
c	Absolute velocity	
C_p	Isobaric specific heat	$[J/(kgK)]$
C_{p_0}	Pressure recovery coefficient	
h	Enthalpy	[J]
K	Number of data fit coefficients	
L	Length	
$\dot{m}$	Mass flow rate	$[kg/s]$
N	Number of points	
P	Axial measurement plane	
P	Pressure	[Pa], [mbar]
Q	Thermal energy	[J]
R	Radius	[m]
r	Recovery ratio	
r	Radial direction	[m]
Re	Reynolds number	
s	Entropy	$[J/(kgK)]$
s	Random uncertainty	
St	Strouhal number	
t	Student t distribution	
T	Temperature	[K]
T	Turbine	
t_{95}	value of the student-t distribution for 95% confidence interval	
u	Peripheral Velocity	$[m/s]$
U	Uncertainty	
V	(Absolute) Velocity	$[m/s]$
V	Volume	$[m^3]$

V	Probe output	[V]
W	Relative Velocity	$[m/s]$
X	Individual values	
z	Axial direction	[m]

Greek Symbols

α	Absolute yaw angle	[deg]
β	Relative yaw angle	[deg]
β	Pressure ratio	
χ	Degree of reaction	
Δ	Difference	
η	Efficiency	
μ	Dynamic viscosity	[Pa s]
μ	Mean value	
ν	Kinematic viscosity	$[m^2/s]$
ν	Degrees of freedom	
ϕ	Flow coefficient	
ψ	Loading coefficient	
χ	Degree of reaction	
ω	Rotation	
ω	Frequency of the compressing system	[Hz]
ρ	Density	$[kg/m^3]$
σ	Variance	
θ	Tangential direction	

Subscript

0	Cruise condition
95	95% confidence interval
b	Related to systematic uncertainty
C	Compressor
C	Central
c	Related to the pipe of the compressing system
$calib$	Calibration
CR	Cell rotation
d	Downstream
$design$	Design operating points
in	Inlet
j	Thermocouple junction
L	Left
$meas$	Measurement

o	Overall
OCS	Oscillation
p	Plenum
out	Outlet
R	Right
red	Reduced
ref	Reference value
RMS	Root Mean Square
rev	Rotor revolution
s	Related to random uncertainty
s	Static quantity
T	Total quantity
T	Turbine
t	Tangential
th	Thermal
u	Upstream
x	Axial

Acronyms

BL	Boundary Layer
BPF	Blade Passing Frequency
CFD	Computational Fluid Dynamics
CH	Choke operating condition
DE	Design operating condition
EA	Ensemble Average
FHV	Fuel Heat Value
HCV	Hub Corner Vortex
HPC	High Pressure Compressor
IGV	Inlet Guide Vane
HPF	High Pass Filtered
LE	Leading Edge
LPF	Low Pass Filtered
NLH	Non-linear Harmonic
Nn	Shaft speed
NS	Near stall operating condition
PLA	Phase Locked Average
PS	Pressure Side
PSD	Power Spectrum Density
R	Rotor
RI	Rotating Instabilities
RMS	Root Mean Square
SC	Stall Cell

SEE	Standard Estimate of Error
SFC	Specific Fuel Consumption
S	Stator
SS	Suction Side
TC	ThermoCouple
TE	Trailing Edge
TLF	Tip Leakage Flows
TLV	Tip Leakage Vortex
Tu	Turbulence intensity
VKI	von Karman Institute for Fluid Dynamics

Chapter 1.

Introduction

1.1. Context

More than one hundred years have passed since the first flight has been performed. At that time the Wright brothers were targeting a self sustained mean of transport, able to fly. The nowadays scenario has undergone radical changes: "air transport moves over 2.2 billion passengers annually" and "worldwide, it is estimated that the equivalent of 1300 new international airports will be required by 2050 with a doubling in the commercial aircraft fleet" [30]. Moreover such a growth is subjected to environmental constraints.

The Paris Agreement, signed last April, represents a "historical turning point" for the reduction of global warming (as said by France's foreign minister) and covers all the trading systems including aviation [31]. The Paris Agreement therefore sets a worldwide frame for ongoing European projects such as Cleansky. The Advisory Council for Aeronautical Research in Europe (ACARE) since 2001 defines a reduction of CO_2 by 50% and of NO_x by 80% by 2020, together with the progressive diminution of the environmental impact of the airplane lifecycle [32].

The emissions reduction represents therefore a major objective of the aerospace research, where a significant contribution is due to the improvement of the engine efficiency. How to reach this target? One possible solution can be found through the analysis of the thermodynamic cycle on which aircraft engines are based: the Joule-Brayton cycle, presented in Figure 1.1. As the efficiency of the ideal Joule-Brayton cycle is a function of the pressure ratio, a higher pressure ratio directly yields a higher efficiency (Figure 1.1, right). So far one or more cycle parameters were optimized at a time, however the actual environmental limitations impose ameliorations regarding all the parameters and new strategies have to be undertaken.

The turbomachinery community is presently facing the big challenge of increasing the cycle efficiency regarding the pressure ratio. The tendency is to reduce the airplane weight as much as possible, therefore a reduced number of stages is more appealing, requiring more loaded stages (possibly with a lower number of blades). A loaded stage though is more keen to stall, and will be able to operate in a narrower range.

Stall is a phenomenon which defines the stability limit (or "surge line") of

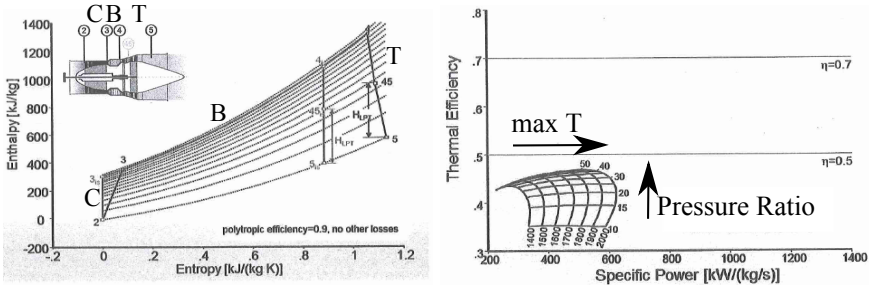


Figure 1.1.: Real Joule-Brayton cycle in an enthalphy - entropy diagram and performance of the real cycle [1].

a compressor. As classified by Day (Figure 1.2 [2]), once exceeded the surge line two different phenomena may take place according to the rotational speed: surge will appear at high regimes, and stall at lower regimes, which can be distinguished in part span or full span. Rotating stall and surge are working conditions that want to be accurately avoided, as they may cause severe consequences such as blade vibrations, casing deformation, until endangering the engine itself. They affect both the aerodynamical performance and the structural constraints of a blade, it is thus imperative to take them into account in the design of a new stage.

Various techniques exist to prevent the formation of these phenomena, and they all aim at the extension of the operating range of the compressor. Among the techniques the most employed are: active control, based on real-time assessments during the engine operation, and a stall-wise robust design.

The compressor unstable range has been investigated for more than 75 years, but some open questions still exist and the design of the machines of new generation require a deeper understanding on the rotating stall inception and the post-stall behavior.

CFD represents the most employed analysis tool during the conception phase of a new compressor design. Nevertheless as Denton [33] shows, CFD presents some intrinsic limitations, which for the moment cannot be overcome, and that anyways have a great impact on the decisions taken on a new machine. Day [34] states indeed: “the inability to predict performance gradients near the peak of the characteristic is, however, a hindrance - particularly as it is these gradients which define the stability limits. Work on improving the CFD predictions for flow conditions near the surge line is ongoing, but it is mostly being done by computational specialists without much input from the stall fraternity”.

The only possibility to overcome the limitations of CFD is by experimental testing. Experimental data are indeed presently employed in the design process as an analysis tool:

1. for an indication on the design, concerning the parameters influencing the unstable range: hub/tip ratio, loading, etc.
2. to predict the stability limit and the stall inception mechanisms
3. in the post-stall behavior, for the determination of the degraded performance and how it affects the structural limit of the various engine components

In order to answer all these requirements an adequate testing have to be foreseen in the production cycle of a compressor. As unsteady phenomena take place, time-resolved measurements are the most suitable and the experimental set-up plays a major role for a complete understanding of the unstable regime.

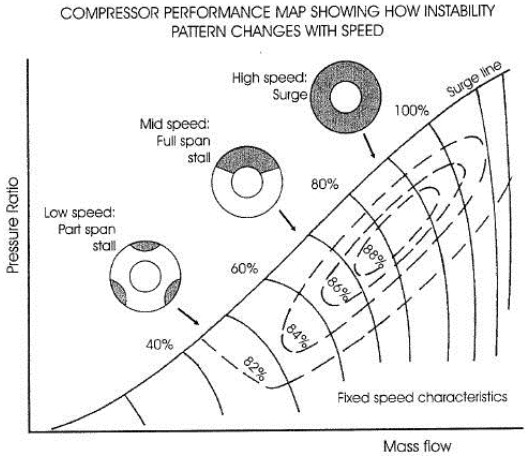


Figure 1.2.: Compressor performance map, unstable range classification according to Day [2] for multi-stage axial compressors.

1.2. Motivation: the Dream test section

The FP7 Dream European project, started in 2008, is in line with the objective targeted by the aero-engine community and studies a "range of completely novel designs for both contra-rotating open rotors and turbofans" [35] in order to fulfill the ACARE requirements regarding noise and CO_2.

In this framework von Karman Institute for Fluid Dynamics, in collaboration with Safran Aero Boosters (former Techspace Aero), tested the first stage of a state-of-the-art booster in order to compare the performance of the original baseline blade with the corresponding optimized version. The aim is indeed the definition of new technologies to be employed in a more loaded compressor stage.

The booster is constituted by typically three or four stages and is located at the core entrance. The radial flow field distribution downstream the fan is skewed, which is not an appropriate condition to start the compression process. The booster has therefore the function to make the flow field uniform in the radial direction. It does not provide a high pressure ratio.

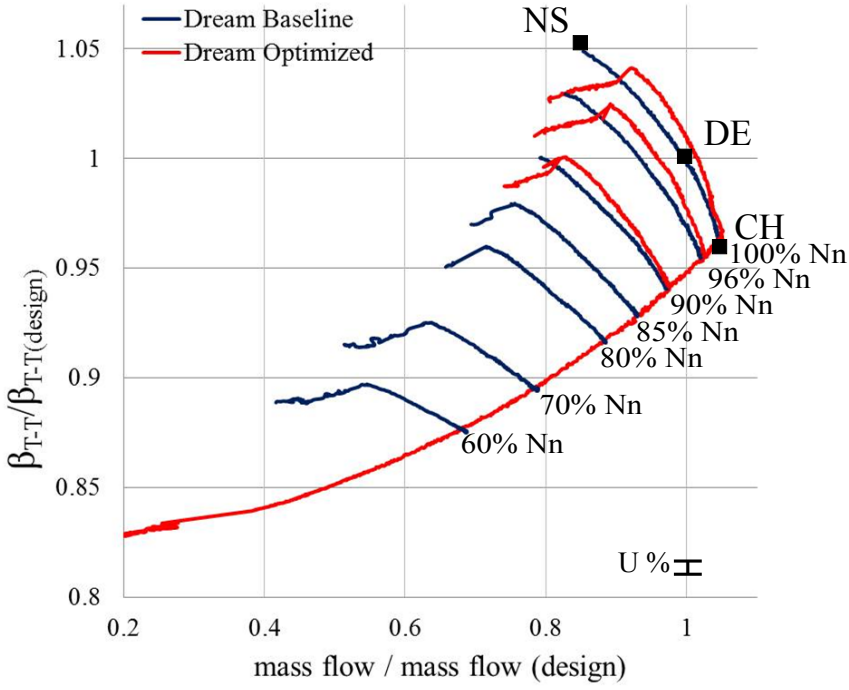


Figure 1.3.: Experimental performance map comparing the Dream baseline blade with its optimized version.

In the case studied a 1.5 stage of a modern booster design was investigated, with the purpose to get a better acquaintance on some technological improvements to apply on boosters of new generation: the sweep and the hub contouring. The sweep has the aim to improve the blade efficiency, the hub contouring to stabilize the hub region and to distribute the load along the whole span.

Figure 1.3 represents the performance map retrieved with the two blades. Their testing points out that the optimized version:

1. provides an increased pressure ratio in the design operating point, as foreseen by the implementation of the new features

2. has a reduced stall margin with respect to the baseline blade

This outcome highlights the limited knowledge about the booster state-of-the-art technology, both at the surge margin and in the unstable region. The conception is also based on steady state considerations, which need to be improved in order to take into account the unsteady phenomena appearing in the unstable range.

1.3. Literature survey

1.3.1. Aircraft engines

1.3.1.1. Principle and new trends

A jet propulsion engine is based on Newton's third law of motion: an action on a body corresponds to an equal and opposite reaction. In this case the body is the air surrounding the aircraft. The engine has the role to create a big mass of air having a certain velocity, able to thrust the aircraft.

The jet engine is composed of a compressor, a burner and a turbine. The compressor and the burner are energizing the flow in two different ways: the former by increasing its pressure, the latter by increasing its temperature. The turbine exploits the energy of the flow, and as it runs on the same shaft as the compressor, it provides the energy to its functioning. The thrust is finally created by the nozzle. Figure 1.4 shows how the various quantities vary along the engine.

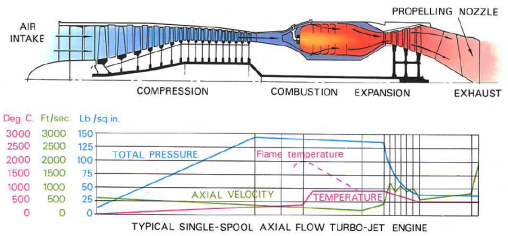


Figure 1.4.: Typical jet engine and trends for the various flow quantities [3].

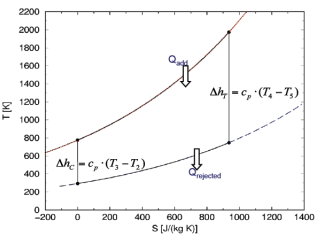


Figure 1.5.: Ideal Joule cycle [4].

As already stated in the Introduction, the thermodynamics of the jet engine is represented by the Joule cycle. The thermal efficiency of the ideal Joule cycle, shown in Figure 1.5, is defined as:

$$\eta_{th} = \frac{Q_{added} - Q_{rejected}}{Q_{added}} = \frac{\Delta h_T - \Delta h_C}{Q_{added}} \tag{1.1}$$

where Δh_T is the energy provided by the turbine, Δh_C is the energy required by the compressor, and Q_{added} represents the heat added by the burner. The thermal efficiency of the cycle can therefore improve by increasing the pressure ratio, as the maximum temperature is fixed not only by the

stoichiometric combustion, but also by the material and the technological constraints utilized to overcome the limitations imposed by the material (e.g. cooling, ...).

The overall efficiency relates the engine useful energy, expressed in terms of airplane cruise velocity V_0, to the specific fuel consumption (fuel mass flow per thrust unit) and the FHV (fuel heat value):

$$\eta_o = \frac{V_0}{SFC \bullet FHV} \tag{1.2}$$

The overall efficiency can also be expressed in terms of thermal efficiency (η_{th} = (energy at the nozzle)/(energy of the fuel)) and propulsive efficiency ($\eta_{propulsive}$ = (useful work of the engine)/(energy at the nozzle)):

$$\eta_o = \eta_{th} \bullet \eta_{propulsive} \tag{1.3}$$

Therefore to a higher thermal efficiency corresponds a lower specific fuel consumption.

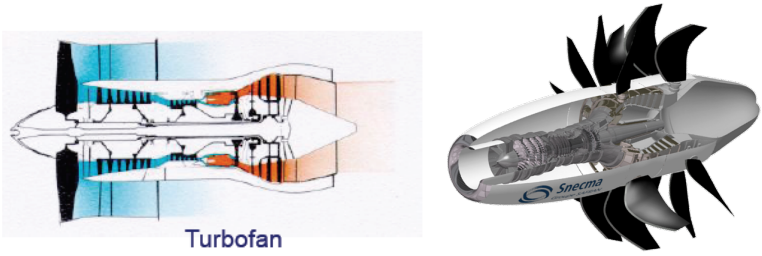


Figure 1.6.: Turbofan [4] and open rotor architecture.

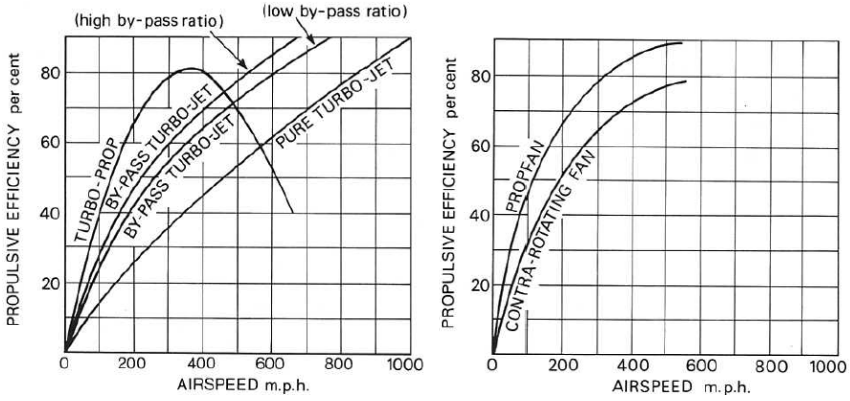


Figure 1.7.: Efficiency of the different engines architectures [3].

The most employed engine architecture is the turbofan engine, which is characterized by an additional flux producing the major part of the thrust. A sketch of a turbofan engine is presented in Figure 1.6, left.

The new architectures are moving towards either a high by-pass ratio or open rotor (Figure 1.6, right), as they are able to function with a higher efficiency, as shown in Figure 1.7.

1.3.1.2. The compressor

A compressor is a machinery built to energize a fluid by increasing its pressure. In the case of a jet engine the fluid is air. Two blade rows typically compose a compressor: the rotor and the stator. Usually the former adds kinetic and pressure energy to the fluid, the latter provides pressure energy. The series of a rotor and a stator blade row is called stage and is represented in Figure 1.8. The allocation of pressure energy across the stage is quantified by the degree of reaction χ, which is the ratio between the static pressure delivered by the rotor ΔP_{Srotor} with respect to the one provided by the whole stage ΔP_{Sstage}: $\chi = \Delta P_{Srotor}/\Delta P_{Sstage}$.

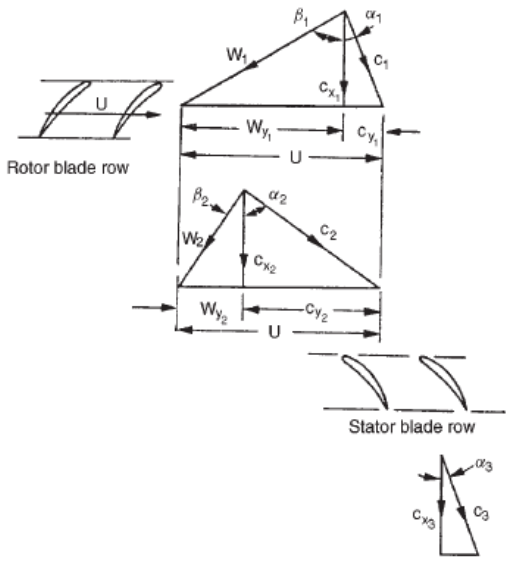


Figure 1.8.: Compressor stage, velocity triangles [5].

The axial flow compressors application is for a higher mass flow range, while the radial machines are utilized for a lower one. Jet engines typically employ axial flow machines, with several stages.

The Euler relation describes the energy provided by the rotor to a streamline passing across it:

$$\Delta h = u(v_{1t} - v_{2t}) \tag{1.4}$$

where: u is the peripheral rotor velocity and v_{1t} and v_{2t} are the tangential velocities across the rotor blade row (in Figure 1.8 they correspond to c_{y_1} and c_{y_2}). Velocity triangles (shown in Figure 1.8) are usually utilized to represent it.

The compressor is required to work in a certain operating range, defined in the preliminary design phase. It is represented on a performance map such as the one shown in Figure 1.2. Each iso-speed line is limited by the choke point at higher mass flows, and by the surge line at low mass flows. As already declared in Chapter 1, rotating stall and surge occur in this region. A more detailed description of these phenomena will be provided in the next section.

The booster

The low pressure compressor, or booster, is located after the fan and it is composed by 3 or 4 stages (see Figure 1.9). As the fan provides a skewed velocity distribution at its root, the booster has the function to supply the core with a uniform flow distribution, not to provide a high pressure ratio as the HPC.

The booster represents the limiting component at partial speed: the rear stages result to be choked, whereas the front ones are not supplied with sufficient air. On the other hand the HPC is more prone to stall at full speed.

Boosters are typically designed towards the choke side, nevertheless a solution to keep the booster in stable conditions at partial speed is the use of bleed at its outlet [36].

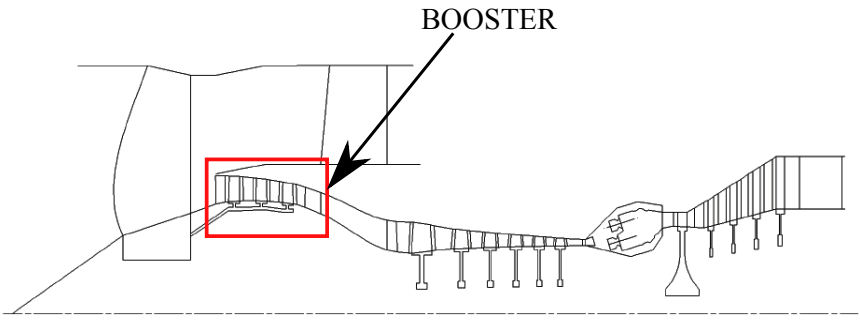


Figure 1.9.: Sketch of a direct drive turbofan engine.

The new engine architectures proposing a high by-pass ratio, imply a lower rotational speed of the fan. As explained by Hiernaux et al. [37], the booster is mechanically coupled to the fan, therefore the pressure ratio reduction linked to the lower speed has to be compensated by a higher loading. The latter can be obtained by either a higher number of stages, leading to an increased weight of the engine (and of fuel consumption), or an increase of

the loading per stage. This solution is preferable, and some studies were undertaken with a specific booster application: Sans [38] investigates the solidity effect, Van de Wyer [39] and Gelmedov et al. [40] analyze the effect of the casing treatments on the casing.

The literature reports very few examples which directly refer to boosters, therefore the specific application will be considered in the next paragraphs if possible, otherwise it will be supplied by other cases having a similar phenomenology.

1.3.2. Aerodynamic structures present in a compressor

In an axial compressor several aerodynamic structures are encountered: secondary flows, wakes, rotor/stator interactions, just to cite some of them. As pointed out by Gbadebo [9], the three-dimensional separations represent the origin of dangerous phenomena such as rotating stall and surge. Their evolution from the stable to the unstable condition has been verified by McDougall et al. [41] and Day [16]. Therefore the attention goes to the flow structures which typically appear in an axial compressor: the tip leakage flows and the hub corner separation. These structures represent also the main contributions to losses in the stable regime.

Tip leakage flows

Tip clearance flows represent one of the loss sources in the rotor blade row [6]. The rotor gap allows a part of the flow field to move from the pressure side to the suction side of the blade producing a leakage flow. As explained in Storer et al. [42], the leakage flow is strongly related to the blade loading and creates a blockage in the tip region of the blade, influencing the incidence along the whole span. The vortex which creates is schematically represented as shown in Figure 1.10, top.

A more detailed description is provided by Chen et al. [7]: adjacent blades have an effect on tip clearance flows, indeed its development in the axial and circumferential directions is due to the chordwise and pitchwise pressure gradients, but also depends on the blade stagger. The representation of its evolution is shown with a three-dimensional flow field and with several two-dimensional flows in Figure 1.10, bottom.

The gap size does not have an impact on the trajectory of the main vortex [7], though it has one on the compressor performance. Marz et al. [8] show that higher gaps make the machine more unstable, i.e. having a more reduced operating range but also a higher fluctuating content. Figure 1.11 provides a representation of the tip leakage flow for different clearances, highlighting the higher unsteadiness for a bigger gap.

Saathoff and Stark [43] propose a detailed study on the tip clearance flow variation according to the incidence: the separation line produced by the vortex is close to the trailing edge at higher flow rates, while it moves forward at higher incidences, until reaching the leading edge at flow rates close to

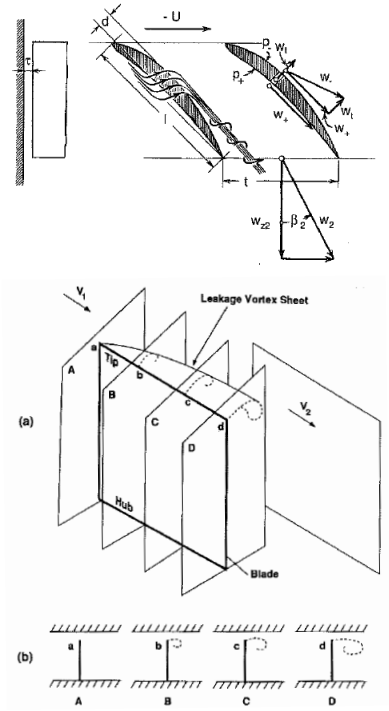


Figure 1.10.: Top: Tip clearance flow as sketched in Vavra [6]. Bottom: Correspondence between three-dimensional steady tip clearance flow and unsteady-two dimensional flow [7].

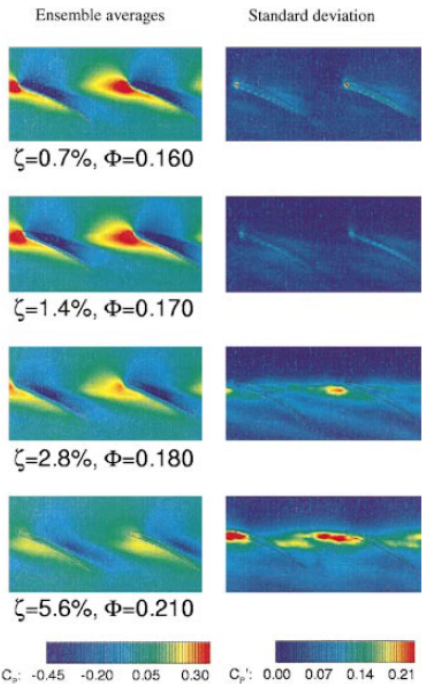


Figure 1.11.: casing static pressure ensemble average and standard deviation plots for varying tip clearance (ξ) and last stable operating point (Φ) [8].

stall. Hoying et al. [44] confirm this variation and show how "stall inception is a result of the motion of the tip clearance vortex moving out (upstream) of the blade passage".

This hypothesis though has been discarded by Pullan et al. [21] and Weichert and Day [20]. Further explanations are provided in section 1.3.3.2, spikes.

Hub corner separation

Vavra, in his review on the compressor losses [6], defines the corner separation as one of the major sources. Its formation is due to different mechanisms: secondary flows, the adverse pressure gradient and the mixing of the endwall and suction side boundary layers. Dong [45] studied the formation of the hub corner vortex separation and showed that it results from the combination of these three mechanisms. This separation is highly three

dimensional and unsteady (see Figure 1.12), and it limits the blade diffusion by increasing the blockage in the blade passage.

Schultz et al. [10] and Gbadebo [9] investigated its effect while varying the angle of attack: at higher values its extension increases in spanwise, pitchwise and chordwise directions (see Figure 1.13), producing a significant drop in the blade performance. At a certain point then, when the aerodynamic load of a blade exceeds a certain critical value, it grows suddenly and gives rise to corner stall. Several authors studied the stall inception via hub corner separation: Gbadebo et al. [9], Miller et al. [46], McDougall et al. [41]. Corner stall though will be the discussed in the following section 1.3.3.2, modal waves.

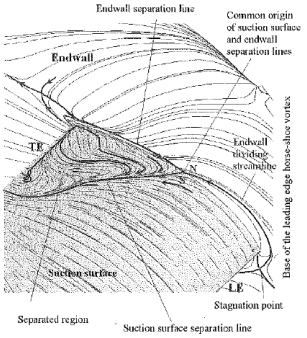


Figure 1.12.: Endwall and suction surface streamlines showing 3D separated flow [9].

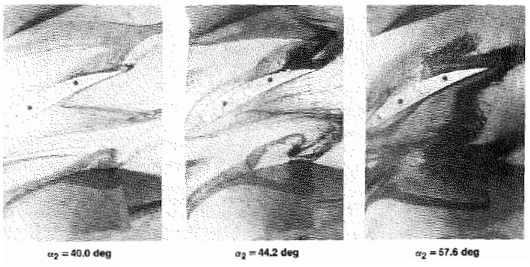


Figure 1.13.: Hub and vane suction side flow visualization at various blade loadings [10].

Given the negative impact on the compressor performance, several research studies have been undertaken in order to limit the effect of the corner separation. The first possibility is to apply take-off bleeds: this technique consists of removing the separated region from the blade suction surface, covering the whole operating range. Several cases have been presented: Gbadebo et al. [47], Naert [48], Godard [49] and they all remark an enhancement of the compressor performance. Another possibility is the hub contouring. A loading redistribution across the blade passage yields a lower velocity peak on the suction side and therefore a higher stability. Hiernaux et al. [37] applied this improvement in the Dream compressor, presented in Section 1.2, showing an increased performance in terms of pressure ratio, but also a narrower stable range.

A compressor blade design can be defined as good or bad according to the lower or higher blockage it produces. However, as pointed out by Miller et al. [46], modern design techniques are based on bidimensional methods, which are unable to take into account the strongly three-dimensional character of separations of this kind. Blockage prediction represents the ultimate

goal of the analysis in both stable and unstable operating points. This objective can be achieved by LES simulations, which require a better calibration though. To this aim, Ma et al. [50] and Zambonini and Ottavy [51] provided detailed studies on hub corner separation. They point out not only their highly three-dimensional feature, but also their unsteady and intermittent behavior. The other possibility to improve the compressor blade design, proposed by Miller et al. [46], is to increase the interaction between the designers and the test facilities by testing 3D manufactured blades, which can be produced in 1-2 days.

1.3.3. Aerodynamic instabilities

Aerodynamic instabilities affect the whole operating range of a compressor.

Mild instabilities appear in the stable range or at the stability limit, without having an excessive influence on the mechanical performance. However it is important to take them into account in the aerodynamic design, as they represent a source of loss.

The unstable range is dominated by instabilities, the two main types are rotating stall and surge.

Compressor designers aim at determining whether rotating stall or surge will occur because the consequences can be very different. From the mechanical point of view rotating stall creates additional vibrations on the blades, while surge provokes unconventional stresses.

From the aerodynamic point of view the presence of rotating stall or surge limits the compressor performance and appears as a drop in pressure ratio, and in the case of surge, as mass flow fluctuations. These phenomena have to be taken into account in the design in order to extend the stable operating range as much as possible, but also to have a complete view on the performance of the machine.

In the following paragraphs present an overview on the instabilities appearing in a compressor, both in the stable and in the unstable range.

1.3.3.1. Mild instabilities

Rotating instabilities

Rotating instabilities represent a kind of disturbance observed in stable regime, confined in the tip region. They have first been observed by Mathioudakis and Breugelmans [52], who reported "the simultaneous existence of disturbances of different wavelengths".

A more detailed description is provided by Mailach et al. [11]. The article describes the rotating instabilities as: "strong fluctuations of blade tip vortices, caused by periodical interactions of the tip clearance flow of one blade and the flow of the adjacent blade. The fluctuating blade tip vortices propagate in circumferential direction along the rotor blade row and yield

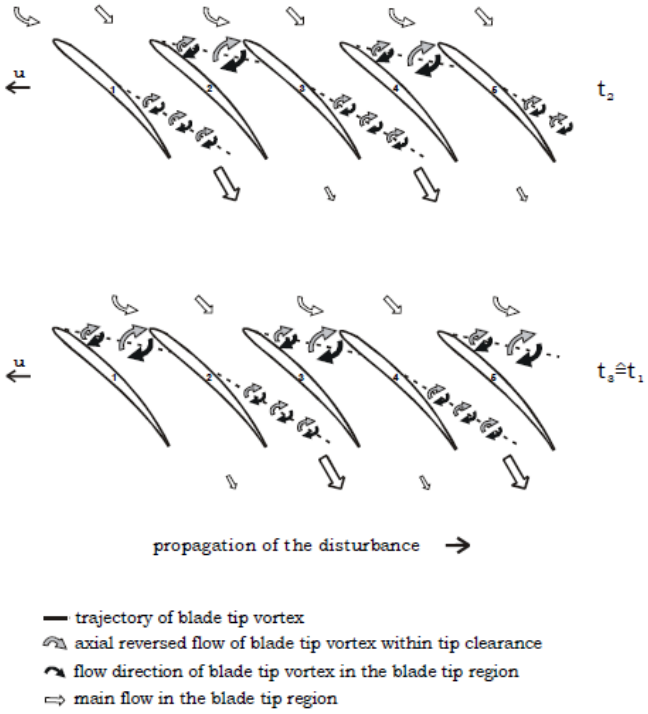


Figure 1.14.: Propagation mechanism of the rotating instabilities [11].

a rotating structure with high mode orders, which is the investigated rotating instability". Figure 1.14 presents a schematic representation of the propagating mechanism described by Mailach.

Kamaier and Neise [53], [54] also investigate on rotating instabilities in the framework of the study of the tip clearance noise and losses reduction.

All the articles dealing with rotating instabilities point out that their presence is associated to reverse flow regions in the tip area: Mailach et al. [11], Kamaier and Neise [53], [54], Pardowitz et al. [12], [13], Vo [55].

Rotating instabilities produce in the spectrum a widely spread hump at approximately half of the blade passing frequency, as shown in Figure 1.15, central. The hump is due to the fluctuation of the vortex, and, as presented by Pardowitz et al. [12], Kamaier and Neise [54], and Wang et al. [56], it consists of several discrete peaks, each one linked to a temporal Fourier component. They result in fact from a rotating source with a non-uniform circumferential distribution. The hump is evident in the signals recorded upstream the blade row.

The peculiarity of rotating instabilities is to create a rotating disturbance around the annulus, thus their complete characterization is comprehensive

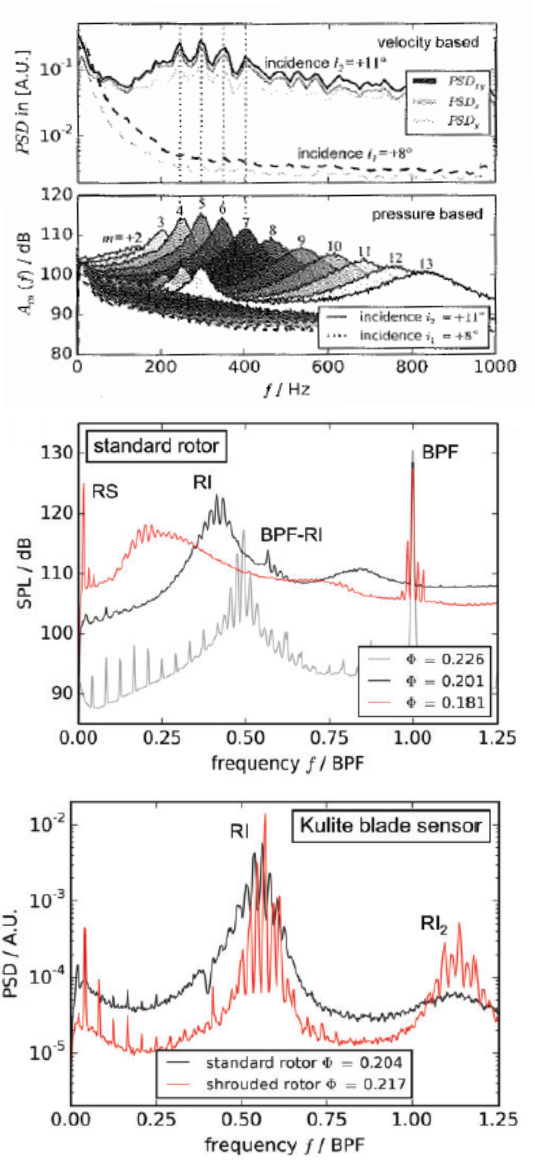


Figure 1.15.: Top: Spectrum of pressure measurements retrieved in presence of rotating instabilities, the modes are highlighted [12]. Central: typical spectrum retrieved with rotating instabilities [13] at different operating conditions (ϕ denotes the mass flow coefficient). Bottom: comparison between a spectrum retrieved in a shrouded rotor and a rotor with a tip gap [13].

of their angular speed. The latter is quantified by several authors (Pardowitz et al. [12], Kamaier and Neise [53], [54] and Wang et al. [56]) by arranging various sensors around the annulus at a corresponding axial location, providing a sufficient spatial resolution to resolve the circumferential evolution in the absolute frame. The description is completed by the presence of sensors located on the rotor blades, which allow the determination of their evolution in the relative frame.

At first the presence of rotating instabilities was associated to a large tip gap, but then it has been demonstrated that the link is not existing. Marz [8] shows their development for different clearances ranging from 0.7% to 5.6% gap/chord ratio. Pardowitz et al. [13] then tested a shrouded rotor with a wide gap between the shrouding and the casing and retrieved their presence even in that case. Figure 1.15 (bottom) presents the spectrum retrieved in the two cases. The unsteady vortex system was considered the basic mechanism generating the rotating instability, though Pardowitz demonstrated the opposite. Further research is therefore required.

Mild stall

Mild stall is a kind of instability consisting of a number of small stall cells which appear in an operating point prior to stall. It has been presented by Inoue [14], [15] in a compressor stage characterized by a hub/tip ratio equal to 0.7.

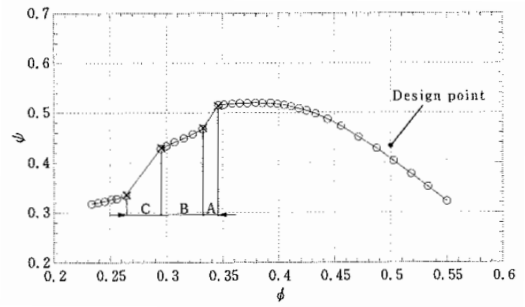


Figure 1.16.: Compressor performance map of the machine showing mild stall [14].

Mild stall has some features similar to spike stall inception as it appears as a three-dimensional separation in the tip region, though these separations are not confined within a blade passage and do not grow nor disappear within few revolutions as spikes. It is therefore closer to a part-span stall cell, rotating at approximately 70% of the shaft speed. Only a further throttling drives the machine into a stall characterized by large size cell.

Figures 1.16 and 1.17 show the performance map of the compressor studied and the corresponding time-resolved signals retrieved at a fixed throt-

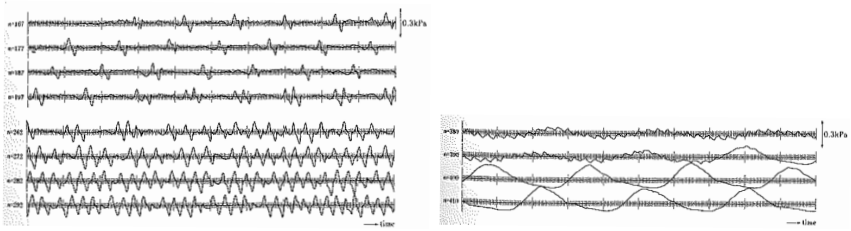


Figure 1.17.: Time-resolved pressure signals near rotor leading edge in mild stall condition (corresponding to flow range A in Figure 1.16) and rotating stall one (corresponding to flow range C in Figure 1.16) [14].

tling condition. In the operating point denoted as A the mild stall develops and appears as the fluctuations presented in Figure 1.17, left. For a further throttling (operating condition C) yields to the formation of a large cell, with the fluctuations shown in Figure 1.17, right.

The description of the detailed mechanism is also presented by Inoue [14]. The low pressure region forming ahead of the rotor is due to a separation vortex. "According to the vortex theory, bound vortices are distributed on an unstalled blade surface, which make a blade circulation (lift force). When leading edge separation occurs, a separation vortex is released on the blade surface to reduce the blade circulation". This vortex results to be therefore attached to the blade suction side and the casing, similarly to a tornado, as shown in Figure 1.18.

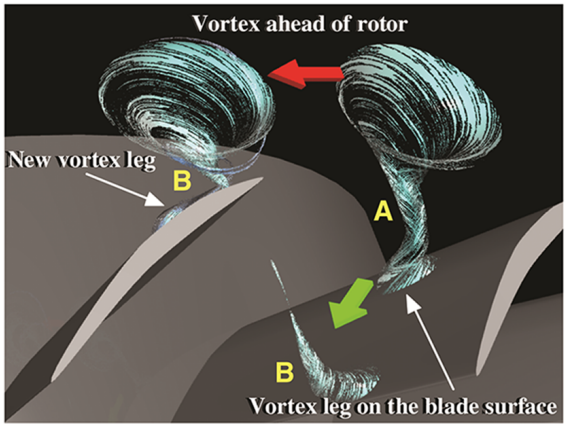


Figure 1.18.: Flow mechanism of mild stall [15].

The vortex travels in the circumferential direction for the interaction with the blades: an increased angle of attack creates the vortex, then as it moves towards the next blade it is released and mixes with the separation bubble

of the next blade, the following vortex leg is then created. The separation vortex behaves violently, therefore a wide low-pressure region appears ahead of the rotor.

Inoue [15] shows that for a higher rotor/stator gap only a large size stall cell appears, without the previous formation of mild stall.

1.3.3.2. Stall

Rotating stall in an axial compressor has first been observed by Emmons et al. [57], who provide its explanation.

Given a compressor cascade, if for any reason a blade passage separates until reaching the pressure side, i.e. stalls, the incoming flow field has to adapt. In the preceding blade passage the mass flow will increase to respect the pressure conditions at the outlet, in the following one the incidence will increase to overcome the separated region. The angle of attack on the preceding blade will therefore decrease, and the blade passage will become more stable, whereas on the following one the angle of attack will increase, and the blade passage will stall. Thus if a blade stalls, then also the following one will stall.

This is the propagation mechanism of rotating stall (shown in Figure 1.19). If the propagation conditions are favourable, it may concern several blade passages.

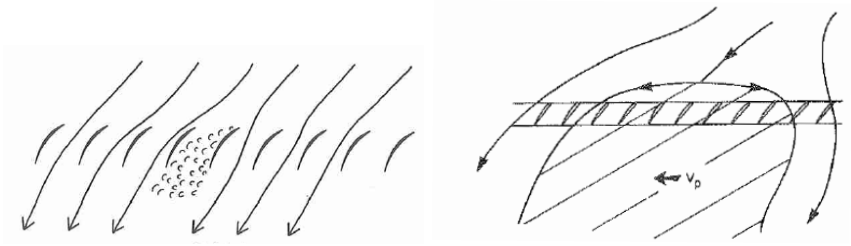


Figure 1.19.: Stall propagation mechanism [16], [17].

As stated in section 1.1, rotating stall appears in a compressor in the low mass-flow range, once reached the "surge-line". On the performance map, which is typically represented with a static-to-total pressure ratio, the surge line often locates at its peak. Further explanations are provided in the next paragraph. The presence of rotating stall produces a stable operating point affected by a strong reduction in pressure ratio (and efficiency). The machine then operates on the "stalled" characteristic, as shown in Figure 1.20.

The understanding of the behavior of a compressor working during rotating stall represents a subject of interest as in some cases multi-stage machines operate in this condition. It may also be the cause of deleterious consequences such as unexpected fatigue cracks, casing deformation and, in case it develops into surge, rotating stall may produce the failure of the

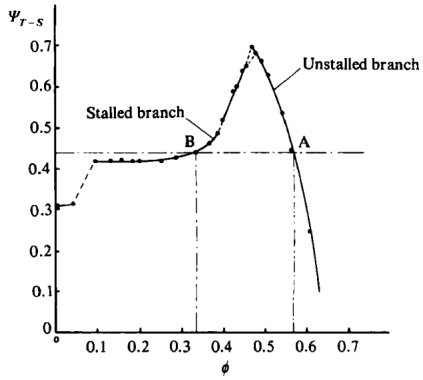


Figure 1.20.: Stalled and unstalled characteristic [18].

entire engine. The additional mechanical stresses produced have therefore to be taken into account in the structural design. Poursaeidi et al. [58] and by Mailach and Voegeler [59] show two examples of assessment of the effects of rotating stall on compressor blades.

The unstable operation of a compressor has therefore to be known for both aerodynamical and structural design.

The main difficulty for the prediction of the post-stall behavior is due to the fact that in the unstable range all the compressors operate in a different manner. Some examples in literature show indeed that stall events are not stochastic. Van de Wyer [39] presents a case where the number of stall cells vary during the same transient, and the machine has a different behavior in various experiments. Jackson [60] show how a stall cell evolves from part-span to full-span during the transient. It exist though other cases in which the stall inception always occurs at the same machine location, as the one presented by Courtiade and Ottavy [61], [62].

The post-stall behavior still cannot be predicted by numerical simulations: Gourdain [63] describes a case in which the stall cell size is not correctly retrieved by the CFD. On the other hand Crevel [64], [65] highlighted the advantages of a CFD computation for rotating stall prediction by employing as a domain the whole experimental facility, in order also to compare the numerical solution with the experimental data. In this case though the computational cost is immense (one million computational hours).

The other problem concerns the definition of the stability limit, which, as already explained in the Introduction, designers want to extend. Also in this case the CFD predictions are not accurate: some examples are reported in the works of Castillon [66], Van de Wyer [39], Sans et al. [67] .

Experimental testing represents therefore the solution for the characterization of the unstable operating points of a compressor, for which Day [2] points out two separate strands: high-speed and low-speed testing. Low-

speed testing has the advantage of gathering detailed informations with unrestricted testing time and lower instrumentation cost. High-speed testing on the other hand requires a more expensive instrumentation and the testing times are relatively short. However it has been demonstrated by Day [68] that remarkable similarities exist between the two options. For aero-engine compressors high-speed testing is in any case preferable, as a wider range of speeds can be investigated.

The following sections contain a description of the stall inception patterns and a characterization of the stall cell.

Stall inception

The most common stall inception behaviors relate to the two "classical" models presented by Day [19]: spikes and modal waves.

Day defines a simple model to predict the appearance of spikes or modal waves: modal waves appear prior to stall if the slope of the characteristic is null or slightly positive, spikes precede stall for a negative slope. "If the peak of the characteristic is reached before the critical value of rotor incidence is exceeded, then modal oscillations will occur. If, on the other hand, the critical rotor incidence is exceeded before the peak of the overall characteristic is reached, then spikes will appear in the overloaded rotor before modal activity has had an opportunity to develop". Figure 1.21 presents this concept on the performance map.

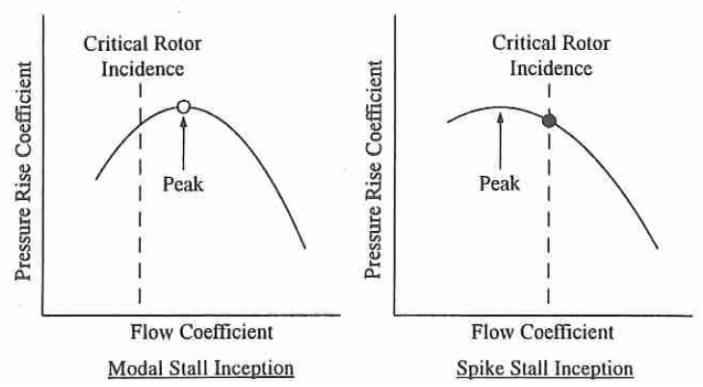


Figure 1.21.: Spikes and modal stall inception on the characteristic [19].

Stall inception - Spikes

The spikes consist of a three dimensional separation localized in the rotor tip region, which, within few rotor revolutions, grow and yield to the development of a stall cell. Since they are confined within one or few blade passages, spikes appear in a signal as shown in Figure 1.22. Jackson [60]

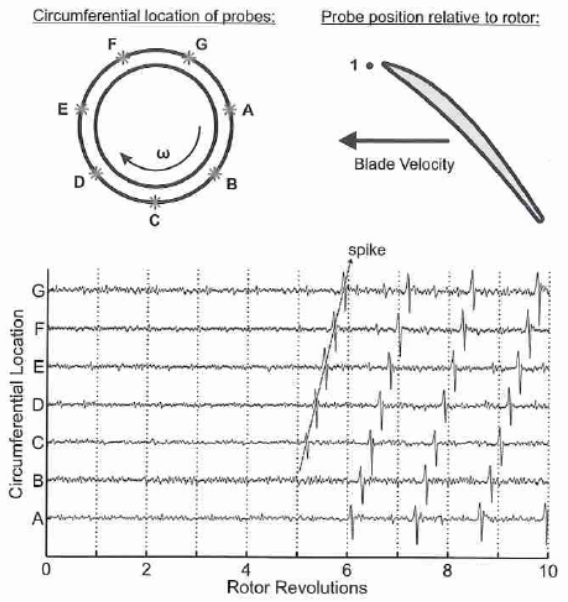


Figure 1.22.: Spike stall inception traces retrieved with sensors located near the leading edge of the blades in seven circumferential positions [20].

describes the evolution from a spike, always occurring at the same machine location, to the formation of multiple stall cells.

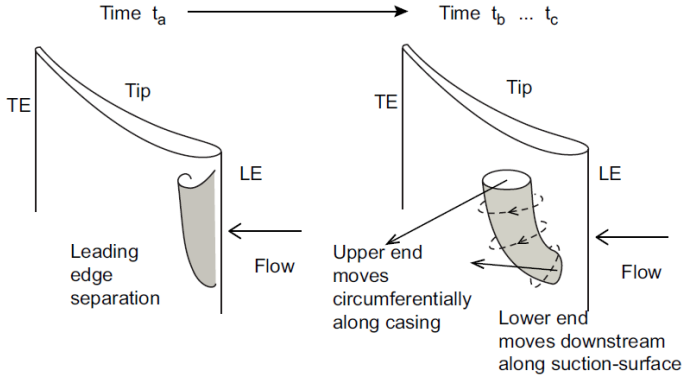


Figure 1.23.: The vortical structure and the formation of spikes [21].

As pointed out by Storer and Cumpsty [42] the tip leakage flow is strongly related to the aerodynamic loading of the blade. The first explanation found to understand the formation of spikes concerns the tip leakage vortex. It is indeed hypothesized that for a higher angle of attack the vortex moves out

of the blade passage, being aligned with the leading edge and impinging on the adjacent blade [44].

Pullan et al. [21] and Weichert and Day [20] provide an accurate description of spikes formation and suggest that it is not linked to the tip leakage vortex. Pullan et al. [21] explain in fact how the leading edge separation forms a vortex anchored on the suction side of the blade and on the casing. The vortex is convected away from the first blade towards the adjacent one, and the separation on the adjacent blade promotes the propagation of the spike in the circumferential direction. This results in a pressure fluctuation. This mechanism is very similar to the one presented by Inoue [15] and its structure is sketched in Figure 1.23.

Yamada [69] confirms the presence of a tornado like vortex during the formation of spikes with a DNS simulation.

Spikes have been detected in compressors characterized by different gaps and also shrouded rotors [21].

Stall inception - Modal waves

The modal waves represent a stall precursor, and are caused by hub corner stall. The modal waves create an instability on the entire annulus and appear in a two-dimensional flow field: no variation along the radius is remarked by McDougall et al. [41]. Modal waves affect the formation of the cell in the region where the velocity is the lowest, as shown in the Figure 1.24. Their amplitude is due to the thickening and thinning of the hub corner separation, which extends across the blade passage with respect to its "stable" condition. The diffusion in the hub region can be employed as a criterion to define at which operating condition the compressor will stall as presented by Lei et al. [70].

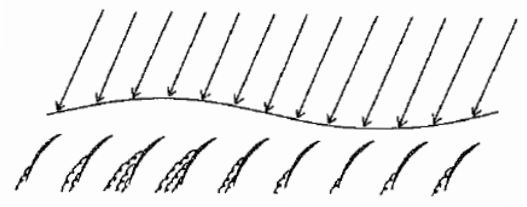


Figure 1.24.: Effect of velocity perturbation on the wake size [16].

McDougall et al. [41] point out that the endwall blockage represents a fundamental feature which determines the stall point: if the blockage extends in the hub region modal waves will appear, if in the tip region spikes. The stalling process is indeed influenced not only by the characteristic but also by the tip gap: a large clearance provokes a tip separation, while a small one yields to hub separation at first.

At the beginning of this section it is stated that modal waves appear at the peak of the compressor characteristic. In fact Day [16] highlights that

a compressor represents a damped oscillatory system: when modal waves appear it becomes less and less damped and it is pushed further towards lower flow rates. As modeled by Stenning [17], the compressing system results to be dynamically unstable at the peak of the curve.

In the compressor stability analysis, as in the model proposed by Moore and Greitzer [71], [72], the characteristic is typically described in terms of load coefficient $(p_{Sout} - p_{Tin})/c_x$, in which p_{Sout} is the compressor outlet static pressure, p_{Tin} is the compressor inlet total pressure and c_x is the axial velocity through the machine. The peak of the curve is reached at $d(p_{Sout} - p_{Tin})/dc_x = 0$, which corresponds to a dynamically unstable compressing system, hence the condition in which rotating stall appears is $d(p_{Sout} - p_{Tin})/dc_x \geq 0$.

The perturbations upstream of the rotor (modal waves), appearing at the peak of the characteristic, can be interpreted as the response of the system to a disturbance in the blades, as discussed in the contribution of McDougall et al. [41]. In the same article it is explained the amplitude increase, referring to Cumpsty [73]: not the entire annulus has to satisfy the condition $d(p_{Sout} - p_{Tin})/dc_x \geq 0$ to enter rotating stall, but if a great section undergoes this condition the compressor stalls and the waves increase their amplitude. The Moore-Greitzer model states that both rotating stall and surge originate from a disturbance which grows in amplitude, according to the initial conditions, i.e. the damping of the system and the compressor characteristic.

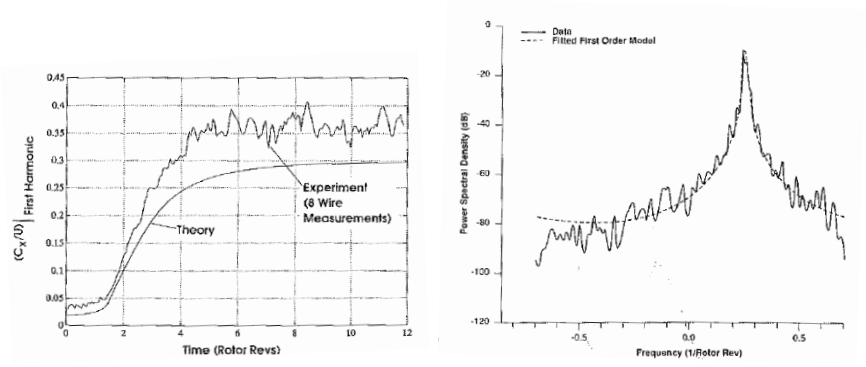


Figure 1.25.: Comparison between the predicted and the measured first harmonic of the axial velocity in the time evolution (left) and the spectrum (right) [22].

Epstein et al. [22] investigated their growth rate by comparing experimental data, retrieved with an ad hoc set-up, and the prediction of the Moore-Greitzer theoretical model applied to the modal waves. Once given the compressor steady state characteristic and geometry, the theoretical model shows good agreement with the experimental data: both the spectrum and

the disturbance growth rate predictions are matching (see Figures 1.25 left and right). The first and the second modes are shown: McDougall et al. [41] indeed noticed that they are predominant whereas the other modes show an exponential decay. Hynes et al. [74] provide an example in which they manage to increase the operating range by 8% by applying active control to the first and the second harmonic. The axial velocity measured by a set of hot-wire anemometers covering the whole circumference at the rotor inlet is employed to vary the stagger angle of the inlet control vanes, thus the axial velocity spatial distribution related to the first and the second harmonic.

Day [16] discovered that the operating range in which modal waves are detected is very limited. Modal waves increase their amplitude as the mass flow is reduced, following an almost linear trend.

This contribution also demonstrates that modal waves not necessarily yield rotating stall. This is the reason why they are called "modal waves" and not "prestall disturbances" as in the article of Epstein et al. [22]. The difference between a stall cell and a modal wave is that the former provokes a drop in the compressor characteristic, while if modal waves appear the compressor can be brought back to stable conditions by opening the throttling valve. However typically the rotational speed and size of the modal waves are similar to those of the stall cell, as in the case presented by McDougall et al. [41].

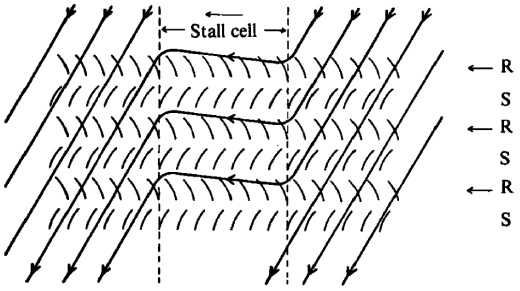


Figure 1.26.: Sketch of the flow lines retrieved across a stall cell in the absolute frame [18].

Stall cell characterization

A general distinction is made between part-span and full-span rotating stall cells [2]. Part-span stall cells typically appear in stages having a low hub/tip ratio, and in a number always greater than one. They are characterized by a rotational speed which varies between 50 and 80% of the shaft speed and are confined in the tip region. Full-span stall cells on the other hand usually appear in stages with a high hub/tip ratio and are rarely more than one. Given their inertia they have a rotational speed comprised between 30 to 50% of the shaft speed.

Once defined which kind of cell will appear it is also possible to determine the global performance of the compressor. Day et al. [75] developed a model to describe the stalled characteristic: the compressor is working as two parallel machines, one operating at zero flow rate and the other one at a mass flow higher than the design one. The drop of the characteristic varies according to the blockage produced by the cell, and therefore changes if it appears a full-span or a part-span stall cell.

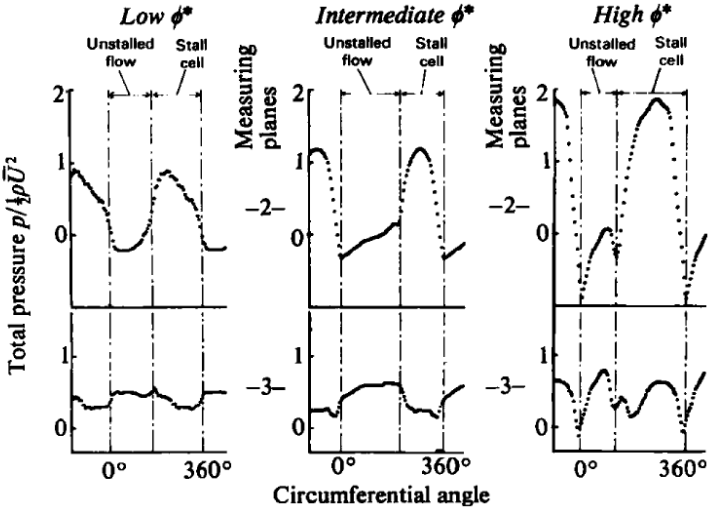


Figure 1.27.: Typical total pressure measurements retrieved in a stall cell at different rotational speeds (identified with different mass flow coefficients ϕ^*) [18]. In this case the data presented are acquired up- and down-stream the first rotor of a three stage configuration (respectively measuring planes 2 and 3).

Day and Cumpsty [18] provide a thorough and general description of the flow field inside a stall cell, and remark no differences between a part-span and a full-span stall cell.

The flow field inside a stall cell is extremely complex. At first it was hypothesized a similarity with a dead wake region. However it was soon discarded by Day and Cumpsty [18], by presenting observations inside a stall cell.

The stalled flow field is characterized by high tangential velocities, which appear of the order of magnitude of the rotor velocity. Tangential continuity has to be respected, thus the velocity is much higher in the stall cell than in the undisturbed flow. Figure 1.26 presents a sketch of the absolute velocity which is typically retrieved around the annulus in a stalled multi-stage compressor.

Tangential velocities are high ahead of the rotor and low at its outlet.

Saxer-Felici et al. [76] retrieve the same pattern with a CFD simulation and present it in the cell relative frame.

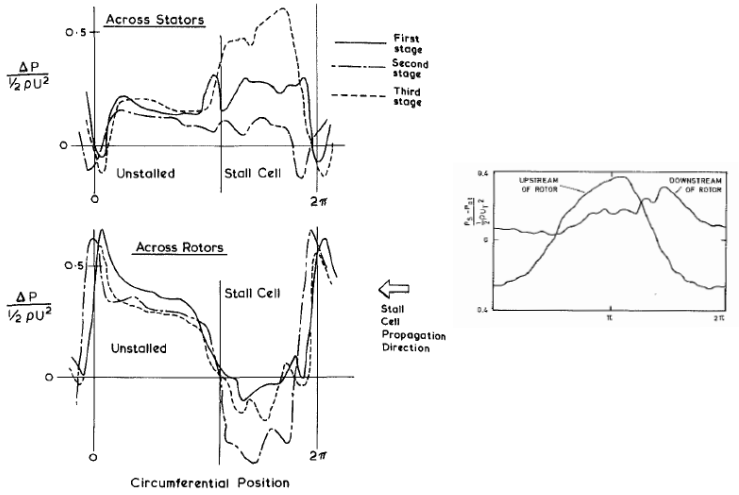


Figure 1.28.: Left: Pressure differences across the blade rows [23], Right: Outer wall static pressure inside a stall cell [24].

Another feature retrieved is a loss of inertial energy in the axial direction, which translates into either reversed flow in some regions or as recirculation within the blade rows themselves. Centrifugal effects in the rotor blade row create static pressure gradients along the span.

Several authors investigated the measurements within a stall cell: Das and Jiang [77], [78], I. Day [79], Breugelmans et al. [24], [80], Saxer et al. [76], [81]. All the features retrieved by Cumpsty and Day [18] are confirmed by the other articles. Not only velocity measurements are presented by also pressure and angle ones. An example of total pressure measurement at the rotor inlet and outlet is shown in Figure 1.27.

The greatest variations appear at the boundaries of the stall cell. It is therefore possible to determine its leading and trailing edge. Cumpsty and Greitzer [23] employ the pressure differences across the rotor and the stator blade rows for its definition:

1. the trailing edge resides at the local positive peak on the ΔP_{Rotor}, at the local negative peak on the ΔP_{Stator}
2. the leading edge resides at the local negative peak on the ΔP_{Rotor}, at the local positive peak on the on the ΔP_{Stator}

An application of their criterion is presented in Figure 1.28.

Breugelmans et al. [24] provide an accurate description of the flow field inside the stall cell and define the trailing edge location at the static pressure

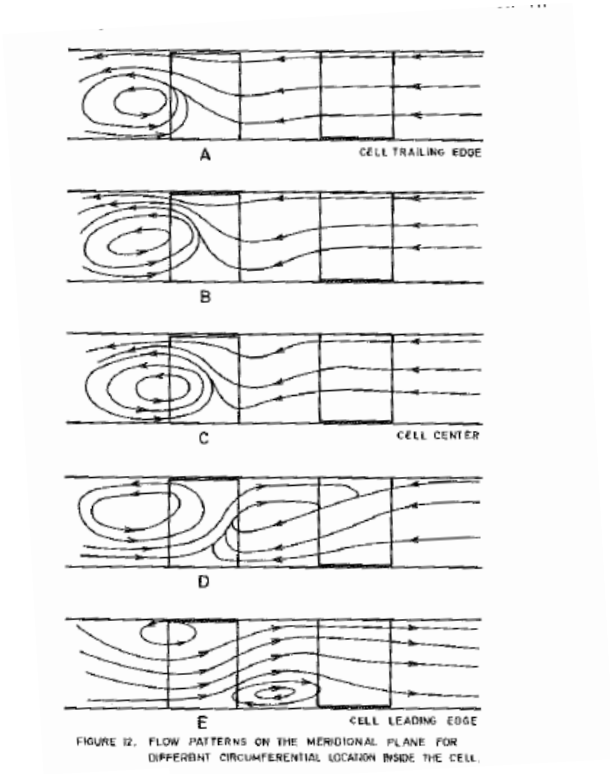


Figure 1.29.: Flow patterns on the meridional plane for different circumferential locations inside a stall cell [24].

peak at the casing rotor outlet (as shown in Figure 1.28). In their article indeed the flow patterns at different circumferential locations inside the cell are presented. The trailing edge is characterized by a reversed flow: the delta pressure across the stage is so high that the flow field cannot overcome it. The hub region at the rotor inlet presents a recirculation which increases its size across the cell, until reaching the full span at the cell center. The recirculation then shifts towards the tip region at the stall cell leading edge. At this location the flow is not reversed. These outcomes are found to be a common pattern in the stall cells and are reported in Figure 1.29.

The complexity of the flow field inside a stall cell is not only due to the variations across the cell itself but also to the evolution it may take during the transient, as in the example presented by Jackson [60].

1.3.3.3. Surge

It is universally recognized that rotating stall is a precursor of surge, as retrieved by Day [68], [82]. Surge is an instability of the entire compression system, typically appearing as high amplitude mass flow fluctuations which produce an axial pulsation across the compressor. It typically occurs at high rotational speed.

Surge is characterized by mass flow fluctuations across the compressor, therefore on the performance map it appears as a hysteresis cycle. Figure 1.30 presents an example of surge cycle. On the other hand a time-resolved signal will alternatively show the fluctuations due to rotating stall, when the machine operates in the unstable range, and a zone without fluctuations, when it operates in the stable range, resulting in a signal similar to the one presented in Figure 1.30.

Most of the compression systems consists of a compressor operating in a duct, which is discharging in a plenum of much higher volume, being the latter connected to the atmosphere by a throttling valve. The typical configuration is sketched in Figure 1.31.

Stenning [17] defined the elements necessary for the study of surge: a compressor, a mass storage (consisting of the plenum), fluid inertia, a throttle. Emmons et al. [57] compared the compression system to a Helmholtz resonator in their experiments. A resonator in fact consists of a large jar with a small neck, where the greatest part of kinetic energy resides in the neck. The frequency of oscillation (ω) depends on the enclosed volume (V_p) and on the length (L_c) and the area (A_c) of the neck. It can be expressed in the following way:

$$\omega = a \times \sqrt{\frac{A_c}{V_p \times L_c}} \tag{1.5}$$

This comparison is also employed by Greitzer [83], [25] and by Moore and Greitzer [71], [72] in their prediction models.

1.4. Objective

The current environmental constraints require the production of the new machines with unconventional designs. The traditional conception techniques indeed comprise design correlations and analysis tools (such as CFD simulations), which may yield to compressor stages satisfying the desired requirement of higher loading, having though the drawback of a reduced stall margin.

The Dream optimized design is an example of such a development philosophy and motivates the extended study of the baseline blade in this PhD project, together with the lack of specific knowledge on boosters highlighted in the Literature survey.

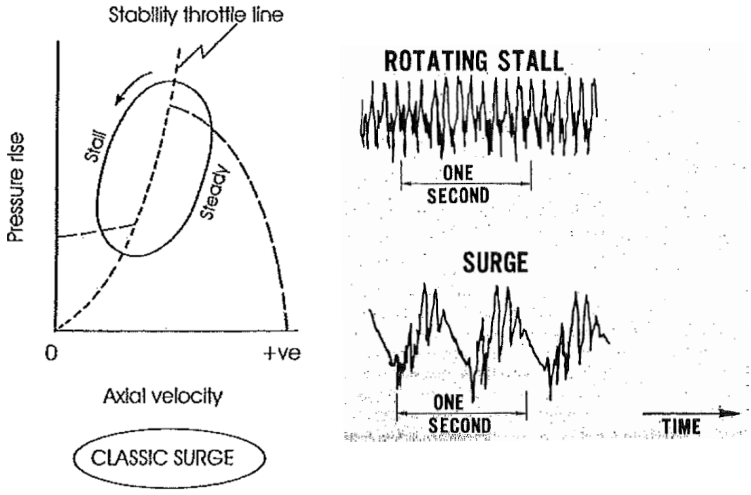


Figure 1.30.: Left: typical performance map during surge [2], Right: typical time resolved signal retrieved during surge and comparison with rotating stall [25].

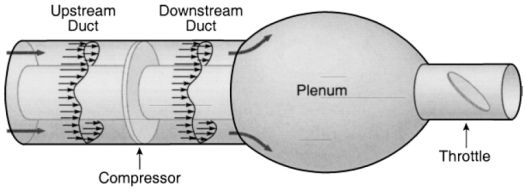


Figure 1.31.: Sketch of a typical compression system [26].

The experimental characterization represents the only way to improve the actual conception techniques, enabling to find new designs which satisfy the environmental constraints.

At present indeed there is a lack of informations regarding the design guidelines of new machines, and, as discussed in the Literature survey, CFD is not an appropriate tool to fulfill them: either the accuracy is not appropriate, or the computational cost is very high. Moreover the new designs can not be based on the data of the existing machines.

The objective of this work is the experimental characterization of a state-of-the-art booster in its unstable operating range, in order to gain a deep understanding on these phenomena and to contribute to the improvement of the design of new engines. Detailed measurements are indeed available on the Dream baseline blade in its stable and unstable range.

The measurements in a state-of-the-art compressor stage allow the knowledge of the flow structures appearing in its whole operating range. The char-

acterization is necessary not only for the analysis of the flow field, but also to improve the numerical tools. The analysis of a state-of-the-art booster represent the basis for the design of machines of new generation and aims at contributing to both the experimental and the numerical techniques employed for the description of the unstable range of a compressor.

1.5. Methodology and Thesis organization

The Literature survey shows how compressors are affected by unsteady phenomena in both the stable and the unstable range, resulting in a highly three-dimensional and complex flow field. The flow structures appearing still present some open questions (e.g. the origin of the mild instabilities) which require further investigation. The precursors to the stall inception reside in the unsteady separations appearing in the stable range, which are also influencing the shape of the stall cell(s).

This study therefore aims the characterization of the unstable range of a state-of-the-art booster by the determination of the unsteady flow structures in the stable one, and the understanding of their evolution at both the stability limit and in the post-stall behavior.

The facility and the experimental set-up are described in Chapter 2, including the instrumentation employed in the time-averaged and the time-resolved measurements. This experimental characterization, in order to be utilized as a reference case for new design tools, presents also a thorough uncertainty analysis applied to the measurements.

The global performance of the machine is then defined with time-averaged measurements. Numerical simulations are employed for the performance of each blade row. The detailed description of the flow field in stable regime is then provided with the time-resolved measurements on the rotor casing and downstream the rotor and the stator. The time-resolved measurements enable to identify the various flow structures. All these topics represent the object of Chapter 3.

Finally Chapter 4 presents the characterization of the unstable regime. At first is defined the stall margin from the global performance point of view and on the manner of entering the unstable range. The phenomena appearing at the stability limit are described by employing the time-resolved pressure measurements introduced in Chapter 2. The post-stall behavior is presented with the analysis of the stall cell and its accurate three-dimensional description. Also in this case the time-resolved measurements are utilized.

Chapter 5 presents the conclusions of the project.

Chapter 2.

Experimental set-up

2.1. VKI-R4 facility

2.1.1. The facility

The VKI-R4 is a high speed compressor facility, which can be employed for both radial and axial compressor stages. The test-rig is a closed loop. It can be pressurized between 0.3 and 3 bar. The test section utilized in the present measurement campaign has been designed at VKI. A throttling valve allows the regulation of the mass flow. A water heat exchanger controls the inlet total temperature, while a control system connected to a pressure source and to a vacuum pump regulates the inlet total pressure (the test conditions are provided in Table 2.1). The shaft is driven by a 450 kW DC motor, connected to the rotor by means of a gearbox. The maximum rotational speed of the latter is 9000 rpm. A sketch of the facility is presented in Figure 2.1.

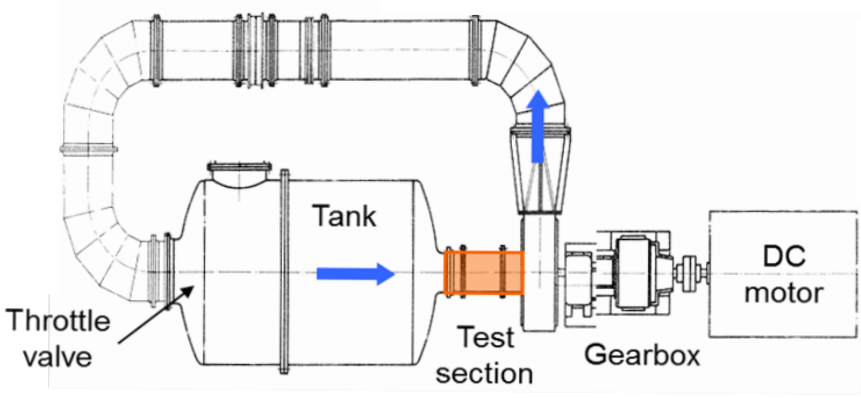


Figure 2.1.: Sketch of the VKI-R4 facility.

2.1.2. Dream test section

In an engine, the fan provides the core with a pressure ratio distribution skewed towards the hub. The booster is located after the fan, it has the

N IGV blades	100
N rotor blades	76
N stator blades	100
Rotor outlet diameter	240
Blade height (R, S)	43, 38 mm
Rotor tip gap	0.3 mm (0.8% span)
Chord at hub (R, S)	27, 24 mm
Rotor stagger at midspan	40 deg
Hub/Tip (R, S)	0.82, 0.85
Aspect ratio (R, S)	1.59, 1.58
Solidity (R, S)	1.45, 1.86
Inlet total pressure P0 (P_{ref})	116868 Pa
Inlet total temperature T0 (T_{ref})	293.05 K
Nominal rotational speed	8748 rpm

Table 2.1.: Quantities characterizing the stage.

function to counterbalance this effect, but not to provide a high pressure ratio. The new design technologies tend to increase the aerodynamic load, imposing high diffusion factors in the low radius region thus making hub critical stages.

The present booster is the first stage of the core and has been scaled to be adapted to the test section of the facility employed for the tests. A fixed stagger inlet guide vane row (IGV) is placed to simulate the spanwise flow distribution provided by the fan root. The rotor blades are characterized by a 0.82 hub/tip ratio and an inlet relative Mach number at the tip of approximately 0.8. The nominal rotational speed is 8748 rpm (100% Nn).

The stage is composed by an IGV blade row with 100 blades, a rotor blade row with 76 blades and a stator blade row with 100 blades. A sketch is shown in Figure 2.2, right. A summary of the quantities characterizing the stage is presented in Table 2.1.

The inlet total pressure is kept constant by a valve connecting the reservoir to the atmosphere. The inlet total temperature is maintained with a water heat exchanger located in the settling chamber. Considered the temperature raise of the flow while testing (equal to approximately 10° C in one hour testing), the absolute rotational speed is continuously adapted to the temperature variations, by keeping constant the reduced rotational speed. The mechanical speed is indeed corrected by the standard condition $T_{standard} = 288.15K$:

$$N_{corrected} = \frac{N}{\sqrt{\frac{T_{T,0}}{T_{standard}}}} \tag{2.1}$$

The inlet total pressure and temperature (P_{ref} and T_{ref} shown in Ta-

ble 2.1) are considered as reference and all the pressure and temperature distributions presented in Chapters 3 and 4 are non-dimensionalized with respect to these values.

2.1.3. The experimental set-up

The performance of the stage is monitored by total pressure and temperature rakes and static pressure taps located at the inlet and at the outlet of the test-section in Planes 0 and 4, as shown in Figure 2.2, left. All these measurements are sampled at 2 Hz. More details on these measurements are given in section 2.3.

Five axial locations, presented in Figure 2.2 (left), allow acquisitions along radial traverses: far upstream the IGV (plane 0), at the IGV inlet (plane 1), at the rotor inlet (plane 2), at the rotor outlet (plane 3) and at the stator outlet (plane 4). Probe traverses are available at four circumferential positions (0°, 90°, 180°, 270°, in which 0° is located at the top, as shown in Figure 2.3) at each measuring plane.

The IGV and the stator blade rows are able to displace along 4 stator pitches, in order to simulate the probe movement in the circumferential direction.

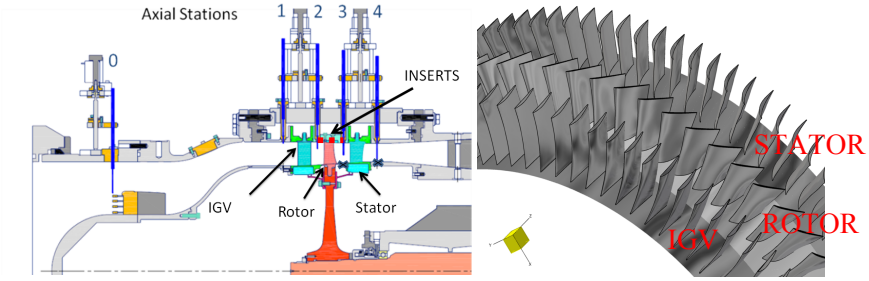


Figure 2.2.: Dream test section, the measuring planes (0, 1, 2, 3, 4) are shown in the left Figure.

Fifteen piezo-resistive pressure transducers monitor the static pressure at the rotor casing by means of time-resolved measurements. In addition two sensors are measuring the time-resolved static pressure at the rotor and stator outlet at the hub. Their description is provided in Section 2.4.2.

The signal from an optical once-per-revolution sensor mounted on the shaft is recorded to provide the compressor rotational speed. It is used as a reference in phase-locked averages.

All the acquisitions of the time resolved data are performed with a 16 bit data acquisition system with a sampling frequency of 1MHz.

This set-up has been adopted for all the operating points investigated and all these data are available for both the stable and the unstable operating

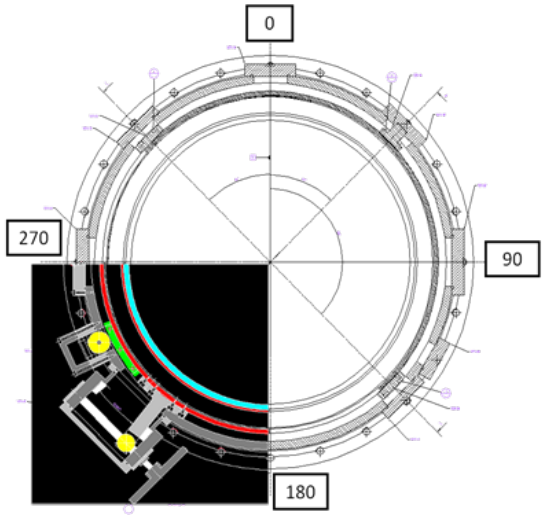


Figure 2.3.: Circumferential locations in the test section in which it is possible to perform radial traversing.

points.

2.2. Uncertainty calculation method

The uncertainty methodology adopted in this study is the ASME. A small summary is provided in this paragraph, while more details refer to Appendix A.

The ASME method categorizes error sources into systematic (bias) and random. The former remain constant during the experiment, the latter cause scatter in the result.

The systematic errors are often denoted with b_i and are combined as:

$$b = \sum_i \sqrt{(b_i)^2} \tag{2.2}$$

Random errors can be computed once ensured the data-set is fitting a Gaussian distribution, as they are estimated as the standard deviation from the average. In case a data fit $\mathbb{M}$ is employed, its quality is estimated with the "standard estimate of error":

$$SEE_{\mathbb{M}} = \sqrt{\frac{\sum_{i=1}^{N} (\mathbb{M}_i - \mathbb{M}_{fit,i})^2}{N - K}} \tag{2.3}$$

in which N stands for the number of points in the data-set and K for the number of coefficients of the polynomial employed in the fit. The SEE is

used instead of the standard deviation. $N - K$ represent the degrees of freedom of the random uncertainty source, in some other cases the degrees of freedom are denoted as ν. The random uncertainty $s_{\overline{\mathbb{M}}}$ is then computed as:

$$s_{\overline{\mathbb{M}}} = \frac{SEE_{\mathbb{M}}}{\sqrt{N}} \tag{2.4}$$

Once defined the systematic and the random uncertainties, the total uncertainty can be estimated as:

$$U_T = \sqrt{\sum_{i=1}^{M_b}(b_i^2) + \sum_{i=1}^{M_s}(s_{\overline{X}_i}^2)} \tag{2.5}$$

The expanded uncertainty U_{95} is taking into account a confidence interval, by the coefficient $t_{95}(\nu)$, which represents the appropriate value of the t-distribution for 95% confidence interval:

$$U_{95} = \pm t_{95}(\nu) \times \sqrt{\sum_{i=1}^{M_b}(b_i^2) + \sum_{i=1}^{M_s}(s_{\overline{X}_i}^2)} \tag{2.6}$$

2.3. Time-averaged measurements

As previously stated the global performance of the machine is monitored during the experiments.

Each of the four rakes located in plane 0 and in plane 4 consists of six small Kiel heads each one containing a total pressure tap and a T-type thermocouple junction. The corresponding axial position is equipped also with static pressure taps at the hub and in the casing, they are eight in plane 0 and five in plane 4.

The quantities provided in real time during the tests are: total temperature and Mach number distributions, averaged total and static pressure and total temperature in each measurement plane. The total-to-total and total-to-static pressure ratio and mass flow are shown as area averaged quantities. The efficiency is derived from the averaged quantities and displayed. The corrected and the mechanical rotational speed are also monitored, together with the throttling valve opening.

2.3.1. Pressure measurements and uncertainty

The inlet and the outlet rakes (and pressure taps) are respectively connected to a 5 and a 15 psi relative pressure scanners.

Whether it be static or total pressure, the measurement is obtained as:

$$P = P_{transducer} + P_{atmospheric} \tag{2.7}$$

The uncertainty is therefore computed with the contributions of the two sources:

$$\delta P = \sqrt{(\delta P_{transducer})^2 + (\delta P_{atmospheric})^2} \tag{2.8}$$

The manufacturer reports the uncertainty value as the 0.5% on the full range of the transducer (with a 95% confidence level). Thus it results to be:

$\delta P_{transducer,inlet} = 5psi * 0.05/100 = 0.17mbar$

$\delta P_{transducer,outlet} = 15psi * 0.05/100 = 0.52mbar$

The ambient pressure is measured by means of a Druck DPI 150 precision pressure indicator with an uncertainty $\delta P_{atmospheric} = 0.75mbar$.

The combination of the two factors yields the values reported hereunder:

$$\delta P_{inlet} = \sqrt{(\delta P_{transducer,inlet})^2 + (\delta P_{atmospheric})^2} = 0.77mbar \tag{2.9}$$

$$\delta P_{outlet} = \sqrt{(\delta P_{transducer,outlet})^2 + (\delta P_{atmospheric})^2} = 0.913mbar \tag{2.10}$$

The resulting uncertainty on the pressure ratio $\delta\pi$ is computed as:

$$\delta\pi = \sqrt{(\frac{1}{P_0}\delta P_4)^2 + (\frac{-P_4}{P_0^2}\delta P_0)^2} \tag{2.11}$$

It results to be approximately 0.2% of the total-to-total pressure ratio and 0.16% of the static-to-total pressure ratio at design operating point at 100% Nn.

Mach number measurements and uncertainty

Mach numbers in the test rig are derived from the total and static pressure measurements in planes 0 and 4:

$$Mach = \sqrt{\frac{2}{\gamma - 1}[(\frac{P_0}{P_s})^{\frac{\gamma-1}{\gamma}} - 1]} \tag{2.12}$$

The uncertainty on the Mach number is calculated from the uncertainties on the static and total pressure measurements, as follows:

$$\delta Mach = \sqrt{[\frac{\partial Mach}{\partial P_s}\delta P_s]^2 + [\frac{\partial Mach}{\partial P_0}\delta P_0]^2} \tag{2.13}$$

The static pressure uncertainty δP_s corresponds to the one presented in the previous paragraph for the inlet and the outlet rakes, in fact they are connected to the same pressure scanner.

The typical value obtained for the Mach number uncertainty is 0.015.

2.3.2. Temperature measurements and uncertainty

The thermocouples contained in the rakes are shielded T-type thermocouples, they are indeed well suited for applications within $-200°$ and $350°$. They are directly linked to a digital scanner, which has the function to: keep constant the reference junction temperature (the cold reference is indeed contained in the scanner); convert the output into a digital signal (A/D characterized by 22 bits); provide the thermocouple junction temperature, using their calibration curve and the reference temperature. The temperature is computed as:

$$T_j = T_{TCref} + \Delta T \tag{2.14}$$

The shield has the function to minimize the effect of the environment on the thermocouple. However the flow is not arrested adiabatically, as the boundary layer near the thermocouple junction dissipates the flow energy, thus it exists a velocity error and the temperature measurement has to be corrected for the influence of the flow velocity. This problem is typically handled by applying the recovery ratio to the measurements:

$$r = \frac{T_j}{T_T} \tag{2.15}$$

Its value derives from the aerodynamic calibration, and depends on the Mach number. The rakes recovery factor has been determined via aerodynamic calibration in the VKI-C4 facility. Its variation is reported in Figure 2.4, right.

The size of the heads is proportional to the span height: a higher diameter is utilized for the shields of the inlet rakes whereas a smaller one for those at the outlet. The recovery factor is therefore expected to be higher for the inlet rakes, while the graph shows an opposite trend. This result in fact contributed to trigger the modification of the calibration facility: the same graph obtained with the improved configuration shows opposite trends.

The first step for the temperature measurements uncertainty calculation is the assessment of the recovery factor calculation uncertainty.

The best curve approximation for $r = f(Mach)$ is found to be a third order polynomial curve. The scatter around the curve fit represents the main uncertainty source. It is calculated with the standard error of estimate, as explained in Appendix A:

$$SEE = \sqrt{\frac{(\sum_{i=1}^{N}(y_i - \overline{y_i})^2}{N-k}} \tag{2.16}$$

The second uncertainty source derives from the calibration itself. It can be obtained as:

$$\delta r_{meas} = \sqrt{(\frac{1}{T_T}\delta T_j)^2 + (\frac{-T_j}{T_T^2}\delta T_T)^2} \tag{2.17}$$

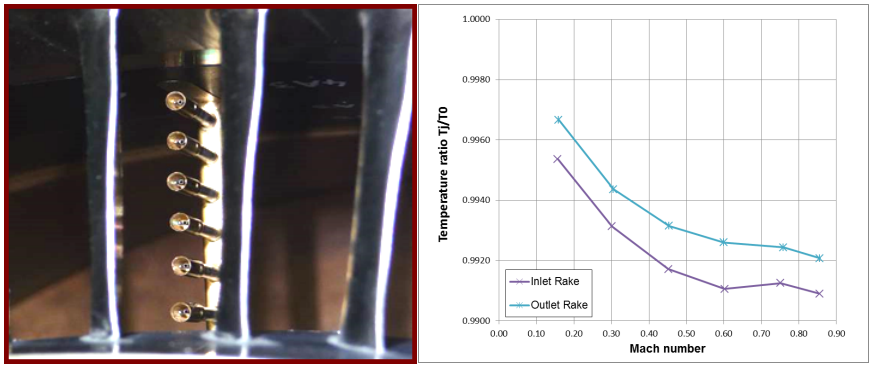


Figure 2.4.: Photo of the rakes, recovery factor of the inlet and the outlet rakes.

Finally the calibration uncertainty results to be the combination of the two uncertainty sources:

$$\delta r_{calib} = \sqrt{(\delta r_{meas})^2 + (\frac{SEE}{\sqrt{N}})^2} \tag{2.18}$$

The value obtained is Mach dependent.

For the thermocouples the uncertainty value assessed by the scanner manufacturer is $\delta T = 0.125°$ C. The measurement value is quantified by applying the recovery factor:

$$T_T = \frac{T_j}{r} \tag{2.19}$$

The uncertainty is therefore computed as the combination of the various uncertainty sources:

$$\delta T_T = \sqrt{(\frac{\partial T_T}{\partial T_j}\delta T_j)^2 + (\frac{\partial T_T}{\partial r}\delta r)^2} = \sqrt{(\frac{1}{r}\delta T_j)^2 + (\frac{-T_j}{r^2}\delta r)^2} \tag{2.20}$$

The recovery factor uncertainty depends on both the Mach number and on the calibration uncertainty:

$$\delta r = \sqrt{(\partial r)^2_{Mach} + (\partial r)^2_{calib}} = \sqrt{(\frac{\partial r}{\partial Mach}\delta Mach)^2 + (\delta r)^2_{calib}} \tag{2.21}$$

The first term can be obtained by computing the local slope of the curve reported in Figure 2.4, right. The second term represents the recovery factor calibration uncertainty. This last value is much higher than the first one, so only the calibration uncertainty is considered in the calculation. The uncertainty values are comprised between ± 0.65 and ± 0.7 K, having higher values at higher Mach numbers.

2.3.3. Efficiency measurements and uncertainty

The efficiency is computed from the total pressure and temperature measurements retrieved with the rakes as follows:

$$\eta = \frac{(\frac{P_4}{P_0})^{((\gamma-1)/\gamma)} - 1}{(\frac{T_4}{T_0}) - 1} \tag{2.22}$$

The uncertainty is retrieved with the combination of the various uncertainty sources, mentioned in the previous paragraphs:

$$\delta\eta = \sqrt{(\frac{\partial\eta}{\partial P_4}\delta P_4)^2 + (\frac{\partial\eta}{\partial P_0}\delta P_0)^2 + (\frac{\partial\eta}{\partial T_4}\delta T_4)^2 + (\frac{\partial\eta}{\partial T_0}\delta T_0)^2} \tag{2.23}$$

The value obtained represents approximately 4% of the efficiency value retrieved at design condition, nominal speed.

2.4. Time-resolved measurements

The detailed characterization of the flow field of the Dream compressor stage is performed by time-resolved measurements, therefore the facility has been instrumented with fast-response pressure sensors and a probe.

As pointed out by Sieverding et al. [84] and Ainsworth et al. [85], the miniature piezo-resistive sensors utilized for time-resolved pressure measurements, are sensitive to both pressure and temperature. They are built by forming a Wheatstone bridge using four resistors on a semiconductor membrane.

This temperature dependency can be compensated in two ways: a passive compensation, which is the conventional approach where external compensation resistors are added to reduce the sensitivity of the bridge output; or an active compensation, where the changes of the overall bridge resistance are monitored as a measure of the sensor temperature. Mersinligil et al. [86] have previously demonstrated that the active compensation is superior in terms of accuracy of the pressure readings but requires a full pressure and temperature calibration. The active compensation is implemented by including the sensor bridge into another Wheatstone bridge, as shown in Figure 2.5, right, where the output of the outer bridge is proportional to the sensor temperature.

2.4.1. Fast-response pressure probe

The probe used in the present study, shown in Figure 2.5, is a single sensor fast response aerodynamic pressure probe with a Ø3 mm head and a 25 psi (∼1700 mbar) flush-mounted absolute sensor.

The probe employs an active compensation scheme. In this configuration, $V_p(T, P)$ and $V_s(T, P)$ are the output voltages corresponding to the inner and the outer bridges (indicated as P and T outputs in Figure 2.5) respectively.

The amplifier provides a gain of 100 and is linked to the acquisition system. As the sampling frequency employed is very high (more than twice the sensor natural frequency), no filter is applied during the measurements.

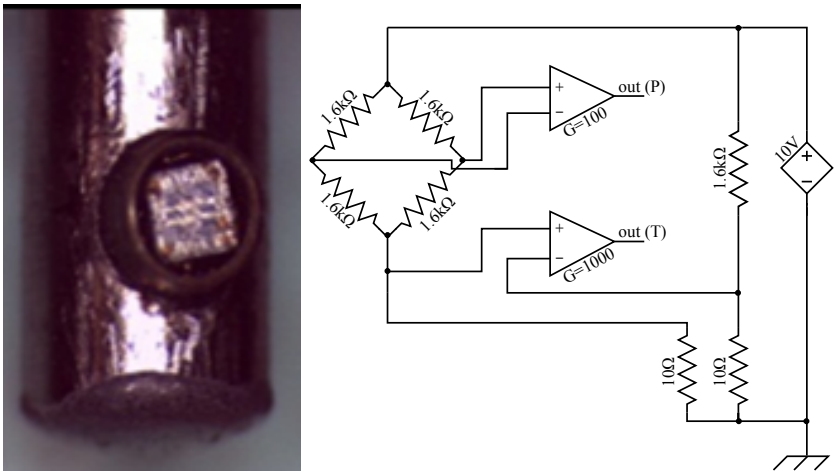


Figure 2.5.: Left: AP1-FP3 fast-response total pressure probe head. Right: Active compensation amplifier circuit diagram.

The use of a fast response pressure probe yields both time averaged values and time resolved ones, leading to the mean and time-resolved analysis of the flow topology. Thus it results to be suitable for the description of both rotating and fixed blade rows.

2.4.1.1. Probe frequency response

The typical spectrum retrieved with the probe in the VKI-R4 facility is reported in Figure 2.6. The power spectral density reported is computed from an acquisition sampled at 1 MHz and for a time of 0.3 s. The frequency resolution obtained is 0.95 Hz.

The sensor natural frequency is visible at approximately 300 kHz, however, given the spectrum amplitude reduction at around 80 kHz, the bandwidth is limited to this value. The blade passing frequency (BPF) appears at approximately 10 kHz so that the probe is able to detect up to 5 BPF harmonics, with which it is possible to provide and accurate representation of the flow field.

The hump visible prior to the sensor's natural frequency is likely to be due to the propagation of the acoustic waves through the corners of the shield surrounding the sensor, as sketched in Figure 2.7. In this hypothesis

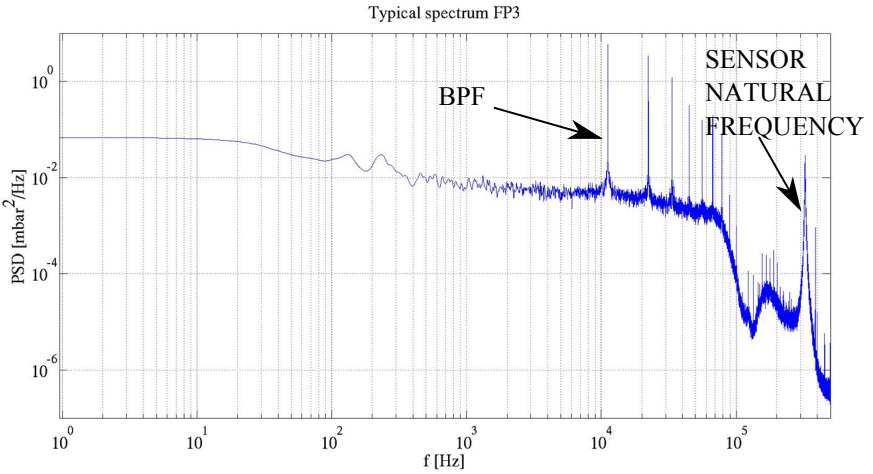


Figure 2.6.: Typical spectrum retrieved with the FP3 probe in the VKI-R4 facility.

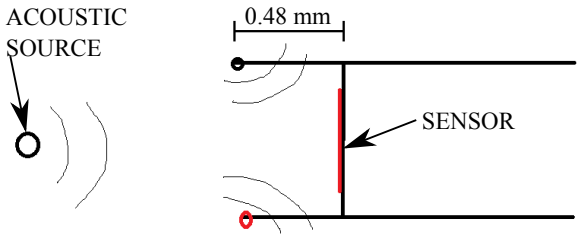


Figure 2.7.: Acoustic propagation of waves on the probe head in the bandwidth 120-220 kHz.

the corners are reflecting the frequencies in the bandwidth 120-220 kHz, amplifying them. The wavelengths indeed would correspond to the shield thickness (0.48 mm).

The amplitude reduction visible at approximately 80 kHz has only a theoretical explanation, while an experimental proof would be required.

An effect of the electronics was discarded as this amplifier was already used in other applications with different probes without exhibiting such behavior.

It was then hypothesized that the slope is due to the turbulence decay. The highest slope for a turbulence decay retrieved with a pressure measurement is -11/3 [87], while in this case the value obtained is more than three times higher and different values appear for different conditions (rpm, blade height, axial location).

On the other hand the region between 80 and 100 kHz results to be in a frequency range where the waves might not be compact: in case it is

considered a shallow cavity with tangential flow, the critical wavelength is $4D$ which corresponds to 80 kHz [88], while if it is considered a pipe (neglecting the short length), the critical wavelength corresponds to $2D$ [89], which in this case is around 100 kHz.

The amplitude reduction therefore is attributed to the interaction between the flow field and the cavity, which act as a low-pass filter for frequencies below 80 kHz.

The lack of an experimental definitive proof points out the necessity to introduce in the common practice the shock tube test of the probes before any application of these instruments. This would allow a good knowledge of the probe independently on the environment and eventually to distinguish an effect of the probe geometry in the measurements in a test-rig.

2.4.1.2. Static calibration and uncertainty

As previously explained, the active compensation amplifier in use yields two outputs V_p and V_s, corresponding to pressure and temperature. The corresponding pressure and temperature values can then be retrieved by applying a systematic calibration with respect to both quantities. The probe is inserted into a calibration chamber, connected to a pressure calibrator, together with two calibrated thermocouples (K-type) used as a reference. The chamber is then placed in a thermostatic oil bath. The calibration is performed within an envelope of 800:100:1600 mbar (absolute) in pressure and 20:10:60°C in temperature. A 14-bit acquisition system set to a sampling frequency of 50 kHz is utilized.

The obtained calibration data is fitted onto two separate polynomial surfaces given in eqs. (2.24) and (2.25), where c_i are polynomial coefficients. In order to provide a better fit a second order temperature dependency (V_s^2) is required to warp the surface, thus an additional cross term appears in the equations (i.e. third term in both equations).

$$P = c_1 + c_2 \times V_p + c_3 \times V_s \times V_P + c_4 \times V_s + c_5 \times V_s^2 \tag{2.24}$$

$$T = c_6 + c_7 \times V_p + c_8 \times V_s \times V_p + c_9 \times V_s + c_{10} \times V_s^2 \tag{2.25}$$

2.4.1.3. Uncertainty calculation on the static calibration

Reference thermocouples

The thermocouple calibration data is fitted onto a line of the form $T = slope \times V + offset$.

A mercury thermometer is used as a reference and it has an uncertainty of $\pm 0.058°$ C (computed as the resolution (0.5°C) divided by the square root of 3, as in a digital instrument), with infinite degrees of freedom (taken as 1 million instead of infinity for practical purposes, allowing to obtain a finite value) as no information on the calibration procedure is provided. For

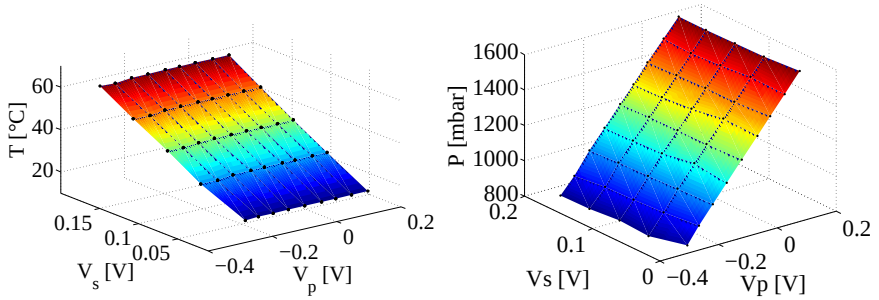


Figure 2.8.: Temperature (left) and pressure (right) calibration surface fits – dots indicating actual calibration points

each of 8 ($N = 8$) data points used for calibration, the deviation from the obtained line fit with two coefficients ($K = 2$) is fed into eq. (A.2) in order to estimate the random uncertainty. The degrees of freedom for this fit are calculated as $N - K = 6$.

The Welch-Satterthwaite equation given in eq. (A.5) yields a combined degree of freedom of 71 for each of the reference thermocouples used. For practical purposes, the t_{95} for degrees of freedom values over 30 is assumed to be 2 where the actual value for infinite degrees of freedom is 1.96 (see Fig.A.1). The expanded uncertainty for each thermocouple is calculated using eq. (A.4) and is found to be $\pm 0.137°C$ and $\pm 0.138°C$ respectively.

As the two thermocouples are used in combination to determine the chamber temperature as $T = (T_{K1} + T_{K2})/2$, the uncertainty values for individual thermocouples are propagated as given in eq. (2.26) resulting in a total uncertinty value (U_{TC}) of 0.054°C, where the third term accounts for correlated uncertainties as the same reference (mercury thermometer) is used for calibration of the two thermocouples. The combined degrees of freedom are once again calculated using eq. (A.5), and a value of 32767 is found resulting in a t_{95} value of 2. The expanded uncertainty for the combination of two thermocouples ($U_{95_{TC}} = \pm t_{95} \times U_{TC}$) is then computed as $\pm 0.108°C$. This value being lower than that of individual thermocouples highlights the advantage of using more than one instrument measuring the same quantity.

$$U_{TC} = \sqrt{\left(\frac{\partial T}{\partial T_{K1}} U_{T_{K1}}\right)^2 + \left(\frac{\partial T}{\partial T_{K2}} U_{T_{K2}}\right)^2 + 2\left(\frac{\partial T}{\partial T_{K1}}\right)\left(\frac{\partial T}{\partial T_{K2}}\right) U_{T_{K1}} U_{T_{K2}}} \tag{2.26}$$

Temperature calibration of the probe

As the miniaturized piezoresistive sensor used in the pressure probe is sensitive to both temperature and pressure, the data acquired during the static calibration of the pressure probe is fit into a polynomial equation given in eq. (2.25), and the calibration surface shown in Figure 2.8 (left) is

obtained.

Although the temperature dependency does not have a second-order character, such a definition is chosen in order to obtain a product of two independent variables ($c_8 \times V_s \times V_p$) which allows to warp the data-fit surface in order to obtain a better fit. For each of the 45 calibration points, the difference between the measured value of T has been subtracted from the same obtained from the surface fit at measured V_p, V_s values and fed into eq. (2.4) in order to calculate the standard estimate of error and random uncertainty with $N = 45$ and $K = 5$.

The total uncertainty calculated for the two reference thermocouples ($U_{TC} = 0.054°C$) is taken as systematic uncertainty as they have been used as reference for temperature calibration. Combining systematic and random uncertainty values, total uncertainty for temperature is calculated as 0.056°C.

Following the calculation of combined degrees of freedom, the expanded uncertainty for 95% confidence interval is computed as ±0.112°C.

Pressure calibration of the probe

The same data used for temperature calibration of the probe is used to determine the pressure calibration.

Data is fit into an equation of the same form, given in eq. (2.24) yielding the calibration surface shown in Figure 2.8 (right), and the random uncertainties are computed. The uncertainty values of the two references used, a Druck DPI 610 pressure calibrator (U_{D610}=0.5 mbar) and a Druck DPI 150 precision pressure indicator measuring atmospheric pressure (U_{D150}=0.75 mbar), are combined in order to determine the systematic uncertainty on the absolute pressure (b_P=0.90 mbar).

The total uncertainty and the expanded uncertainty for 95% confidence interval are found to be 0.91 mbar and ±1.81 mbar respectively.

2.4.1.4. Aerodynamic calibration and uncertainty

In order to exploit the aerodynamic characteristics of the probe in virtual three-hole mode, an aerodynamic calibration determining the pressure recovery of the single sensor unsteady probe with respect to yaw angle is essential.

The aerodynamic calibration is performed in the VKI-C4 open jet calibration facility, where the Mach number is controlled by regulating the pressure in a reservoir upstream the jet nozzle. The probe is yawed, i.e. rotated around the shaft as illustrated in Figure 2.9, using a programmable angular traverse system equipped with step motors. Thanks to the open-jet configuration, the static pressure is equal to the ambient pressure, recorded using a Druck DPI 150 precision pressure indicator with a total uncertainty of U_{D150}=0.75 mbar. The nozzle is instrumented with four T-type reference thermocouples in order to measure the total temperature and eight pressure taps connected to a variable reluctance pressure transducer measuring

the chamber pressure which has a total uncertainty of 1.82 mbar and an expanded uncertainty for 95% confidence interval of ±4.11 mbar.

The calibration is performed between yaw angles of -80° and 80° with increments of 2° at Mach numbers of 0.2, 0.3, 0.5 and 0.7. The calibration information gathered is presented in terms of pressure recovery coefficient plotted in Figure 2.9 for M=0.7, which yields a value of 1 for total pressure and 0 for static pressure measured by the probe and defined in eq. (2.27), where P_s is the ambient pressure, P_{0_p} is the pressure measured by the probe and P_0 is the total pressure.

$$C_{p_0} = \frac{P_{0_p} - P_s}{P_0 - P_s} \tag{2.27}$$

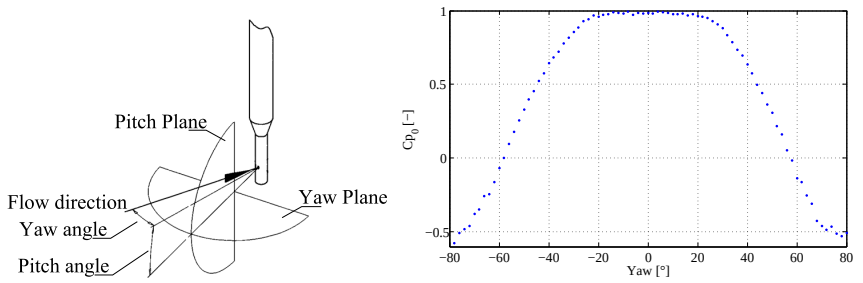


Figure 2.9.: Right: Illustration of yaw and pitch axes of a pressure probe. Left: Pressure recovery coefficient of the AP1-FL3 at M=0.7.

Aerodynamic calibration uncertainty

The uncertainty on the pressure recovery coefficient C_{p_0} is a function of the total pressure measured by the probe, the reference total pressure and the static pressure requiring the propagation of estimated uncertainties on these references as the *systematic uncertainty* term using eq. (2.28). The static calibration total uncertainty of the probe is calculated as $U_{P_{0_p}}$ =0.91 mbar as already presented in the last paragraph. While the uncertainty on the static pressure measured by a Druck DPI 150 precision pressure indicator (VKI atmospheric pressure server) is given as $U_{D150} = U_{P_s}$ =0.75 mbar, the total uncertainty on the total pressure measured using a variable reluctance transducer is estimated as U_{P_0} =1.82 mbar.

$$b_{C_{p_0}} = \sqrt{\left(\frac{\partial C_{p_0}}{\partial P_{0,p}} U_{P_{0_p}}\right)^2 + \left(\frac{\partial C_{p_0}}{\partial P_0} U_{P_0}\right)^2 + \left(\frac{\partial C_{p_0}}{\partial P_s} U_{P_s}\right)^2} \tag{2.28}$$

In order to determine the *random uncertainty* on the aerodynamic calibration, the pressure recovery coefficient data obtained is fit on to a curve of the form given in eq. (2.29).

$$c_{P_{0_{fit}}} = \sum_{i=1}^{8} a_i Sin(b_i\phi + c_i) \tag{2.29}$$

In this case, for c_{P_o} the *standard estimate of error* (SEE) and the *random uncertainty* is calculated as shown in eq. (2.30), where N =80 and K =24.

$$SEE_{c_{P_0}} = \sqrt{\frac{\sum_{i=1}^{80}(c_{P_{0_i}} - c_{P_{0_{fit}}})^2}{N-K}} \qquad s_{c_{P_0}} = \frac{SEE_{c_{P_0}}}{\sqrt{N}} \tag{2.30}$$

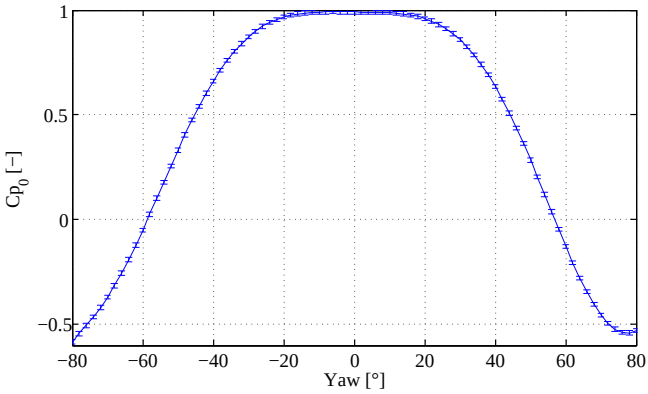


Figure 2.10.: Pressure recovery coefficient of the AP1-FL3 at M=0.7 together with expanded calibration uncertainties.

Once the systematic and random uncertainty terms are obtained, the *total uncertainty* (U_T) and the *expanded uncertainty* for 95% confidence interval (i.e. 2σ) are calculated, where t_{95} denotes the appropriate value of the two-sided *t-distribution* for 95% confidence interval. In order to determine the student's t (t_{95}) value required to compute the expanded uncertainty, the combined degrees of freedom must be computed using Welch-Satterthwaite equation. In short, the Welch-Satterthwaite equation combines the degrees of freedoms of systematic and random uncertainty sources (ν_i).

Once the Welch-Satterthwaite equation is solved, the value is truncated in order to determine the degrees of freedom for the combined system. Following this step, the appropriate value of student's t (t_{95}) may be found using two-sided t-distribution table for 95% confidence interval as already explained in the previous part.

The degrees of freedom calculated for uncertainty on pressure recovery coefficient are found to be higher than 30, yielding a t_{95} value of 2. The expanded uncertainties for 95% confidence interval for the total pressure recovery coefficient at four Mach numbers (0.2, 0.3, 0.5, 0.7) are computed

as ±0.14, ±0.058, ±0.019, ±0.0094 respectively. In Figure 2.10, the obtained curve fit together with its expanded uncertainty is presented for M =0.7.

2.4.1.5. Total pressure distribution detected experimentally

The time averaged pressure distribution along the radial traverse at the rotor outlet retrieved with the FP3 probe is employed as a reference for the numerical simulations. The measured traverses are presented in Figure 3.9 at both the design and the near stall conditions with the corresponding errorbars, and are compared to the corresponding outcomes from the numerical simulations. They both point out a hub loaded blade row. The description of the blade row is provided in the next chapter (3.2.2).

The measurement uncertainty is following the ASME method, as the calibration uncertainty of the instrumentation. The total uncertainty value obtained for the static calibration is taken as the systematic uncertainty term for measurement uncertainty estimation as all errors and uncertainties during calibration will be carried into measurements. Concerning the random uncertainty term, it is imperative to ensure that the acquired data does not substantially deviate from a Gaussian (or normal) distribution. In order to identify departures from normality such as outliers, skewness and kurtosis, *normal probability plots* are typically used. In order to obtain the normal probability plot, data is first sorted in ascending order, followed by assigning median ranks to each data using Bernard's formula given in eq. (2.31), where $P_{50\%}$ denotes 50% median rank while i and N stands for data index and number of data points. Finally the inverse of the normal cumulative distribution function (CDF) is calculated using the corresponding mean and standard deviation at the corresponding probabilities ($P_{50\%}$).

$$P_{50\%} = \frac{i - 0.3}{N + 0.4} \tag{2.31}$$

In order to take into account the uncertainty variations due to the flow field, the uncertainty is at first computed on a phase locked average (PLA), which provides the representation of the typical blade passage (see Figure 3.15). The explanation of this post-processing technique is shown in Appendix B.1. The averaged blade passage at a certain span height is divided in a number of points called "classes", resulting from the average of the data retrieved in that time interval in all the blade passages of an acquisition. In each class it is imperative to ensure that the acquired data do not substantially deviate from a normal distribution. The histogram and normal probability plot for two example classes around the middle of the blade passage from data acquired at mid-span and tip are presented in Figures 2.11 and 2.12. As for the time-averaged case, both probability plots exhibit a linear trend. For the presented classes, the skewness values are -0.0229 and -0.3361 while the kurtosis values are 0.1258 and 0.246 respectively.

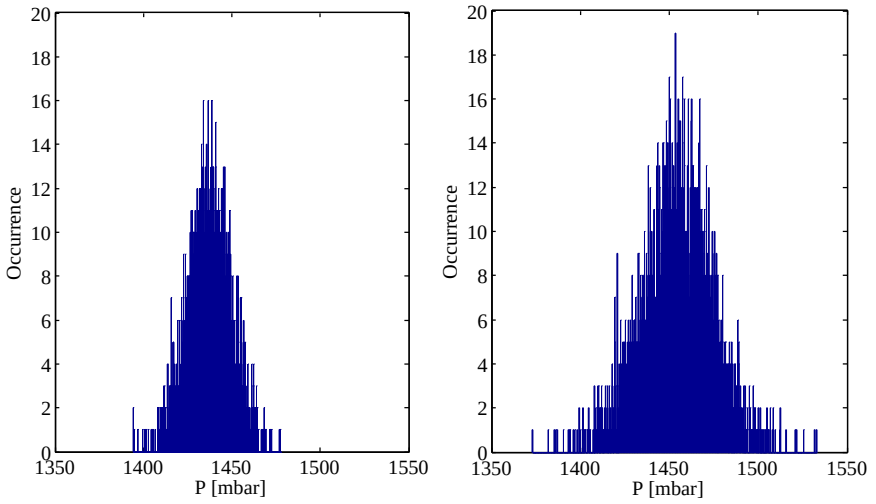


Figure 2.11.: Histogram of example PLA classes for data acquired at mid-span (left) and at tip region (right).

For the PLA procedure, the standard deviation may be estimated using P_{RMS} definition shown in eq. (B.1) which is equivalent to the definition given in eq. (A.1). The random standard uncertainty is then calculated as $P_{RMS}/\sqrt{N}$, with N being ∼3192 (=76×42) for PLA as explained before.

Combining the systematic and random uncertainty sources, the total uncertainty is obtained using eq. (A.3). The combined degrees of freedom are calculated using Welch-Satterthwaite equation and are found to be significantly higher than 30 yielding a t_{95} value of 2 for all classes in both averages. The expanded uncertainty values for the phase-locked average is presented in Figure 2.13.

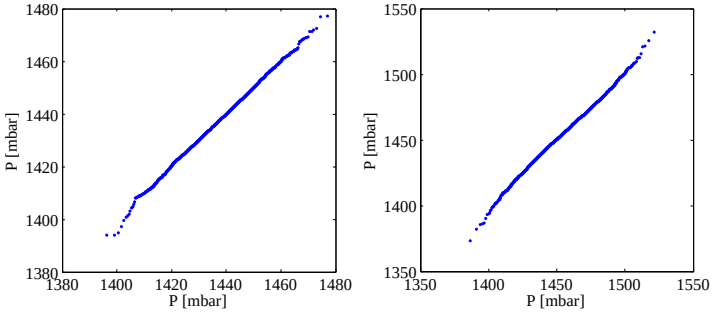


Figure 2.12.: Normal probability plot of example PLA classes for data acquired at mid-span (left) and at tip region (right).

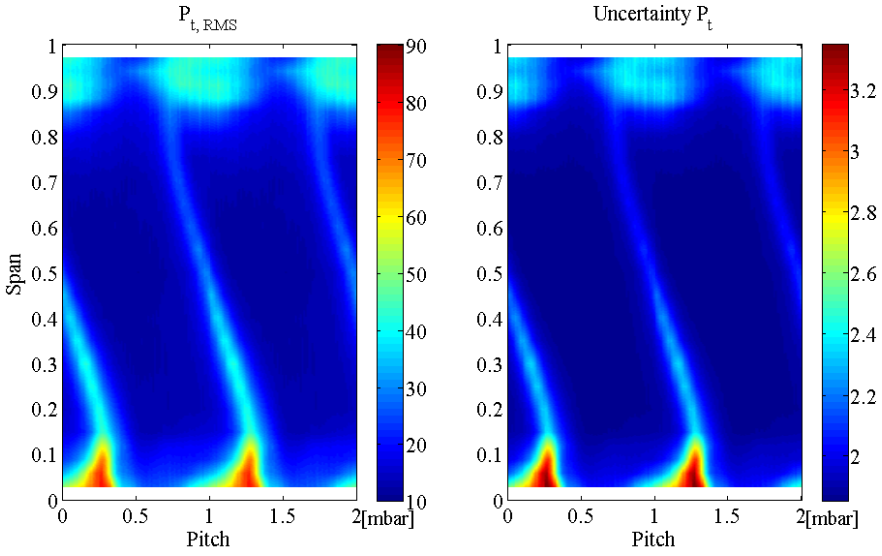


Figure 2.13.: P_{RMS} (left) and expanded uncertainty (right) maps (left) of the PLA presented over two blade passages.

Higher values of uncertainty are visible at regions with higher unsteadiness such as the blade wakes, tip leakage flows and hub corner separations. The PLA uncertainty represents approximately the 0.2% of the averaged total pressure measurement at midspan. The uncertainty calculation result therefore denotes the capability of the probe to provide the detailed representation of the flow field in this machine.

The uncertainty retrieved at each span height on the PLA allow to take into account the variations of the flow field, therefore each span value is averaged to obtain the errorbars presented in Figure 3.9. The uncertainty slightly increases in the zones of higher unsteadiness, however the discrepancies are very low as the systematic component is much higher than the random one, which is related to the flow field.

Probe application in a virtual three hole mode

The fast-response pressure probe FP3 has been employed in a virtual three-hole mode, in order to verify its capabilities for the detection of the rotor outlet yaw angle, Mach number, static pressure and corrected total pressure. This test has been performed at 96% Nn at design condition.

The angular characteristics of a single sensor probe can indeed be exploited to measure the unsteady yaw angle by yawing it at two symmetric angular positions. In this technique, called *virtual three-hole mode*, a single sensor probe is subsequently moved along traverses with different yaw angle settings, having recordings equivalent to the left and right hole of a direc-

tional three hole probe. This technique is therefore able to yield not only total pressure measurements, but also static pressure, Mach number and yaw angle distributions. As the recordings are done at different time intervals, the operating condition of the test facility must be stable. In order to perform the calculations, the unsteady data is reduced using a phase-locked average technique, and therefore periodic content of the signals recorded are analyzed, revealing the need of a proper trigger signal.

The center traverse has been aligned with the absolute velocity direction at the rotor exit at midspan, which corresponds to 35°. On the other hand the angular displacements of the virtual left and right holes are selected as 35° according to the angular insensitivity range of the probe, which corresponds to $\sim \pm 20°$. In order to determine the angular characteristics of the virtual three-hole probe, the aerodynamic calibration data obtained (and presented in terms of C_{p_0}, defined in equation 2.27) are shifted as shown in Figure 2.14, where C_{p_0} coefficient curves positioned in the left, the central and the right hole are presented at $M = 0.7$. As the virtual hole displacement is selected as 35°, with a calibration envelope of ±80°, the virtual hole mode calibration envelope is limited to ±45°.

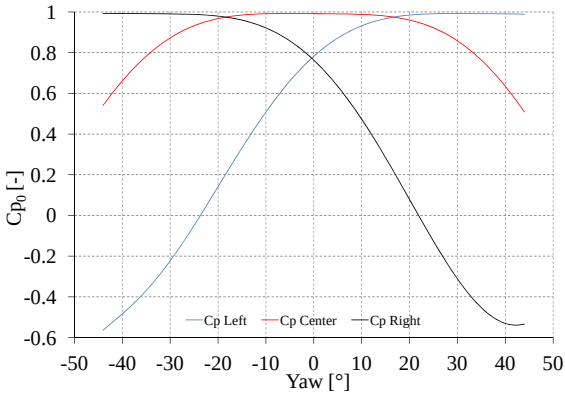


Figure 2.14.: The derived aerodynamic calibration curve (expressed in terms of C_{p_0}, defined in equation 2.27) of the virtual three-hole mode probe at M=0.7.

The probe application in virtual three-hole mode yields unsatisfactory results. The frequency analysis of the three traverses highlights a reduced bandwidth for the "left" and the "right" holes with respect to the central one from 70 to 25 kHz. The limitation is due to a wide spread hump, which has a peak at approximately 35 kHz. Figure 2.15 shows the result obtained for the acquisitions of the three traverses at midspan as an example.

The probe turning seems to cause the hump presence, it is therefore hypothesized to be due to the interaction between the probe cavity and the flow field.

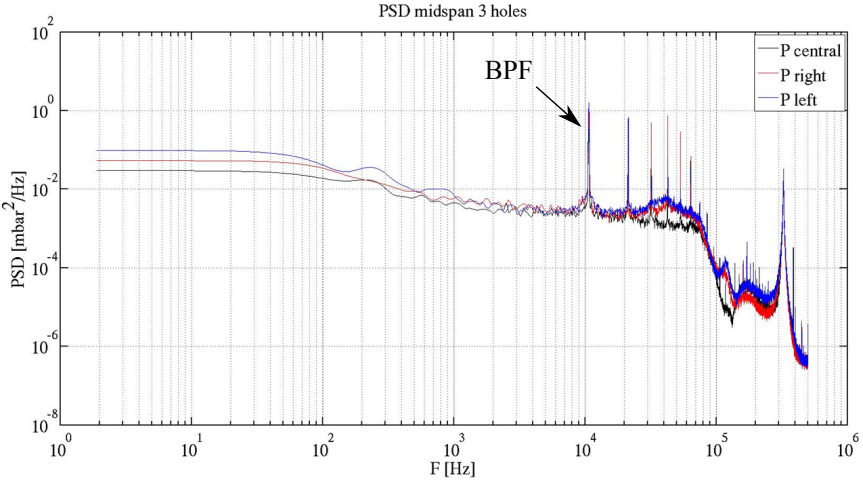


Figure 2.15.: Typical spectrum retrieved with the FP3 probe in the VKI-R4 facility.

In the previous paragraph (2.4.1) it is explained that the cylinder model (or deep cavity model) cannot be applied to the probe cavity. Indeed the calculation of the resonance frequency by employing either the Helmholtz or the deep cavity model would yield misleading results.

On the other hand it is well known (it was demonstrated by Tonon et al. [27]) that Rossiter modes can appear in presence of a shallow cavity. The tangential component of the flow field, parallel to the cavity, creates vortices of two species: those impacting on the endwall of the cavity and those in the cavity itself, the latter appearing with different modes. Figure 2.16 shows a sketch of this mechanism.

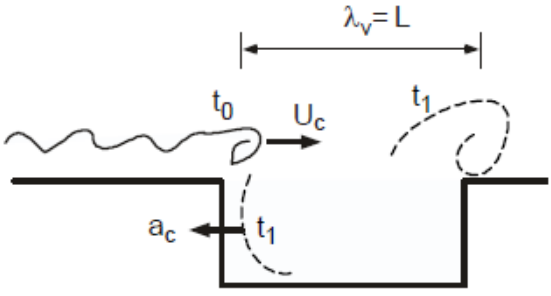


Figure 2.16.: Shallow cavity feedback to the Rossiter modes [27].

This model can be applied to the probe cavity, which, once turned at

$\pm 35°$ results to be similar to a shallow cavity with an impinging tangential flow. The frequency of the first Rossiter mode, which corresponds to the presence of one vortex in the cavity, is calculated from the definition of the Strouhal number, which has been found to be approximately equal to 0.4 in this condition [27]:

$$f = \frac{St \times U}{W_{eff}} \tag{2.32}$$

in this formula St is the Strouhal number (equal to 0.4), U is the tangential absolute velocity, W_{eff} is the effective width of the cavity, where it is considered the cavity diameter (equal to 1.1 mm).

The frequency obtained is approximately 35 kHz, which is in good agreement with the peak of the hump.

The probe therefore is not able to provide any additional informations on the flow field if utilized in virtual-three hole mode with this set-up. The signals in fact should be filtered at approximately 25 kHz in order to remove the effect of the hump. The filter would have the effect to limit the bandwidth at the first BPF harmonic, hence a filtered signal would provide a rough representation of the flow field topology. The flow angle distribution, together with the static pressure and Mach number ones result therefore not available in this experimental campaign.

The unsatisfactory result of the probe employment in a virtual three-hole mode seem therefore to be linked to the probe geometry. A different configuration, such as a cylindrical probe with a sensor protected by a cavity could represent a possible solution for this application.

2.4.2. Wall fast-response pressure sensors

The determination of the time resolved pressure levels in both the axial and the circumferential directions is fundamental not only for the detection of the stall cell(s) in the unstable range, but also for an appropriate description of the tip flow field in the stable operating points. The sensors cover an arc of 42° (K2 and K3 represent the two extremes and are located respectively at 80° and 38°) and are equally spaced by one rotor pitch. The sensors are axially displaced between plane 2 and plane 3 as shown in Figure 2.17. K14 is set in plane 2, while K15 in plane 3. The static pressure at the hub is retrieved in plane 3 and plane 4 by means of sensors located at 66°.

These sensors are 15 psi differential and are characterized by a passive compensation scheme, therefore they provide a single output voltage V_p proportional to the pressure measured.

Their signal is amplified with a gain of 100 and then connected to the acquisition system. As in the case of the probe, the sampling frequency is much higher than the sensor natural frequency, therefore no filter has been applied to the measurements.

The sensors are indeed characterized by a frequency higher than 200 kHz, as shown in Figure 2.18, which represents the typical spectrum retrieved in

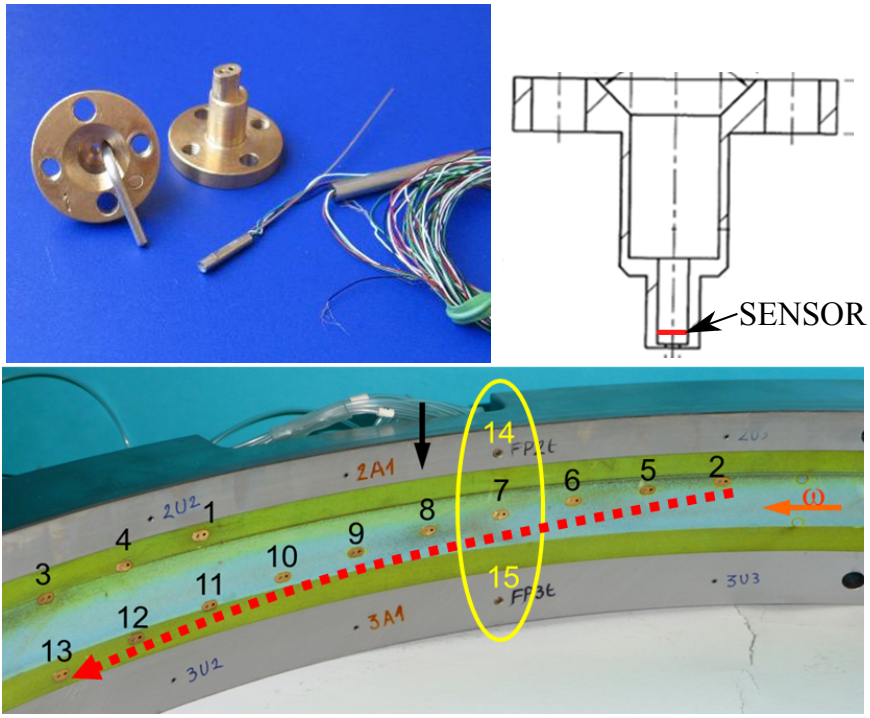


Figure 2.17.: Fast-response pressure sensors configuration and insert.

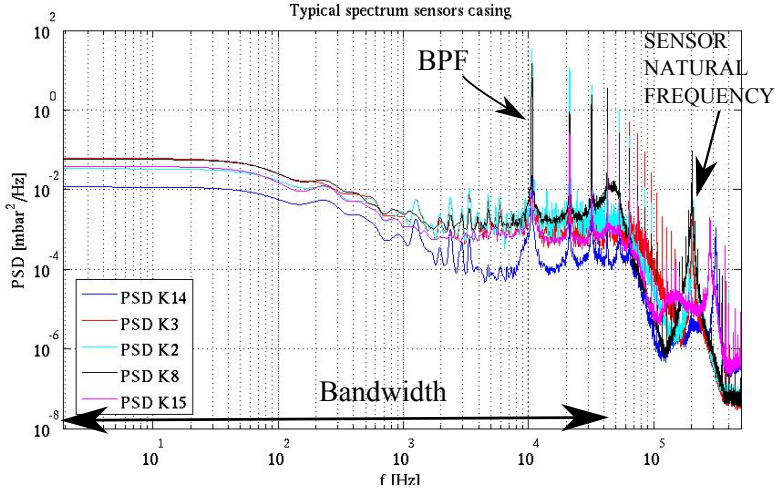


Figure 2.18.: Typical spectrum retrieved in the R4 facility with the fat-response pressure sensors on the casing.

the R4 facility. It is possible to distinguish the BPF (at approximately 10 kHz) and the resonance frequency of the sensor at around 200 kHz. The amplitude drop is preceded by a hump, which is attributed to the resonance of the cavity preceding the sensors: they are indeed contained in a metallic insert and protected by a cavity as shown in Figure 2.17. A shock tube test performed on a similar insert provides a bandwidth limitation to 60 kHz caused by the cavity.

As visible from the Figure 2.18 though, not all the sensors are the same. K14 and K15, which are respectively located at the rotor inlet and outlet (see Figure 2.17), are 25 psi absolute. Their natural frequency is therefore higher than the other sensors and corresponds to approximately 300 kHz.

The sensors are calibrated in situ by pressurizing the loop.

They are characterized by an uncertainty of ± 1.2 mbar, computed with the ASME method.

2.5. Measurements employed as reference for the blade row numerical characterization

The quality of the computations performed for the characterization of the three blade rows has been assessed by comparing the numerical output with the experimental global performance. Pneumatic probes and thermocouples traversing is chosen for this evaluation as they enable a more accurate description of the spanwise distribution, which is also employed as boundary condition for the computations.

This section describes the instrumentation adopted together with the methodology utilized for the global performance calculation.

2.5.1. Temperature measurements

The temperature profiles at the stage inlet and outlet are detected with T-type Kiel thermocouple probes traversed in plane 1 and plane 4.

Likewise the thermocouples contained in the rakes, they are connected to the temperature scanner, following the same acquisition chain.

The recovery factor profile retrieved for these probes is shown in Figure 2.19.

The uncertainty is quantified with the methodology employed for the rakes thermocouples and the t95 uncertainty results to be comprised between 0.7 and 0.75 K, increasing with the Mach number.

2.5.2. Pressure measurements

Static pressure measurements

The static pressure is retrieved with pressure taps, which employ the acquisition chain adopted for the rakes measurements. At each measurement

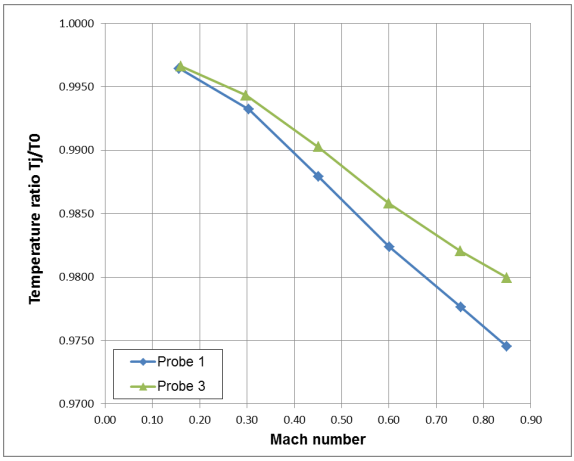


Figure 2.19.: Recovery factor calibration for the thermocouple probes employed in plane 1 and plane 4.

plane five ports are located at both the hub and the casing. The spanwise pressure distribution is obtained by linearly interpolating the mean hub and the casing measurements. This trend has previously been verified by Sans et al.[67]. The uncertainty refers to the one of the inlet pressure transducer for the measurements in planes 1 and 2, to the one of the outlet transducer for those in planes 3 and 4.

Total pressure measurements: kiel and three-hole probe

The inlet and outlet total pressure spanwise distributions are detected with pneumatic pressure probes: a kiel probe in plane 1 and a three-hole probe in plane 4. The former is connected to the scanner employed for the inlet rakes, the latter to the scanner of the outlet rakes.

The kiel head has the advantage of providing measurements insensitive to the flow angle within a certain angular range. The probe has been calibrated in the VKI-C4 facility and the insensitivity range results to be comprised within $\pm 30°$, as shown in Figure 2.20, right.

The kiel probe is following the acquisition chain employed for the inlet rakes, yielding an equal uncertainty value.

The three-hole probe is employed in plane 4. It consists of a head with three parallel tubes, as shown in Figure 2.21. The central hole is cut perpendicularly while the left and the right holes at $45°$.

The three holes allow the detection of both the yaw angle and the total pressure, by applying an iterative procedure based on two coefficients which are Mach and yaw angle dependent and are retrieved by angular calibration.

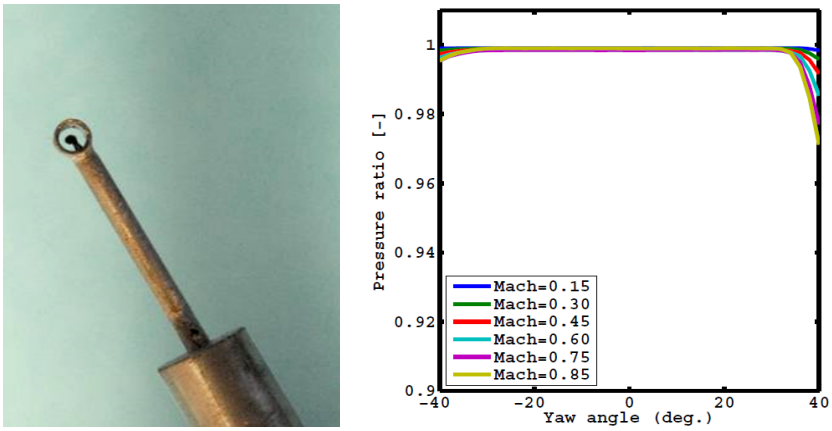


Figure 2.20.: Left: Kiel pressure probe. Right: Kiel probe angular calibration.

The coefficients are defined as:

$$K_{yaw}(\alpha, Mach) = \frac{P_L - P_R}{P_C - \frac{P_L+P_R}{2}} \tag{2.33}$$

$$K_{tot}(\alpha, Mach) = \frac{P_{T,ref} - P_C}{P_C - \frac{P_L+P_R}{2}} \tag{2.34}$$

in these formulas P_C, P_L and P_R represent respectively the pressure detected by the three-hole probe with the central, the left and the right holes, $P_{T,ref}$ the reference total pressure in the chamber.

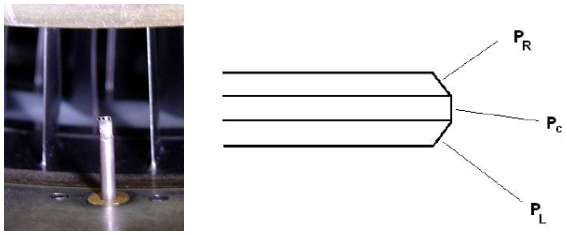


Figure 2.21.: Three-hole pressure probe.

The calibration covers an angular range $\pm 25°$, acquired with steps of $2°$, and Mach numbers ranging from 0.15 to 0.85, detected with steps of 0.1. Figure 2.22 shows the curves obtained.

Once defined the coefficients in the calibration, the iterative procedure can be applied with the measurement data to retrieve the yaw angle and the total pressure at the stator outlet. The loop starts with initial values of

K_{yaw} and Mach (computed from the measured P_C and the static pressure retrieved with the taps), the K_{tot} is then calculated and therefore a new value of total pressure and Mach number. Convergence is reached on an imposed threshold on the Mach number.

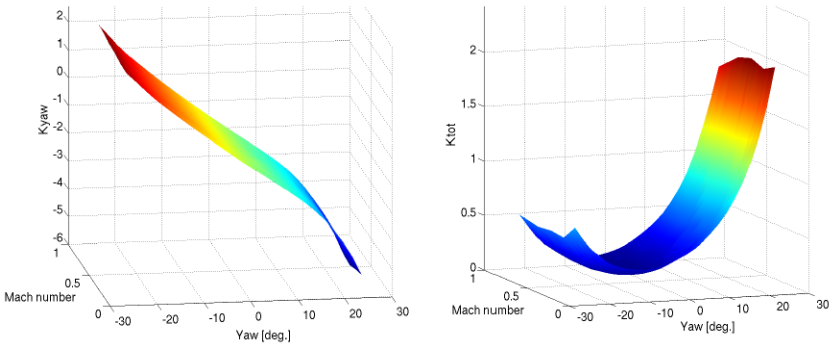


Figure 2.22.: Three-hole probe calibration coefficients K_{yaw} and K_{tot}.

Uncertainty on the three-hole probe measured quantities The uncertainty on the total pressure and yaw angle retrieved with the three hole probe follows the iterative procedure to obtain these measured quantities, explained in the previous paragraph.

The yaw angle measurement depends on the corresponding K_{yaw} coefficient and Mach number, as it is retrieved on the map shown in Figure 2.22:

$$\alpha = f(Mach, K_{yaw}) \tag{2.35}$$

The uncertainty contributions derive on both the calibration and the test data:

$$\delta\alpha = \sqrt{(\delta\alpha_{calib})^2 + (\delta\alpha_{test})^2} \tag{2.36}$$

The calibration uncertainty is computed as the SEE of the regression curve represented in Figure 2.22, obtaining a value $\delta\alpha_{calib} = 0.25°$. The test uncertainty derives from the contributions of the K_{yaw} and Mach number, it is computed as:

$$\delta\alpha_{test} = \sqrt{(\frac{\partial\alpha}{\partial K_{yaw}}\delta K_{yaw})^2 + (\frac{\partial\alpha}{\partial Mach}\delta Mach)^2} \tag{2.37}$$

The Mach number uncertainty value is retrieved as shown in paragraph2.3.1. The δK_{yaw} can be calculated as follows, where D represents the denominator of the K_{yaw} coefficient:

$$\delta K_{yaw} = \sqrt{(\frac{1}{D}\delta P_L)^2 + (-\frac{1}{D}\delta P_R)^2 + (-\frac{P_L - P_R}{D^2}\delta D)^2} \tag{2.38}$$

the uncertainty on the denominator is:

$$\delta D = \sqrt{(\delta P_C)^2 + (-\frac{1}{2}\delta P_L)^2 + (\frac{1}{2}\delta P_R)^2} \tag{2.39}$$

The three pressures P_c, P_L and P_R are connected to the same scanner, yielding an uncertainty $\delta P_L = \delta P_R = \delta P_c = 0.54$ mbar.

The uncertainty on K_{tot} is similarly computed and it is employed to retrieve the uncertainty on the total pressure measurement. The K_{tot} coefficient also depends on the yaw angle and the Mach number. The uncertainty results to be:

$$\delta K_{tot} = \sqrt{(\delta K_{tot,calib})^2 + (\frac{\partial K_{tot}}{\partial \alpha}\delta\alpha)^2 + (\frac{\partial K_{tot}}{\partial Mach}\delta Mach)^2} \tag{2.40}$$

in which the sensitivities derive from the calibration procedure. The total pressure uncertainty can be finally retrieved:

$$\delta P_{tot} = \sqrt{(\delta P_c)^2 + (D\delta K_{tot})^2 + (K_{tot}\delta D)^2} \tag{2.41}$$

These values are employed to calculate the uncertainty on the Mach number 2.13. Thus new values of uncertainties on α, K_{yaw}, K_{tot} and total pressure can be computed, until reaching the loop convergence as in the case of the yaw angle and total pressure result.

The final values obtained are $\delta\alpha = 0.5°$ and $\delta P_{tot} = 2.5$ mbar. The total pressure uncertainty retrieved with the three hole probe yields, together with the one of the kiel probe employed at the stage inlet, to an uncertainty on the total-to-total pressure ratio of approximately 0.24% on the value at design condition at 100% Nn.

The uncertainty on the efficiency value retrieved with the probe traversing approximately corresponds to the one obtained with the rakes, as the highest contribution is due to the temperature measurements, which follow the same acquisition chain of the rakes.

2.5.3. Global performance assessments

The pressure and temperature measurements described in the previous sections are employed for the determination of the global performance of the stage, and they are utilized as reference for the computations describing the behavior of the single blade rows.

The total pressure and temperature radial traverses have been performed by acquiring data on 23 points, as shown in Figure 3.1 (right).

The various profiles are integrated along the span in order to obtain the total pressure ratio, the mass flow and the efficiency of the stage. All the quantities are mass flow averaged.

Chapter 3.

Characterization of the stable operating range

The stability limit of a compressor depends on the compressor characteristic and on the flow structures appearing in the stable range. Their presence is due to several parameters among which the geometry of the blades (hub/tip ratio, aspect ratio, etc.), the clearance, the loading distribution.

The investigation on the Dream compressor targets the unstable regime, therefore the study of the stable operating points is performed not only to have a better understanding on the loading distribution on the stage, but also to have an insight on the flow structures contributing to the formation of the unstable mechanisms.

The performance map is retrieved with steady instrumentation, while numerical simulations are employed for the performance of the single blade rows. As the focus of this project is on the unsteady flows and the rotor represents the main source of unsteadiness, the rotor blade row is analyzed at design and at near stall conditions at 100% Nn, using time-resolved pressure measurements on the casing and at the outlet. The stator blade row is characterized only at design operating point (at 100% Nn) utilizing time-resolved pressure measurements at its outlet.

The investigation presented in this chapter allows to define the compressor characteristic, to locate the three-dimensional separations in the various blade rows, and to identify the precursors of the flow structures developing in the unstable range.

3.1. Experimental set-up employed in the stable operating points

The experimental set-up employed for the characterization of the stable operating points refers to the one described in section 2.1.3: rakes in Planes 0 and 4 continuously monitor the performance of the stage sampling at 2 Hz, while fast-response pressure sensors detect the rotor tip flow, the hub rotor and stator outlet. In addition to this a fast-response pressure probe retrieves total pressure measurements at the rotor and at the stator outlet. The probe utilized has been described in section 2.4.1.

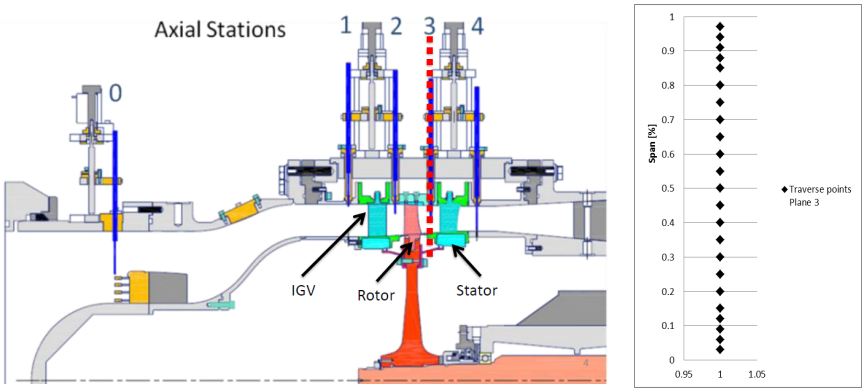


Figure 3.1.: Left: sketch of the rotor outlet traversing. Right: measurement location along the radius at the rotor outlet.

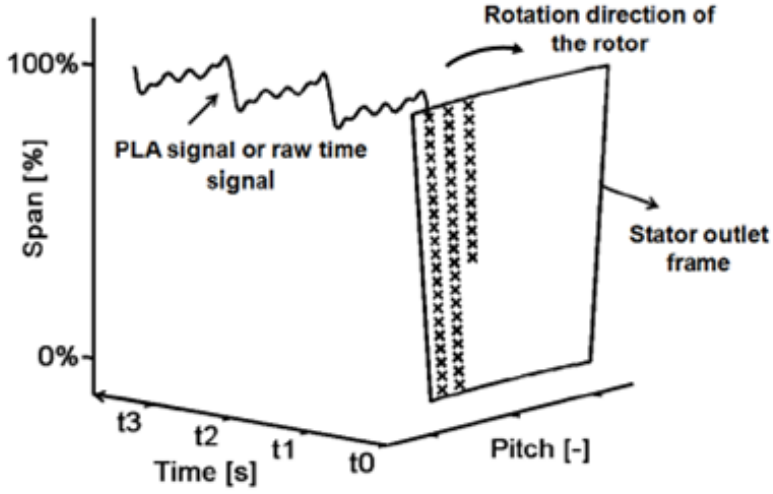


Figure 3.2.: Sketch of the measurement matrix retrieved at the stator outlet with the circumferential and radial traversing of the fast response pressure probe.

Regarding the detection of the rotor flow field, the probe radial traversing system is sketched in Figure 3.1 (left), and the probe is located at 90° (see Figure 2.3). The data are acquired in 23 measuring points, as sketched in Figure 3.1, right. The hub and the tip regions, where the three-dimensional separations appear, are detected with a higher refinement.

The time-resolved data, which include both the probe and the sensors

measurements, are recorded at F_s=1 MHz for 0.3 s (300,000 samples), providing samples containing approximately 42 rotor revolutions.

The detailed characterization of the stator flow field requires both circumferential and radial probe traverses, which are performed moving alternatively the probe and the stator (and IGV) blade row. The measurement frame covers 3 stator pitches in 31 circumferential and 19 radial positions, which means 589 measurements.

These measurements allow the representation of the total pressure time evolution across 3 stator blade passages, as shown in the sketch in Figure 3.2.

3.2. Global performance of the stage

3.2.1. Performance map

The Dream compressor stage performance map retrieved with the rakes is presented in Figures 3.3, 3.4, respectively in terms of static-to-total and total-to-total pressure ratio.

The performance map expresses the abscissa in terms of corrected mass flow, which is defined with respect to the standard conditions ($T_{standard} = 288.15K$ and $P_{standard} = 101325Pa$):

$$\dot{m}_{corrected} = Q_m \sqrt{\frac{\frac{TT0M}{T_{standard}}}{\frac{PT0M}{P_{standard}}}} \tag{3.1}$$

and then normalized with respect to the design conditions at 100% Nn.

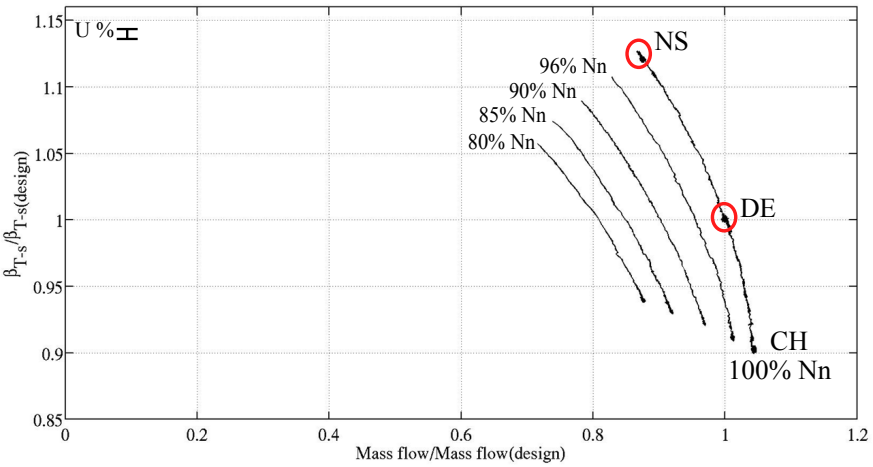


Figure 3.3.: Stage total to static performance map retrieved with the rakes in the stable operating points.

The stage detailed characterization, performed with radial traverses of time-resolved pressure measurements at the rotor outlet, is available at three operating conditions, which are choke (CH), design (DE) and near stall (NS)at three rotational speed: 90, 96 and 100% Nn. However in this chapter only the design and near stall conditions at 100% Nn will be analyzed. In the Figures 3.3, 3.4 they are represented with a red circle.

For the sake of clarity the choke operating condition merely indicates the one of maximum mass flow, whereas it does not correspond to the definition of "choke" often found in the literature (e.g. Griepentrog [90]), in which the maximum mass flow is reached for the presence of a sonic line in the blade passage.

The stall inception mechanism varies from high to low speed. This topic will be analyzed thoroughly in the next chapter.

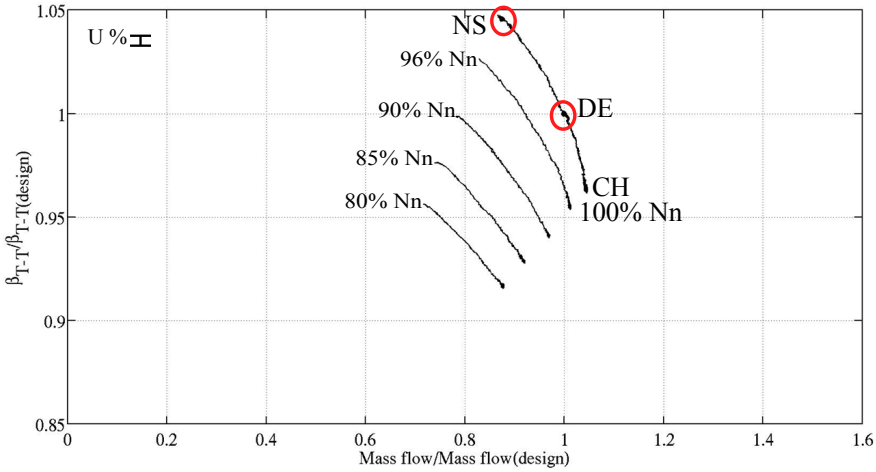


Figure 3.4.: Stage total to total performance map retrieved with the rakes in the stable operating points.

3.2.2. Performance of the single blade rows

Experimental data are not available at all the measuring planes, therefore the performance of the single blade rows is retrieved using numerical simulations. In order to be consistent as much as possible with the experimental data, the representation is provided in the four measurement planes. The approximations due to the rotor/stator modeling of a RANS simulation want therefore to be avoided, and the effect of unsteady phenomena which directly impact on the performance of compressors need to be tackled, thus the choice of the Non-Linear Harmonic method simulation type. In fact it is able to take into account the unsteadiness of the flow field without requiring

the computational time of a URANS [91], [92]. This method is implemented in Numeca Fine Turbo 9.0.3 solver.

The Non-linear Harmonic method is able to consider the unsteadiness as it represents the various quantities characterizing the flow field as a sum of a time-averaged term and a time dependent one, the latter being Fourier decomposed in time:

$$U(\vec{r},t) = \bar{U}(\vec{r}) + \sum U'(\vec{r},t) = \bar{U}(\vec{r}) + \sum_{k=1}^{N} (\widetilde{U}_k(\vec{r}) e^{(I\omega_k t)} + \widetilde{U}_{-k}(\vec{r}) e^{(I\omega_{-k} t)}) \tag{3.2}$$

The Fourier discretization represents only the blade passing frequency and a number of BPF harmonics selected by the user: a higher number yields a better representation of the flow field, though implies a more refined mesh and thus a higher computational time and memory.

The numerical data are validated through an experimental comparison, then they are analyzed with the spanwise distributions of total pressure and temperature, flow angle and entropy, concluding with a temperature-entropy diagram.

3.2.2.1. Numerical set-up

Numerical domain

The resolution of the equations in the frequency domain allows to employ a single blade passage per row in the computational domain. Thus the stage is represented as shown in Figure 3.5. The numerical domain covers the machine from its inlet to its outlet including the measurement planes 1 and 4 identified in the experimental set-up.

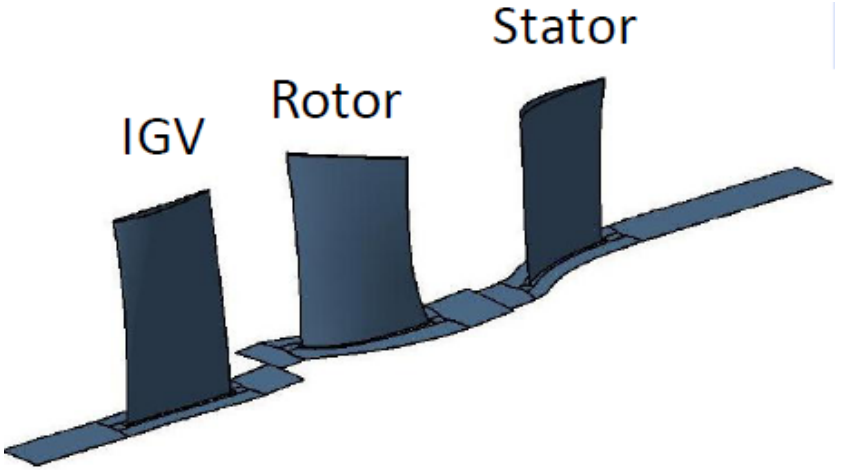


Figure 3.5.: Numerical domain employed in the simulations.

Quality assessments of the simulation

The non-linear harmonic method, in order to provide an accurate representation of the BPF and its harmonics, requires a mesh which has to be discretized according to the following criteria.

The number of nodes in theta direction for the element located upstream of the interface $N_{\theta,u}$ has to be:

$$N_{\theta,u} \geq 30N\frac{n_d}{n_u} \tag{3.3}$$

while for the one downstream $N_{\theta,d}$:

$$N_{\theta,d} \geq 30N\frac{n_u}{n_d} \tag{3.4}$$

In these two conditions N stands for the number of harmonics selected, n_u and n_d for the number of blades located respectively upstream and downstream of the interface.

The grid quality has been evaluated via comparison of RANS simulations with the performance retrieved experimentally (presented in Section 2.5.3).

As the focus of the study is the unstable regime, the grid quality is assessed in the near stall condition.

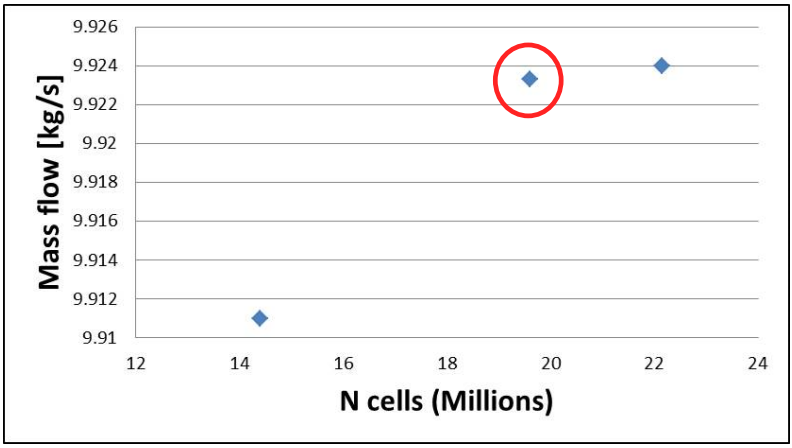


Figure 3.6.: Mesh sensitivity analysis and grid chosen (red circle).

In order to achieve an appropriate experimental-numerical comparison, the data are extracted from the numerical solution at the same location of the experimental acquisitions, and the same calculation procedure employed for the experimental data is applied to obtain the global performance.

The results and the relative errors are presented in table 3.1.

Figure 3.6 compares the flow rate obtained with the three-grids utilized in the sensitivity analysis. The mesh with 19.6 M cells is selected as the convergence on the mass flow is reached.

The grid selected is described in the following paragraph.

Table 3.1.: Mesh sensitivity analysis.

	$\dot{m}_{rel.err.}[\%]$	$\pi_{rel.err}[\%]$	$\eta_{rel.err.}[\%]$
Exp. data	-	-	-
14 M cells	1.390	-0.030	-1.510
19 M cells	1.270	-0.188	-1.676
22 M cells	1.260	-0.050	-1.570

Grid details

The mesh is generated with the module Autogrid5 of Numeca FINE Turbo. The span is discretized with 129 nodes on the rotor blade row and 97 on the IGV and stator blade rows. An O4H grid is utilized. The constraint on the nodes in the theta direction is respected: 99 nodes are set on the IGV blade row, 195 on the rotor and on the stator blade rows. The boundary layer on the rotor blade, which is the most critical (the Reynolds number computed at the rotor hub results to be the highest) is represented by 65 layers. The first cell size is lower than one micron, reaching thus a Y+ ≤ 1. The expansion ratio is kept lower than 2 in both the spanwise and the blade-to-blade distributions. The rotor clearance is discretized on 33 layers.

The grid reaches a number of nodes approximately equal to 19.6 million cells.

The comparison between the RANS and the NLH results obtained are presented in Table 3.2. On the contrary to what expected for the NLH modeling, the comparison shows that the NLH simulation provides a better accuracy in the design condition and not in the near stall one.

Table 3.2.: RANS - NLH comparison.

Design	$\dot{m}_{rel.err.}[\%]$	$\pi_{rel.err}[\%]$	$\eta_{rel.err.}[\%]$
Exp. data	-	-	-
RANS	1.3582	0.6145	3.4840
NLH	1.3296	0.5984	3.5289
Near stall			
Exp. data	-	-	-
RANS	0.5837	-0.1879	-1.6760
NLH	2.8673	0.3054	-1.5748

Numerical parameters

Regarding the spatial discretization it is employed a second order central scheme, as it is the only one available for the NLH method.

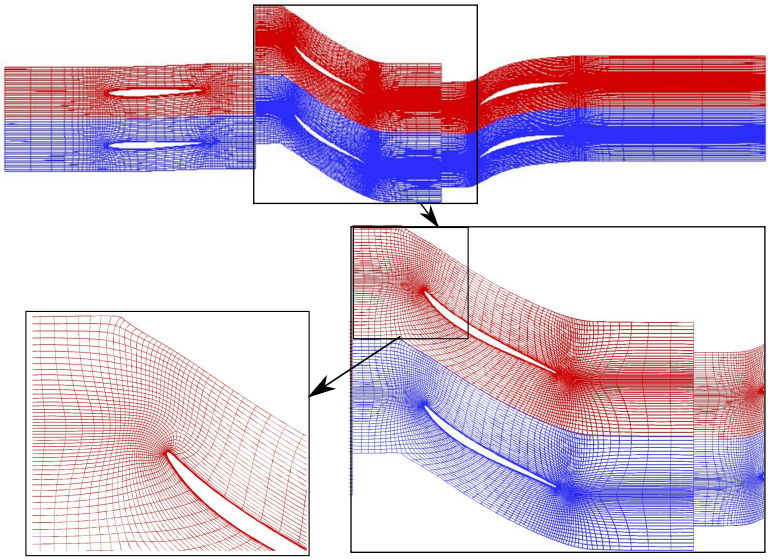


Figure 3.7.: Grid employed on the stage and zoom on the rotor blade row.

Time integration is performed with a four steps explicit Runge-Kutta method with a local time stepping.

The number of harmonics is selected as 3. The decision derives from a previous study on this configuration [93], showing that a higher number of harmonics lead to a significant increase in the computational time, without providing a better accuracy though.

Boundary conditions

The Spalart-Allmaras turbulence model is employed as the only one available for NLH computations.

The boundary conditions imposed in the computation are:

- the rotational speed, which at 100% Nn corresponds to 8750 rpm
- the inlet total pressure spanwise distribution retrieved experimentally in Plane 1
- the inlet total temperature spanwise distribution derived from the experimental results in Plane 1
- the inlet tangential velocity component $V_t/V_z = 0$
- the inlet radial velocity component $V_r/V_z = 0$
- the inlet turbulent viscosity spanwise distribution in the case of Spalart-Allmaras model, provided by the industrial partner

- the outlet static pressure derived from the experimental results in a given radial location and the radial equilibrium

The distributions imposed as boundary condition are shown in Figure 3.8.

Quality assessments of the simulation with respect to the experimental data - validation

The simulations target the definition of the performance of the various blade rows, therefore the total pressure measurements retrieved with the fast-response pressure probe at the rotor outlet are compared with the corresponding numerical data to have a further term of comparison.

In order to perform an appropriate comparison, the CFD data are extracted at the same axial and radial locations of the measurements. The result is shown in Figure 3.9 at both design and near stall conditions.

The CFD output appears to be comprised or not far from the test uncertainty. The relative error of the numerical data is always lower than 2% at all span locations. The probe blockage, together with the CFD modeling, influence the result.

The total pressure retrieved by the CFD is showing lower values along the whole span, at both design and near stall conditions. The result is consistent with the lower pressure ratio retrieved by the simulations. It is well known that numerical errors due to turbulence modeling, spatial discretization scheme and rotor/stator interface impact on the final result, implying a different representation of the unsteady flow structures. It has already been shown for this case [67] that NLH computations predict deeper and wider wakes than the one observed in the experiments. This results in a lower pitchwise average.

3.2.2.2. Spanwise distributions

The single blade rows are characterized with the radial distributions of total pressure and temperature, flow angle and entropy, which are presented in Figures 3.10, 3.11, 3.12, 3.13.

The ultimate effect of a compressor is to energize the flow by pressurizing it, therefore the total pressure distribution allows to assess the pressure ratio achieved by each row along the radius. The total pressure profile results from the work exchanged, which is due to the total temperature differences, and can also be expressed in terms of tangential velocity variations. Losses always affect the transformations across the blade rows, and can be quantified by the entropy production. The entropy profiles are computed with respect to pressure and temperature reference values and then adimensionalized with respect to the minimum value retrieved in the stage at its inlet.

The total pressure and the total temperature distributions are normalized with respect to the reference values indicated in section 2.1.1. The minimum inlet entropy value is employed for its normalization. Both the absolute and

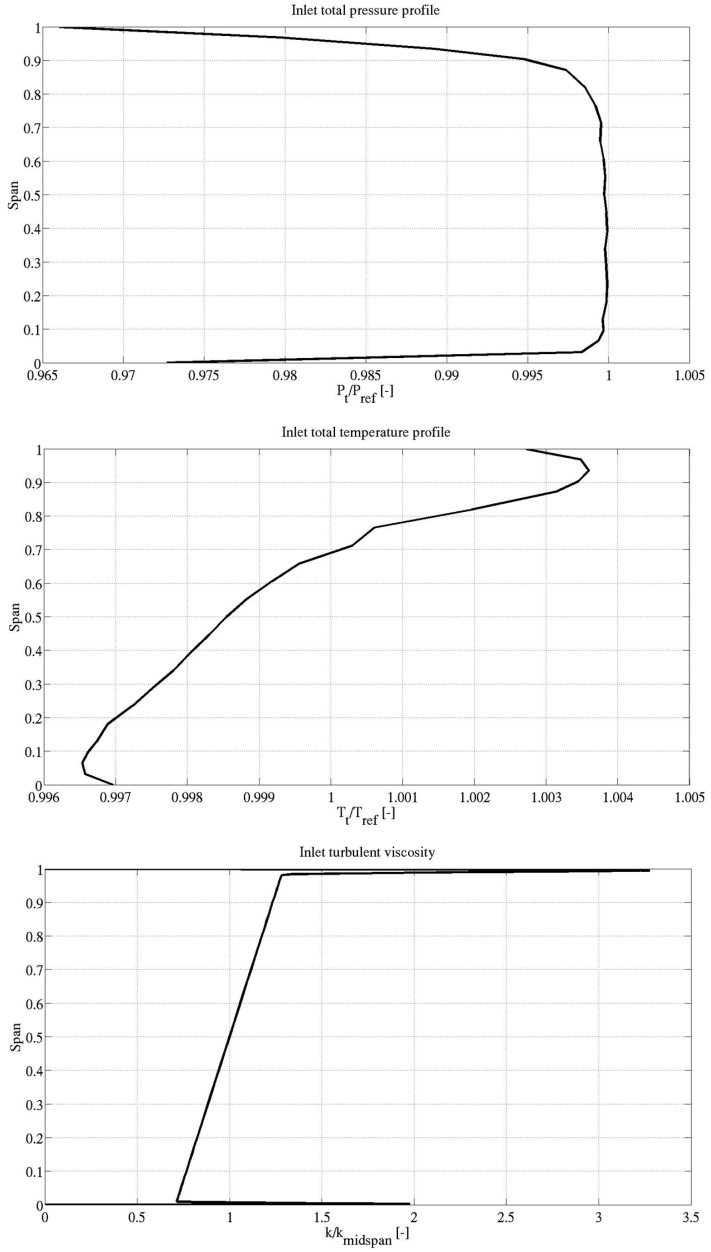


Figure 3.8.: Inlet distributions employed as boundary conditions in the simulations, respectively total pressure (a), total temperature (b) and turbulent viscosity(c).

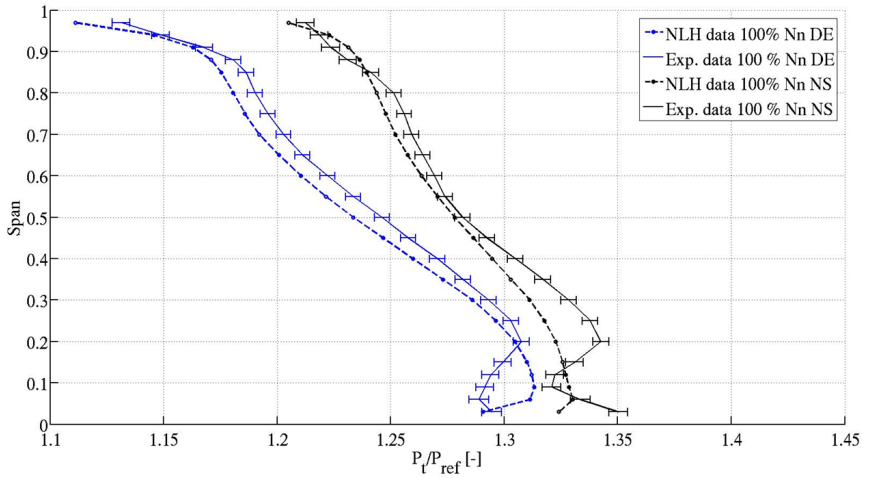


Figure 3.9.: Comparison of measured and the computed total pressure distribution at the rotor outlet at design and near stall conditions at 100% Nn.

the relative flow angles are plotted across the rotor, in order to have a better understanding on the velocity triangles distributions.

The total temperature not only provides the work distribution but also takes into account the static temperature increase, which is due to the losses. Work exchange occurs across a rotating blade row, and it is remarked by a total temperature rise, higher in the near stall condition than in the design one. In the present case it is visible between planes 2 and 3, which corresponds to the rotor location.

Higher total temperature values characterize the hub and the tip regions.

The former is due to the fact that the rotor is hub loaded, as pointed out by the total pressure distributions, on the other hand the losses are not concentrated at the hub, but in the tip zone. Higher entropy values are indeed located in this region and contribute to the total temperature increase by friction.

The angle distributions also show a hub loaded rotor, with a significant relative velocity variation.

The IGV remarks the presence of losses already at the stage inlet: higher entropy is visible in the tip region, thus the reason could be the elbow preceding the stage (see Figure 3.1).

The flow is reducing its speed across the stator and the presence of the boundary layer results in a higher entropy towards the walls.

The IGV has the function to represent the velocity distribution provided by the fan. This is obtained with a tangential velocity spanwise distribution and a small expansion.

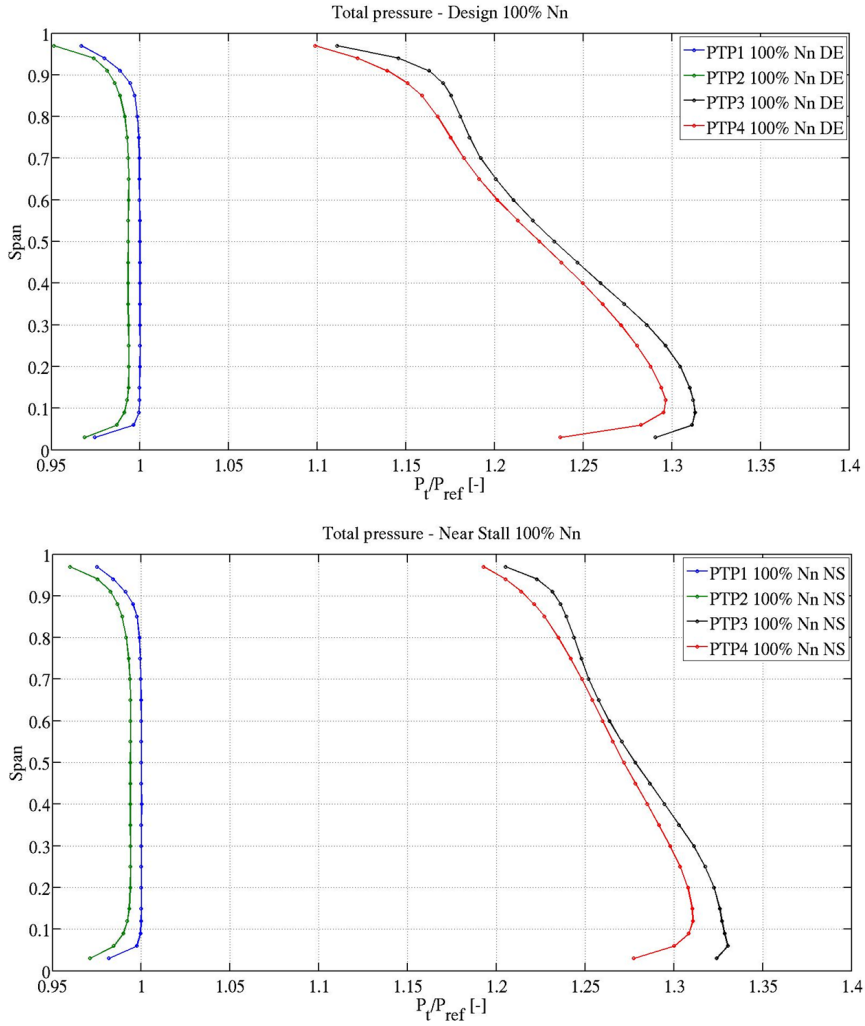


Figure 3.10.: Top: Total pressure radial distribution at 100% Nn design operating condition retrieved numerically in the four measuring plane. Bottom: Total pressure radial distribution at 100% Nn near stall operating condition retrieved numerically in the four measuring plane.

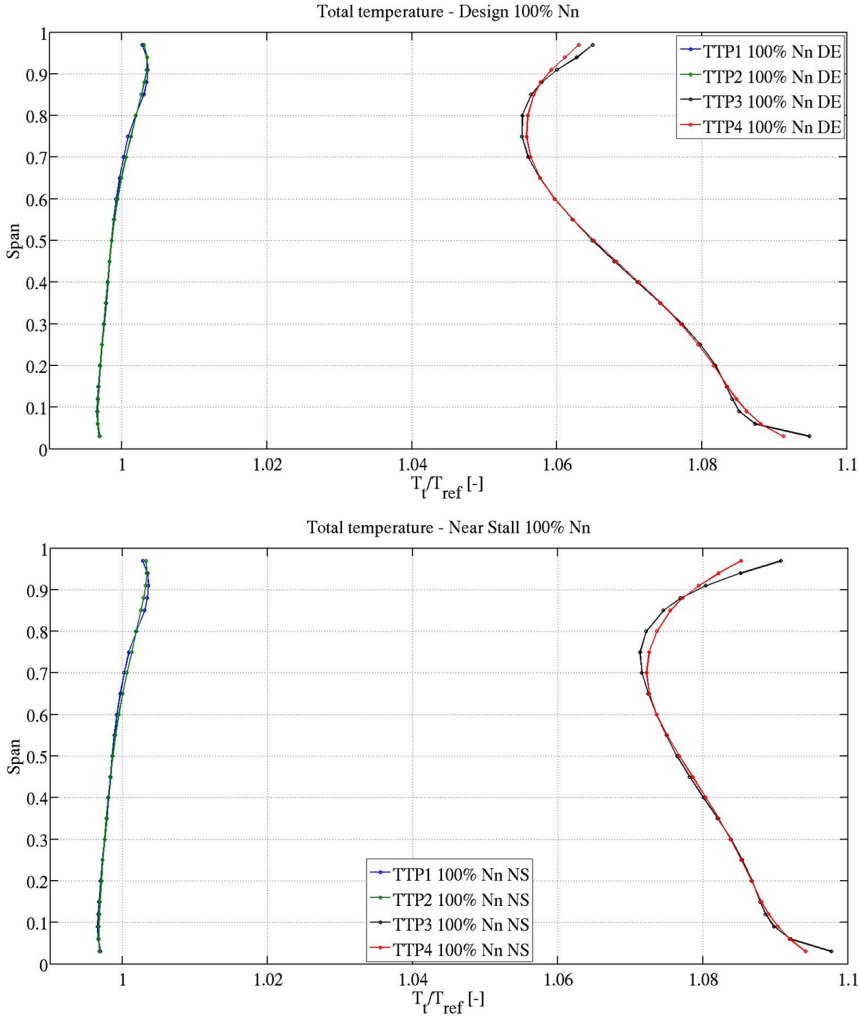


Figure 3.11.: Top: Total temperature radial distribution at 100% Nn design operating condition retrieved numerically in the four measuring plane. Bottom: Total temperature radial distribution at 100% Nn near stall operating condition retrieved numerically in the four measuring plane.

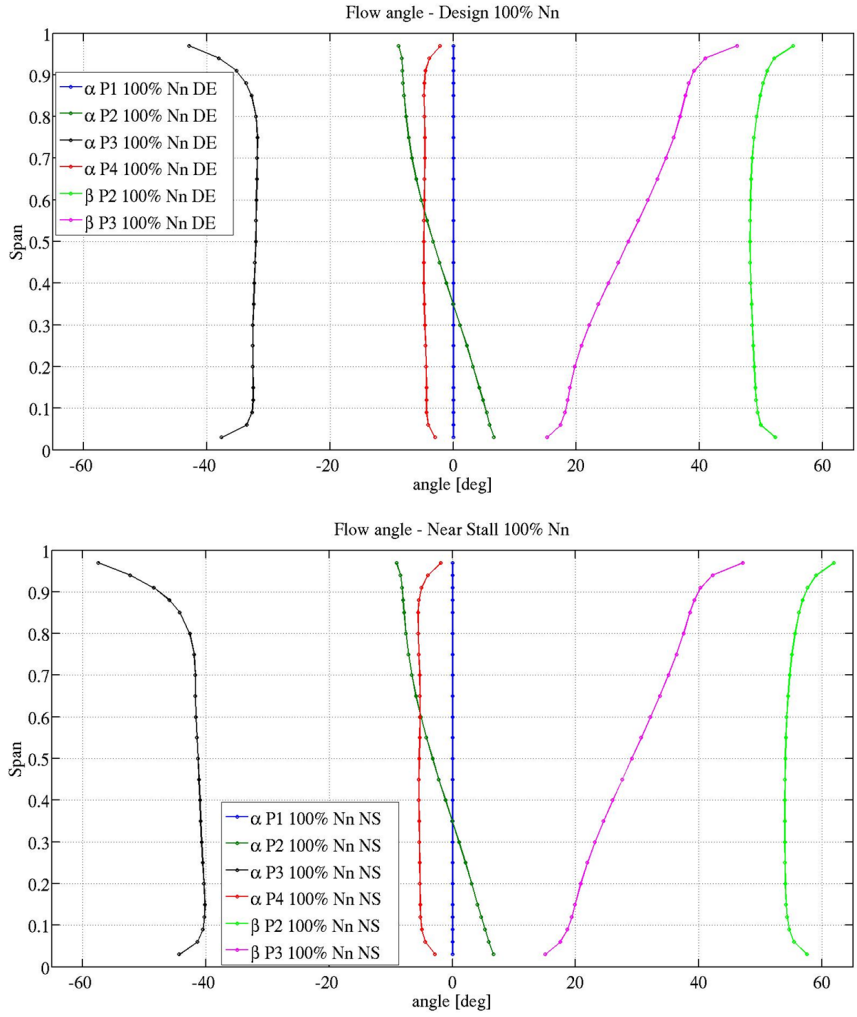


Figure 3.12.: Top: Flow angle radial distribution at 100% Nn design operating condition retrieved numerically in the four measuring plane. Bottom: Flow angle radial distribution at 100% Nn near stall operating condition retrieved numerically in the four measuring plane.

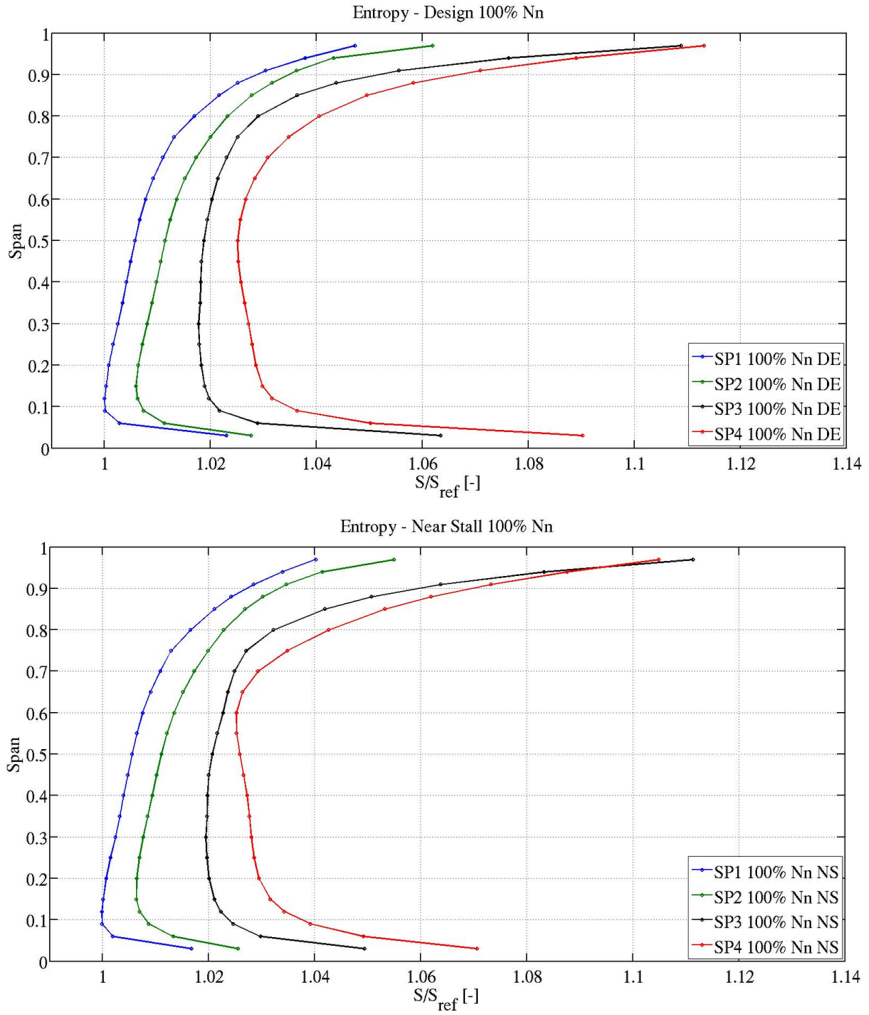


Figure 3.13.: Top: Entropy radial distribution at 100% Nn design operating condition retrieved numerically in the four measuring plane. Bottom: Entropy radial distribution at 100% Nn near stall operating condition retrieved numerically in the four measuring plane.

The rotor is delivering the highest part of the load, as the total pressure does not increase across the stator. On the other hand the only function of the stator is to provide an axial velocity distribution at the stage outlet.

3.2.2.3. T-s diagram

The temperature-entropy diagram finally represents a summary of the loading distribution across the stage. The work exchange is visible as a total temperature difference, while the losses on the abscissa in terms of entropy. Moreover it is possible to compute the degree of reaction of the stage.

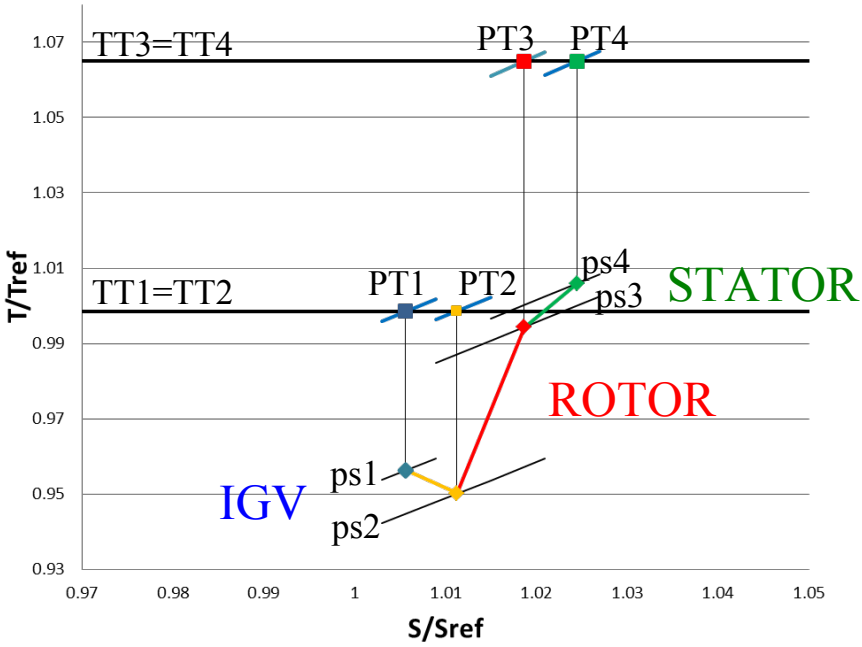


Figure 3.14.: T-s diagram retrieved numerically at midspan at 100% rpm, design operating condition.

The graph has been obtained with the total temperature, pressure and static pressure retrieved numerically at midspan, in the four measuring planes.

The diagram is complementary to the spanwise distributions as it allows to distinguish the static pressure from the kinetic component in the total pressure increase across the stage.

In this case the rotor delivers the highest part of the compression, and it

can be quantified by the degree of reaction:

$$\chi = \frac{\Delta Ps_{rotor}}{\Delta Ps_{stage}} \tag{3.5}$$

which represents the static pressure rise produced by the rotor ΔPs_{rotor} with respect to the one of the stage ΔPs_{stage}. It is equal to 0.93.

3.3. Detailed characterization of the flow field

3.3.1. Rotor flow field description

3.3.1.1. Total pressure distribution at the rotor outlet

The rotor outlet flow field is detected with a radial traverse of the fast response pressure probe, as described in section 3.1.

The time-resolved pressure data are exploited to characterize the typical blade passage by applying a phase locked average (PLA). As this post-processing methodology is applied in both the stable and the unstable operating points, the uncertainty on the rotor outlet total pressure PLA is presented as an example in Appendix **??**, to assess the quality of this technique.

Each of the 23 acquisitions detected along the radial traverse are divided into rotor revolutions according to the trigger (one-per-rev) signal and then into the number of rotor blades. The choice of the number of classes per blade passage is comprised between 85 and 90, according to the minimum number of points per blade passage retrieved in the acquisitions in the same radial traverse. The phase locked average procedure is thoroughly explained in Appendix B.1. The grid obtained, which is composed by 90×23 points, is interpolated on a more refined matrix (90×390) in the circumferential and radial direction.

The corresponding RMS is then calculated, in order to define the unsteady zones of the blade passage, where also the losses are located. The equation employed is:

$$RMS = \sqrt{\frac{\sum_{i=1}^{N}(P_i - \overline{P})^2}{N}} \tag{3.6}$$

in which P_i denotes the single acquisition, $\overline{P}$ the mean level in the class and N the number of points used to obtain one PLA value (i.e. the number of blade passages times the number of revolutions).

The skewness and the kurtosis for the PLA are also computed. Skewness, shown in eq.(3.7), is a measure of the lack of symmetry for a given data set, hence any symmetric distribution such as a Gaussian (or normal) distribution has zero skewness. While negative values of skewness indicate that the data is skewed towards the lower values (i.e. has a longer tail on the lower

side of the center point), positive values indicate vice versa. The notation employed in equation 3.7 corresponds to the one of the RMS, σ denotes the variance of the same distribution.

$$skewness = \frac{\sum_{i=1}^{N}(P_i - \overline{P})^3}{N\sigma^3} \tag{3.7}$$

The skewness is able to provide the positive or negative distance of the data set from the mean value. In time-resolved pressure measurement it is utilized to recognize the presence of shear stresses (some examples are shown in literature, e.g. Zambonini et al. [51]), as positive values correspond to an acceleration of the flow field, whereas negative values to a deceleration.

Kurtosis, on the other hand, is a measure of peakedness of data relative to a Gaussian distribution (which has a kurtosis value of 3). Data sets with low kurtosis tend to have a flat top, while data sets with high kurtosis have a sharp peak near their mean value and heavy tails. As the normal distribution has a kurtosis value of 3, an adjusted definition called *excess kurtosis* given in eq. (3.8), where 3 is subtracted from the typical kurtosis definition (also called Pearson's kurtosis), is used in order to achieve positive values for *peaked* and negative values for *flat* data sets. The notation employed in equation (3.8) corresponds to the one of RMS and skewness.

$$kurtosis = \frac{\sum_{i=1}^{N}(P_i - \overline{P})^4}{N\sigma^4} - 3 \tag{3.8}$$

High values of kurtosis correspond to a distribution having heavy tails, thus it is also typically employed in time-resolved pressure measurements (e.g. Zambonini et al. [51]), as it quantifies the intermittency of the flow field.

The combined analysis of the phase locked average, RMS, skewness and kurtosis allows the description of the flow field and to distinguish the unsteady flow structures appearing in the blade passage. These maps are presented in Figures 3.15, 3.16, 3.17, 3.18.

The total pressure map highlights what has been observed in the spanwise distributions: the losses are concentrated in the tip region, while the hub is delivering the highest part of the pressure ratio. The closing of the throttling valve causes a loading increase in the spanwise direction.

The wake appears in the pressure distribution as a low pressure and unsteady zone, as the RMS is higher in this region. The skewness shows an acceleration on the pressure side due to the mixing of the flow with the suction side flow, and a corresponding deceleration on the suction side.

It is noteworthy to notice a thickening of the wake towards the hub, due to the presence of the hub corner separation, which appears as a consequence of the adverse pressure gradient and the mixing of the suction side and the

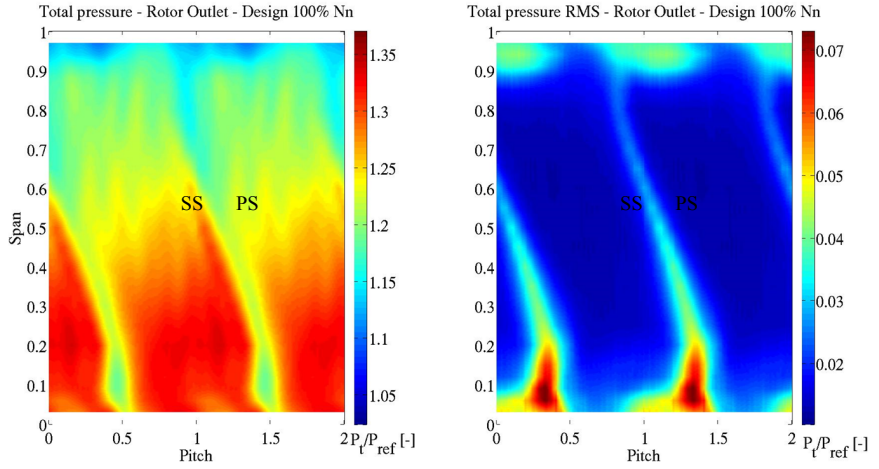


Figure 3.15.: Total pressure phase locked average (PLA) map and corresponding RMS of the rotor outlet flow field at 100% Nn, design operating condition.

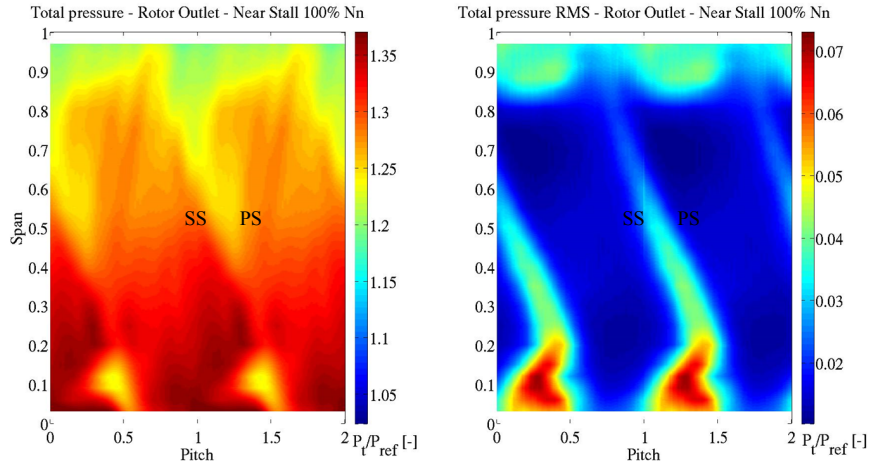


Figure 3.16.: Total pressure phase locked average (PLA) map and corresponding RMS of the rotor outlet flow field at 100% Nn, near stall operating condition.

endwall boundary layers. It represents the highest source of unsteadiness in the blade passage. The kurtosis shows in fact that the intermittent area is widely spread across the blade passage.

As previously shown in Chapter 1.3.2, the literature provides several examples of the growth of the hub corner separation with the loading, until

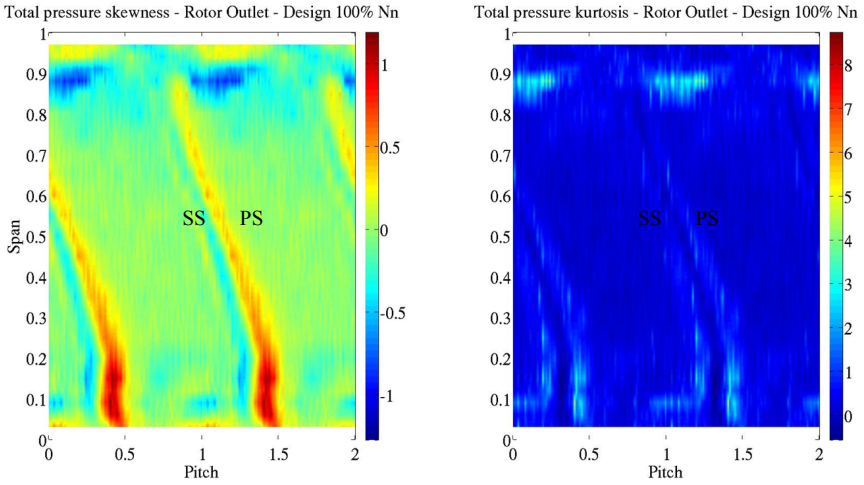


Figure 3.17.: Total pressure skewness map and kurtosis of the rotor outlet flow field at 100% Nn, design operating condition.

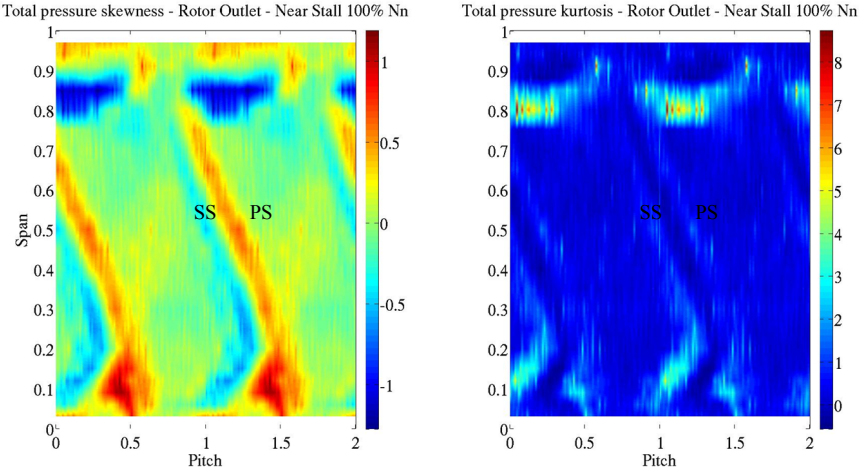


Figure 3.18.: Total pressure skewness map and kurtosis of the rotor outlet flow field at 100% Nn, near stall operating condition.

reaching the hub corner stall. In the present case it shows a size increase from the design to the near stall condition, occupying more than 50% of the pitch and 20% of the span at the higher loading.

The tip region is characterized by a wide unsteady zone. The tip leakage flow is highlighted in this area and, as it will be explained in the next paragraph, does not occupy the whole blade passage (see Figures 3.22, 3.23).

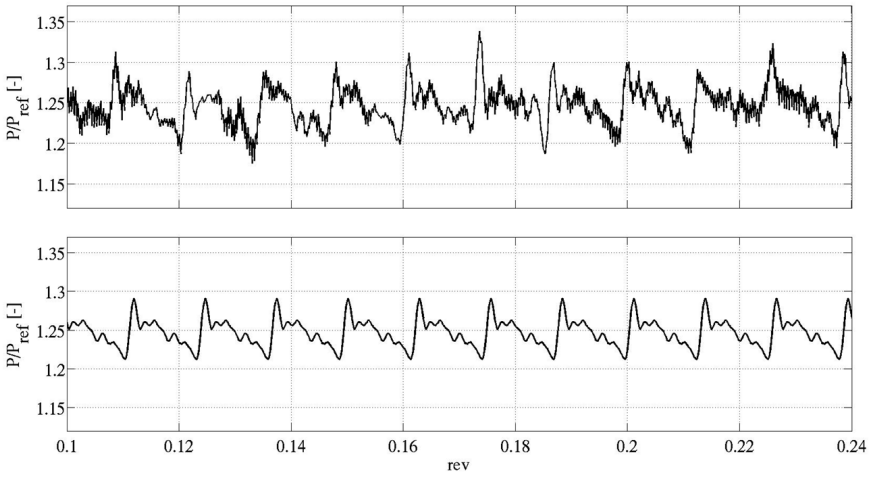


Figure 3.19.: Rotor outlet total pressure at midspan, comparison between the raw signal (top) and phase locked average (bottom).

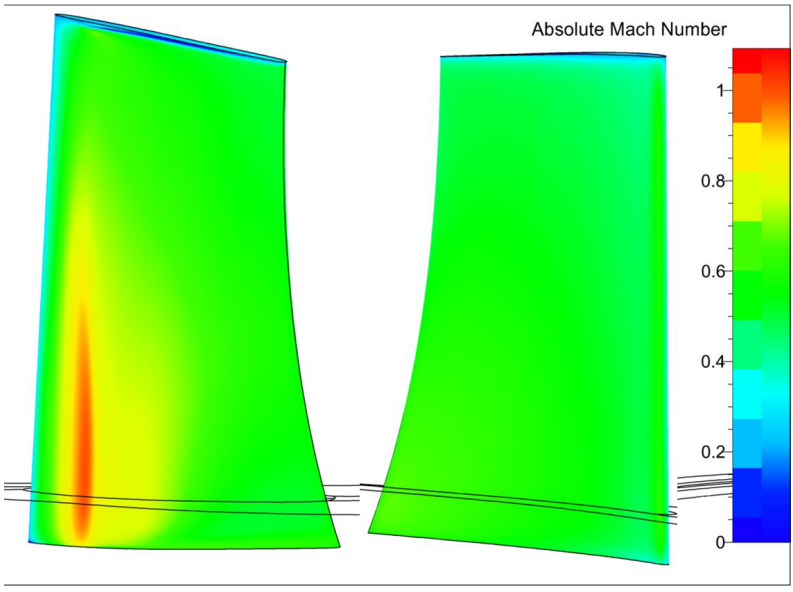


Figure 3.20.: Absolute Mach number distribution retrieved numerically on the rotor blade on the suction side (left) and on the pressure side (right).

The rotor outlet map allows to define the extension of the separation zone, which covers approximately 10% of the span in the design condition and increases to approximately 15% in the near stall one.

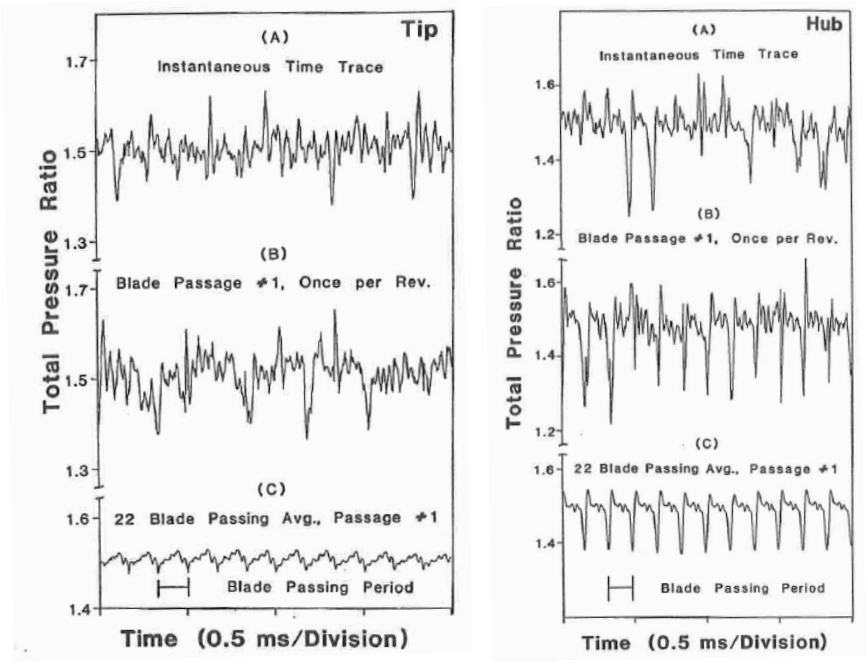


Figure 3.21.: Left: NASA rotor exit pressure ratio near tip (R/Rt = 0.91) for rotor as whole(A), an individual blade passage (B), and ensemble average of that individual blade passage [28]. Right: Same as Left, but for rotor hub (R/Rt = 0.68) [28].

This behavior has already been shown in the literature: the adverse pressure gradient across the blade row and the pitchwise pressure difference increase from the design to the near stall condition and therefore impact on the size of the tip leakage flow.

The skewness defines the sense of rotation: higher values are visible in the area closer to the casing while lower values appear below, thus the vortex shows an anti-clockwise rotation. The deceleration zone increases from design to near stall condition and its intermittent behavior is confirmed by the kurtosis.

Pressure fluctuations are visible in the blade passage at all the span heights in the PLA. The raw signal at 50% of the span is presented as an example, together with the corresponding phase locked average in Figure 3.19. The sound flow oscillates at approximately 3-4 times the blade passing frequency.

Ng et al. [28] and Epstein et al. [94] retrieved similar patterns in transonic compressors (see Figure 3.21), which has been found to be due to the shock fluctuation around its mean location.

The analysis carried on by these authors concerns transonic fan blades,

which are characterized by normal shocks in the blade passage. They proposed a model to characterize the fluctuations observed, which can be extended to shocks of any kind. The shock movement appear to be due to inlet Mach number fluctuations, together with the trailing edge vortex shedding, which depends on the blade suction side separation length.

This model could fit in the present case as in the rotor blade passage a weak shock appears, due to the supersonic pocket on the blade suction side (see Figure 3.20). The inlet Mach number fluctuations indeed may be attributed to the presence of the IGV blade row, whereas the suction side separation length is likely to vary for the intermittent behavior of the hub corner separation, which in the Dream compressor stage appears to be significantly extended across the blade passage. This separation is therefore plausible to interact with the shock, giving rise to the fluctuations visible in Figure 3.19.

3.3.1.2. Casing pressure distribution

The time-resolved pressure measurements retrieved with the sensors shown in Chapter 2.4.2 allow the description of the rotor tip flow.

The signals are low pass filtered at 40 kHz in order to elude not only the effect of the resonance of the sensors, but also the one of the cavity resonance of the inserts, visible in Figure 2.18. The former would result in additional noise, the latter would provide a signal alteration.

The rotor casing static pressure is also represented with the phase locked averaging technique (and RMS) utilized for the rotor outlet total pressure. In this case though the matrix of data presents a much higher refinement in the circumferential than in the axial direction. Indeed 90 classes are employed for the azimuthal coordinate, while only 14 axial positions (corresponding to the sensor locations) are available. An interpolation along these coordinates results in a plot where it is difficult to distinguish the various flow structures.

The problem is overcome by an interpolation grid which varies the interpolation direction according to the blade zone. The domain of a blade passage is divided according to the main direction of the flow field. The region preceding the leading edge and the one beyond the trailing edge are considered not to differ significantly from the axial direction, therefore the signals are interpolated on the axial and circumferential directions. On the other hand the flow field in the blade passage is subjected to the presence of the blade and the tip leakage vortex, therefore the directions considered in the interpolation are those of the blade stagger angle and the one of the tip leakage vortex. The latter has been defined by J. Sans according to previous CFD calculations on the stage presented in [95]. The mesh obtained is characterized by a matrix of 90×390 points.

As explained in the previous paragraph, the PLA is able to detect the mean component of the flow field in a blade passage and the correspond-

ing RMS allows to identify the unsteady zones. The phase locked average technique is inherently characterized by a lower uncertainty than instantaneous measurements, as the number of points averaged allows to reduce it. However, given the low amount of points in the axial direction, the detailed topology retrieved with the proposed interpolation grid has to be further verified.

The contour plot of the instantaneous casing static pressure is therefore analyzed with two objectives: first to verify the presence and the topology of the flow structures retrieved with the phase locked average, second to have a better understanding of the discrepancies existing between the various blade passages.

In order to obtain the contour plot the angular space shift existing between the sensors has to be taken into account.

The sensors in fact cover the rotor casing in the axial direction from its inlet to its outlet, but are also shifted in the circumferential direction covering 42°, thus the signals have to be rephased.

The angular space shift $\Delta\theta$, corresponds to a time lag ΔT when considering a particular phenomenon rotating at an angular speed Ω. The time lag, which has to be compensated, can be expressed as:

$$\Delta T = \frac{\Delta\theta}{\Omega} \tag{3.9}$$

In the stable operating points the preponderant phenomena occurring are purely linked to the blade passing frequency. The reference signal considered is the one located at the rotor leading edge (K3), at 38° (see Figure 2.17).

In case more phenomena appear (e.g. a stall cell, which is characterized by a much lower frequency than the BPF), the related time lags must be taken into account. In order to apply the shift, the spectrum is divided in to a number of intervals equal to the one of the phenomena to be considered. Each part of the spectrum is isolated by filtering the other parts. For example if there are two rotating phenomena the spectrum is divided in two intervals: a low frequency band dominated by the low frequency phenomenon (e.g. the cell frequency), and a high frequency one dominated by the high frequency phenomenon (e.g. the BPF). All the signals are at first low pass filtered in the low frequency band and shifted with respect to the related time lag (e.g. the one of the stall cell), then high pass filtered in the high frequency band and shifted with respect to the high frequency time lag (e.g. the one of the BPF).

Each time-resolved signal is then reconstructed with the mean value, and the two shifted ones. This representation of the flow field is not exact as it considers only the deterministic components related to the two main phenomena (e.g. the stall cell and the BPF), while all the other components are not included.

This methodology has been applied by Courtiade [62], who reconstructed the casing flow field of a three stage axial compressor in stable conditions

and during the formation of spikes and surge.

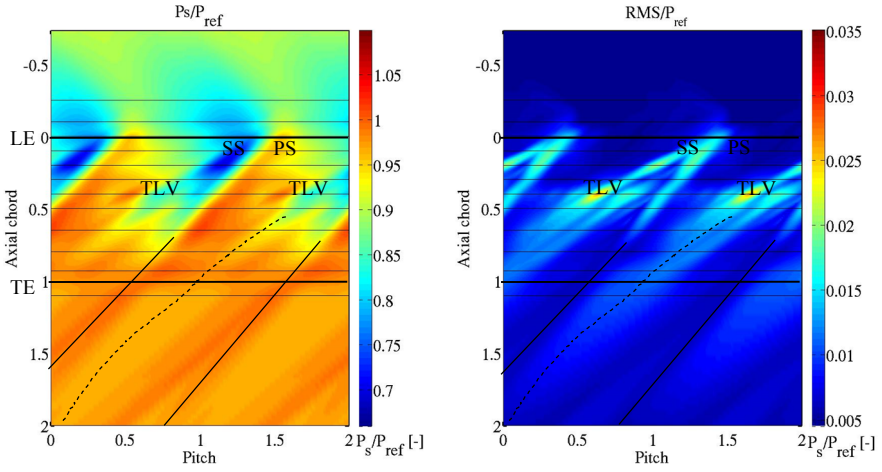


Figure 3.22.: Phase locked averaged casing static pressure distribution and corresponding RMS at 100% Nn, design operating condition. The grid indicates the axial location of the sensors.

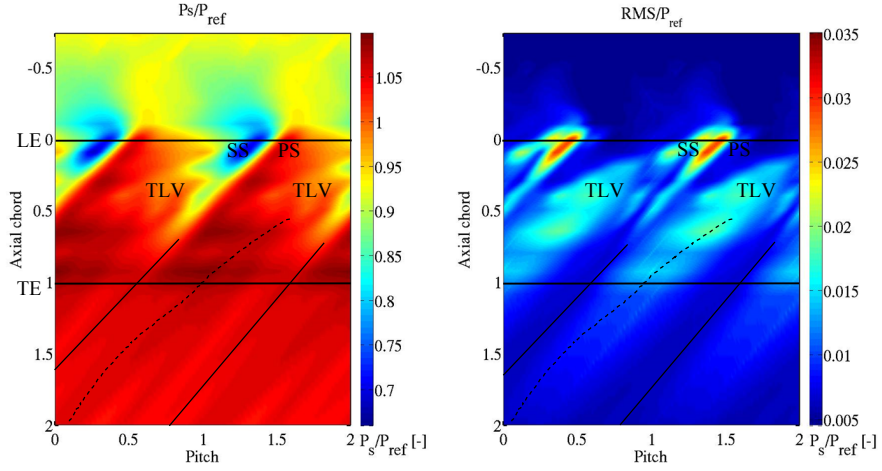


Figure 3.23.: Phase locked averaged casing static pressure distribution and corresponding RMS at 100% Nn, near stall operating condition.

The rephased signals are then divided in to an equal number of points, in order to avoid discrepancies on the different data sets.

The phase locked average is presented together with the corresponding RMS in Figures 3.22, 3.23, whereas the contour plot in Figures 3.24, 3.25.

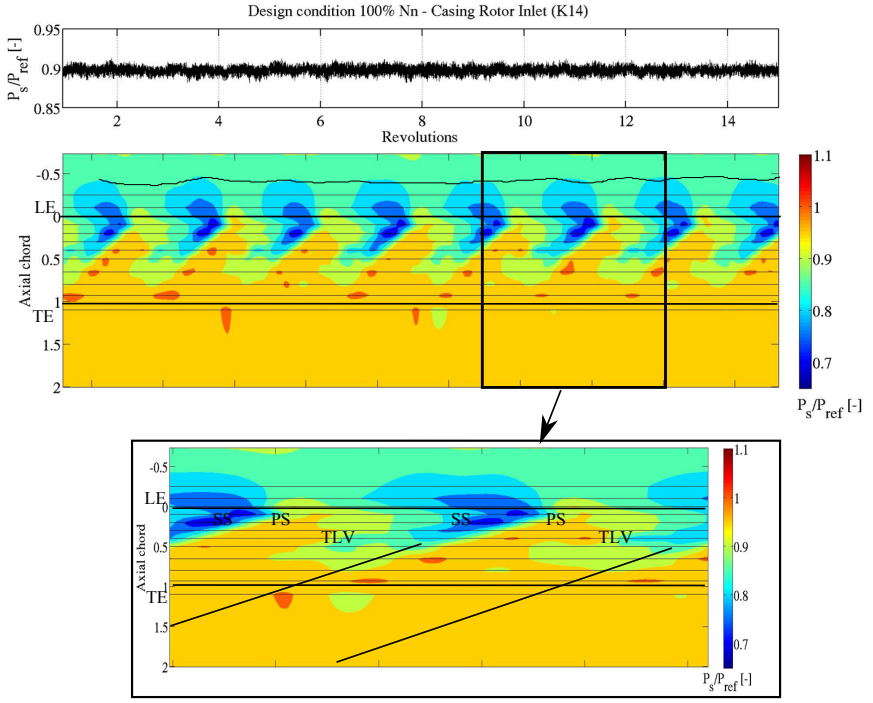


Figure 3.24.: Top: Time resolved static pressure signal at the rotor inlet at 100% Nn, design operating condition. Bottom: Instantaneous static pressure distribution on the rotor casing at 100% Nn, design operating condition, and corressponding zoom on two blade passages. The grid indicates the axial location of the sensors.

Both of them are shown for the design and near stall conditions at 100% Nn.

The tip leakage flow (TLF) is visible in the PLA map and in the carpet plot as a low pressure region starting from the leading edge, allowing to define the blade positioning. In the graphs are highlighted the blade pressure and suction sides (respectively PS, SS), and the wake trajectory with a black line. The trajectory of the TLF is marked on the phase locked average with a dashed line.

The TLF is also identified with high RMS values, which allow to track its trajectory across the blade passage. The RMS spots have been also retrieved by Hah et al. [29] in a one and a half stage compressor and they have been attributed to the IGV wakes interactions with the tip leakage flow. The graph obtained by Hah is reported in Figure 3.26 for sake of completeness.

The pressure gradients across the blade passage are responsible for the magnitude and the trajectory of the tip leakage flow. In this case the tip

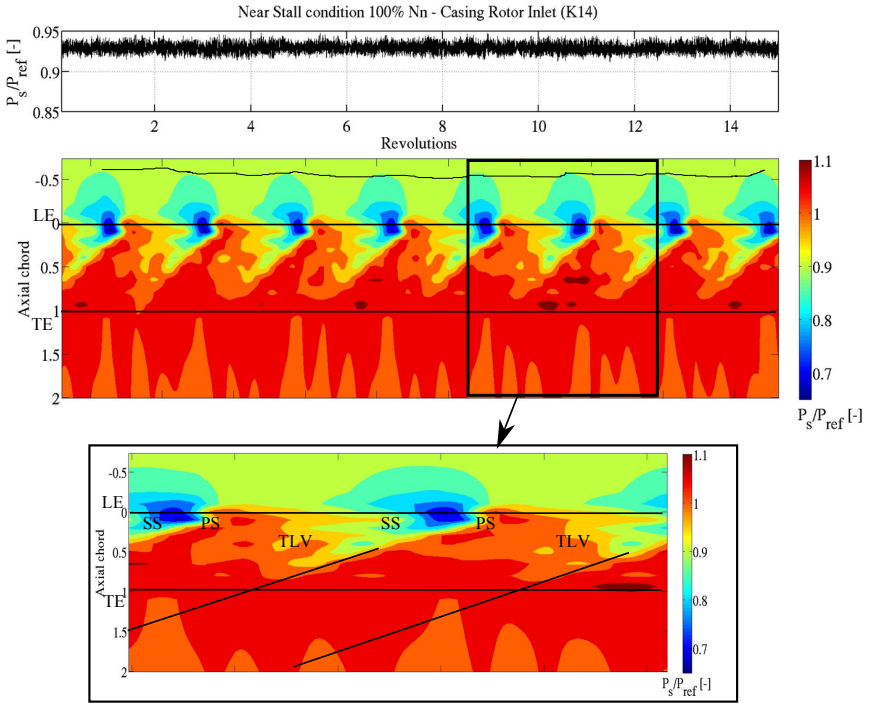


Figure 3.25.: Top: Time resolved static pressure signal at the rotor inlet at 100% Nn, near stall operating condition. Bottom: Instantaneous static pressure distribution on the rotor casing at 100% Nn, near stall operating condition, and corressponding zoom on two blade passages.

vortex is confined within the blade passage, also at high loading, where it impacts on the adjacent blade. The radial loading is concentrated towards the hub, resulting in the tip region in this trajectory of the tip leakage flow. This behavior is retrieved in both the phase averaged results and in the contour plot.

The location of the tip leakage flow visualized in the casing phase locked averages (Figures 3.22, 3.23) corresponds to the structure observed in the rotor outlet maps (Figures 3.15, 3.16): in both the graphs the clearance flow impact at the rotor outlet (axial position 2 in Figures 3.22, 3.23) with the wake of the adjacent blade, in the two plots they are respectively marked with a dashed and a continuous black line.

Rotating instabilities

The low pressure region observed upstream of the rotor leading edge, visible in both the PLA and the carpet plots seem to be due to the rotating instabilities mechanism. It is visible at both design and near stall conditions.

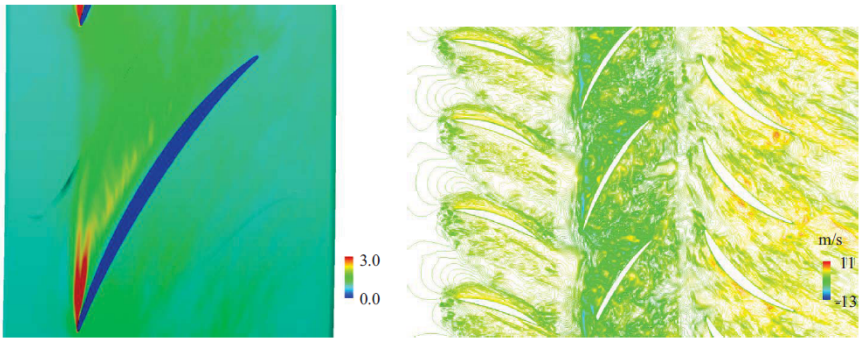


Figure 3.26.: Standard deviation of static pressure and instantaneous axial velocity contours at rotor tip, at near stall condition in a one and half stage [29].

The spectra of the signals retrieved with the sensors on the casing seem to confirm their presence. The spectra are presented in Figure 3.27 for the inserts located at −75% (K14), 0% (K3), 110% (K12) and 200% (K15) of the rotor axial chord, to show the frequency content evolution along the blade passage.

As already explained in the literature survey, the rotating instabilities are recognized in a spectrum with the presence of several peaks comprised between 1/3 and 2 BPF. Each peak corresponds to a mode of the circumferential fluctuation.

In the present case several modes are distinguished within 10 and 60% of the BPF and also at $BPF + modefrequency$. The highest amplitude is reached for the sensor at the leading edge (K3), which is the location where the low pressure region appears. The peaks are also visible at −75% of the axial chord, while they disappear towards the outlet. This behavior has been retrieved by several authors: Pardowitz et al. [12], Kamaier and Neise [54], and Wang et al. [56].

It is noteworthy to observe that one of the peaks attributed to the rotating instabilities appears also when the stage is subjected to rotating stall. Figure 3.27, c indeed shows the spectra retrieved in the stall condition, in which the component at approximately 6 kHz remains also in the unstable conditions. The peak is evident at the rotor inlet as a fraction of the BPF, and it is summed to the BPF in the signals at the rotor outlet. The peak presents a wise amplitude (approximately 1 kHz) and it seems comparable to the observations of Pardowitz et al. [12] reported in the Literature Survey. Further explanations regarding the presence of rotating instabilities during the stall transient will be provided in Chapter 4.4.2.

In the contour plots (Figures 3.24 and 3.25) the extension of the low

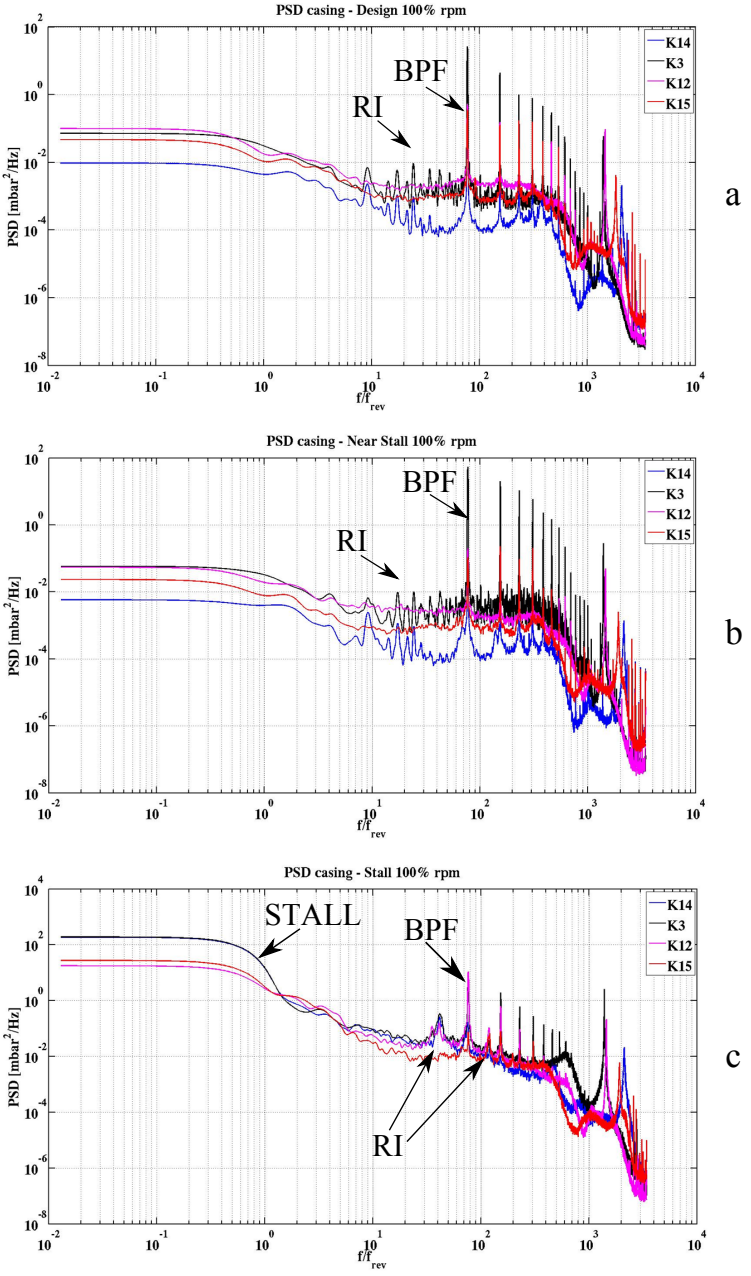


Figure 3.27.: Spectra of different sensors on the rotor casing at design (a), near stall (b) and stall (c) operating conditions.

pressure region slightly varies between the different blade passages. The mechanism may be associated the one known for the rotating instabilities presented in Figure 1.14: the tip flow of a blade passage influences the one of the preceding and the following, giving rise to a fluctuation which propagates circumferentially. This is remarked by the black line ahead of the rotor blades in the carpet plots and by an RMS peak at the rotor leading edge.

The rotating instabilities are due to the fluctuating tip flow on the blade suction side, however the flow structure which is responsible for their presence still has to be completely identified and seems to vary from a machine to the other. In the literature some examples are shown: Wu et al. [96], [97] explain their formation on a tip loaded rotor as the tip leakage vortex breakdown, whereas Pardowitz et al. [13] retrieve them in a shrouded rotor.

In the Dream compressor stage the presence of the rotating instabilities seem to be due to the low pressure region forming upstream the rotor leading edge as a potential effect of the tip leakage vortex. Measurements on the rotor blade would enable to provide an accurate explanation on the case examined.

3.3.2. Stator flow field description

The detection of the flow structures which participate to the triggering of rotating stall is the objective of this chapter. Considered the high degree of reaction of the stage, the stator is expected to provide little contribution in the unstable mechanisms. This will be further characterized in this paragraph by the detailed description of the flow field at design condition, employing the total pressure measurement matrix presented in section 3.1, which covers three stator pitches.

The average in time of the total pressure data detected at the stator outlet yields equivalent results to those of a pneumatic pressure probe, allowing the description of a fixed blade row. The use of a fast response pressure probe provides in addition the RMS, and therefore it enables to identify the unsteady regions, as previously shown for the rotor flow field. The RMS is computed as the scatter of the time-resolved signal around its mean value, at each measurement position, using the formula presented in the previous paragraph (Eq. B.1). The averaged total pressure and the corresponding RMS maps are presented in Figure 3.28.

For a complete description of the flow field its time evolution is also presented. At each measurement position the total pressure signal is ensemble averaged on the rotor revolution frequency by utilizing the one-per-rev signal. This allows to detect a mean evolution of the stator flow field on a rotor revolution. An RMS on the ensemble average is also computed with the formula B.1 in order to locate the unsteady regions. The results corresponding to three time frames are presented in Figure 3.29

The stator has the aim of providing an axial flow at the stage outlet. Like

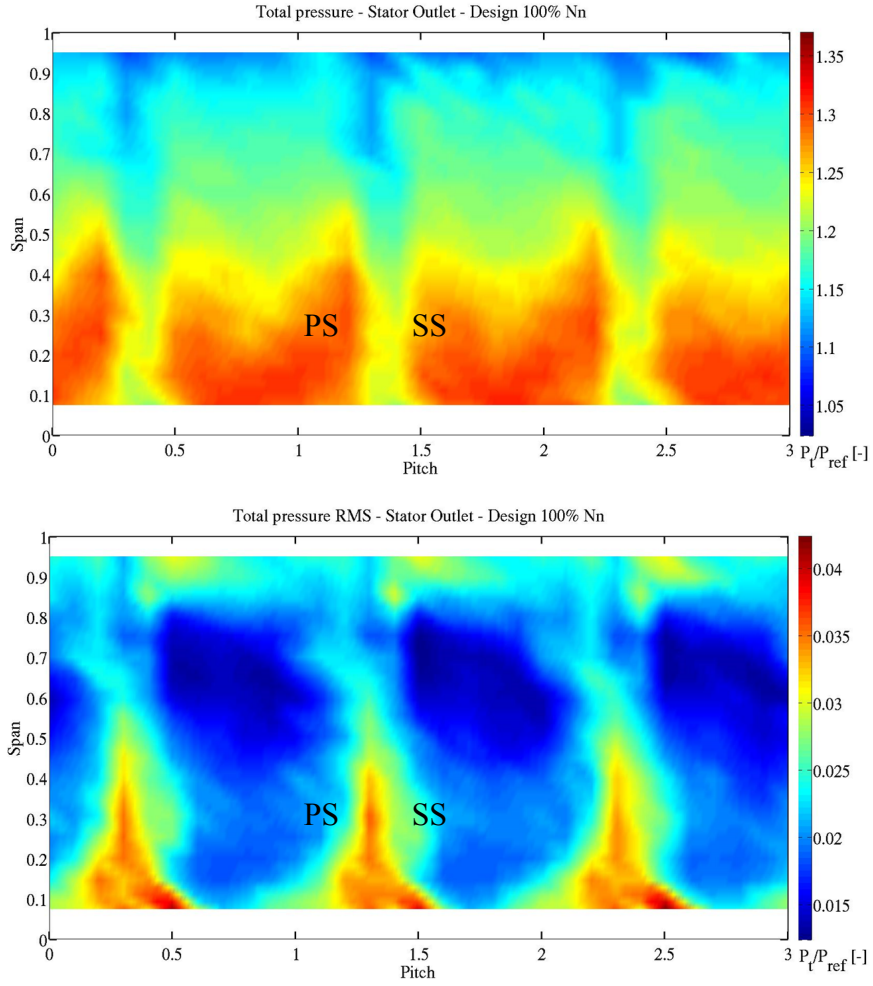


Figure 3.28.: Stator outlet total pressure (time averaged) and corresponding RMS.

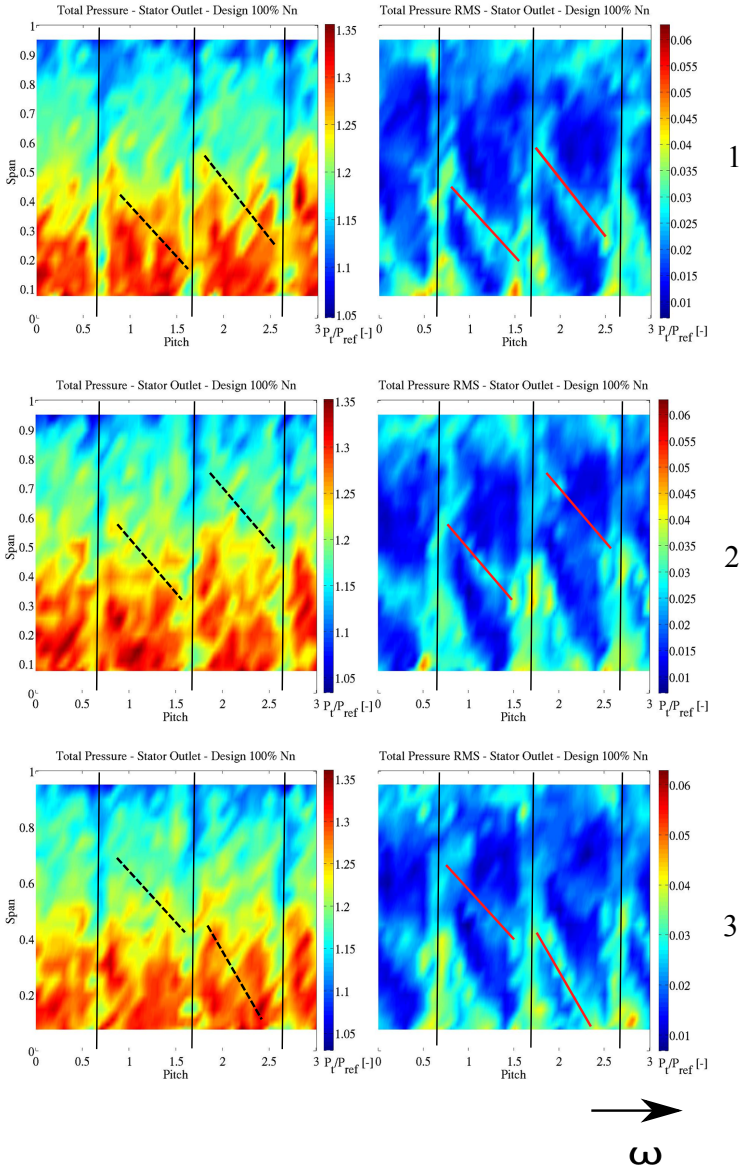


Figure 3.29.: Instantaneous values of stator outlet total pressure and corresponding RMS for three subsequent times.

the rotor blade row, the stator is also hub loaded (see Figure 3.10). Both in the averaged and the instantaneous distributions the stator wakes can be distinguished as low pressure regions in the pressure maps, and as zones of high RMS. Higher RMS values are visible at both the hub and the tip regions, which correspond to the higher losses remarked in the pitchwise average presented in Figure 3.13.

The instantaneous pressure maps and RMS (Figure 3.29) indicate that the greatest part of the unsteady flow structures responsible for the losses are influenced by the rotor. The rotor wakes in fact are visible in the RMS (red lines) and it is possible to distinguish their time evolution. The interaction between the rotor and the stator wakes appears as a peak of RMS, and as lower pressure in the pressure distribution. It is especially clear in the wake in Figure 3.29, 2.

The pressure distribution appears to vary in the three instants of time. The rotor hub corner vortex and tip leakage vortex are also visible at the stator outlet as higher RMS zones. On the other hand, the only remarkable unsteady flow structure that can be attributed to the stator blade row is the wake, the potential migrations of other secondary flows are submerged by the structures of the rotor blade row.

Given these considerations on the instantaneous pressure maps, it is possible to attribute the low pressure region visible at midpitch in the averaged pressure map (Figure 3.28) to the rotor wake. In fact its extension varies in the three blade passages.

The data-set employed for the description of the stator flow field provides both the space and time information regarding this blade row, and could be utilized in addition to a similar data-set retrieved at the rotor outlet to fully describe the rotor/stator interactions by performing a modal analysis. Examples of analysis of this kind are presented in literature: Courtiade et al. [98] apply this method on a three-stage compressor, starting from the modal decomposition proposed by Tyler and Sofrin [89]. The drawback of the VKI-R4 test-section is that the stage periodicity is on a quarter of annulus, which correspond to 25 IGV/stator and 19 rotor blades, while the fixed rows movement is possible only on four pitches. Therefore the application of a modal analysis would be possible, but requiring the assumption of periodic flow at the extremes of the four pitches, making it not ideal. Therefore in case a complete study on the blade rows interaction has to be undertaken, the machine periodicity is preferred to fit with the investigated area.

3.4. Conclusions

The characterization of the stage in the stable range points out a high degree of reaction, which is due to: an IGV blade row, having the role to simulate the fan velocity profile impinging on the first stage of the booster, a highly loaded rotor blade row and a stator blade row delivering an axial flow at

the stage outlet. The high degree of reaction of the stage seem to cause the presence of a supersonic pocket in the rotor blade passage. It also suggests a first stalling of the rotor blade row.

The rotor is characterized by a loading distribution concentrated at the hub. Considering the two stalling mechanisms appearing in a blade, due to either the tip leakage flow or the hub corner separation, the stage shows higher probability of a hub corner stall. Given the loading distribution, the tip leakage flows do not occupy the whole blade passage in the near stall condition, whereas the hub corner separation creates blockage over a wider part of the blade passage.

On the other hand the tip region represents the highest source of losses, which appear to be due to the inlet bending of the test section and the clearance flow.

The Dream compressor stage also seem to be affected by the presence of the rotating instabilities mechanism in stable conditions. It is attributed to the potential effect of the rotor tip leakage flow.

The stator blade row is also hub loaded, and it is shown to provide a minor contribution to the stage loading, being mostly influenced by the rotor flow field. The measurements performed at the stator outlet suggest a small machine periodicity for the investigation of the rotor/stator interactions.

Chapter 4.

Characterization of the unstable operating range

In the previous chapter the stable behavior of the Dream compressor has been presented. The flow structures characterizing the stage and their evolution at different operating conditions have also been highlighted.

The investigation of the unstable regime is the objective of this chapter. The analysis is comprehensive of both the stall inception and the post-stall behavior.

A compressor, during its operation, is always subjected to speed variations, thus the unstable regime is tested at different rotational speeds.

The specific experimental set-up employed is introduced at first and it is followed by an overview on the unstable regime: the stability limit is defined on the experimental characteristic for different speed lines, and the corresponding time-resolved pressure signals are presented.

The signals retrieved at three span heights are employed to understand the nature of the stall inception. The latter is then discussed for the different speed lines by utilizing static pressure contour plots on the rotor casing.

The post-stall behavior is investigated by using the wall sensors on the casing to determine the number of stall cells, their size and rotational speed. The cell shape is defined by both the static and the total pressure measurements at various locations at midspan.

4.1. Experimental set-up adapted to the unstable range

The unstable operating points description requires some additional clarification regarding the experimental set-up.

The tests are performed while continuously closing the throttling valve with slow motion and suddenly re-opening it after the compressor enters into stall, starting from a stable point (often the near stall one).

The rakes are utilized to monitor the performance throughout the whole duration of the tests.

The probe FP3 is kept fixed at midspan, as shown in Figure 4.2, at 90°, in order to obtain a time-resolved total pressure measurement in a position close to the sensors.

Time-resolved pressure sensors are also employed for the detection of the unsteady phenomena, such as the instabilities appearing prior to stall and the flow breakdown.

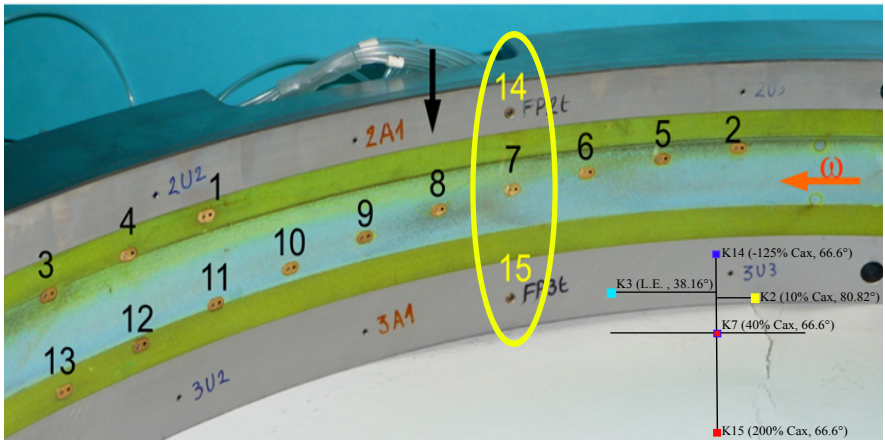


Figure 4.1.: Fast response pressure sensors axial and circumferential disposition.

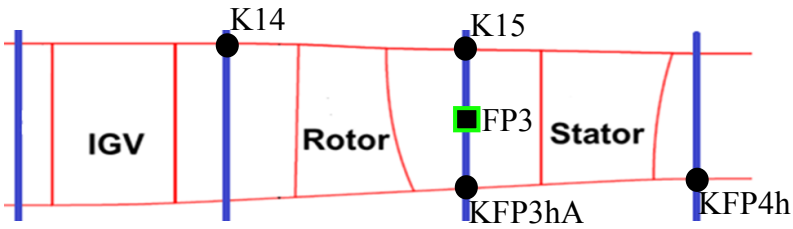


Figure 4.2.: Radial disposition of the sensors and probe FP3.

It is noteworthy to recall, and accurately define, the positioning of the sensors, as their location is fundamental not only for an appropriate detection of the number of stall cells, but also to distinguish axial and circumferential motions.

The whole stage is axially covered with fast response wall pressure sensors: as shown in Figure 4.2 the rotor casing is occupied from inlet to outlet, moreover at the hub rotor and stator outlet are located two sensors (KFP3hA, KFP4h). An axial motion of the flow field can be retrieved with the inserts located at an equal azimuthal position: K14, K7 and K15 on the rotor casing, whereas a tangential propagation is detected with the sensors K3 and K2, which are set at an axial distance of 10% of the axial chord and at 42° difference on the azimuthal coordinate (see Figure 4.1, right).

4.2. Overview on the unstable range

In the stability study of a compressor it is typically considered the static-to-total pressure rise, as it often provides a peak at the stall inception. The one retrieved for the Dream compressor in the R4-VKI facility is shown in Figure 4.3. For sake of completeness the total-to-total characteristic is also presented (Figure 4.4). Both of them are obtained with the rakes described in section 2.3.

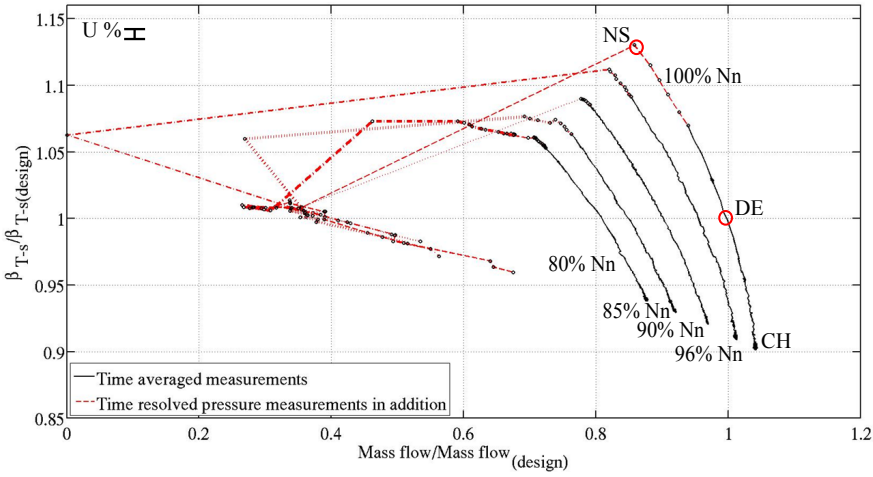


Figure 4.3.: Stage static-to-total performance map retrieved with the rakes.

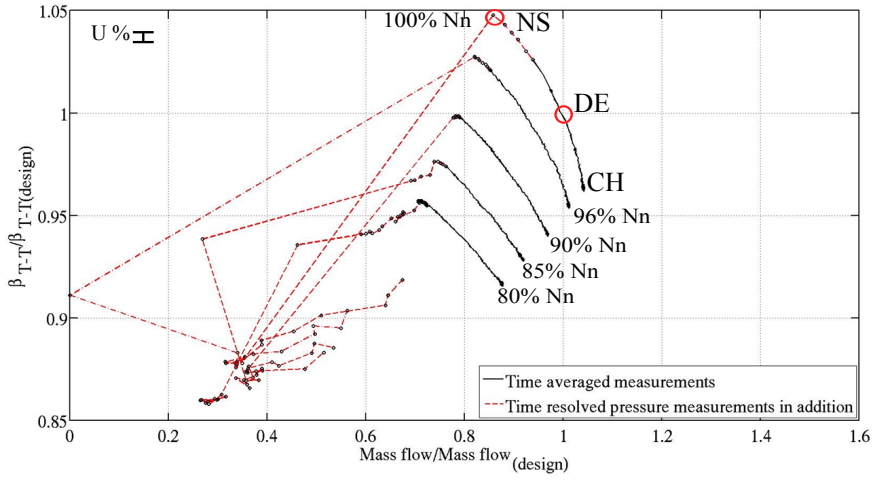


Figure 4.4.: Stage total-to-total performance map retrieved with the rakes.

On the static-to-total performance map the stability limit appears with a slope variation (see Figure 4.3). In the Dream compressor stage the stall inception behavior seems to vary with the rotational speed: at the high regimes (100% Nn and 96% Nn) the characteristc drops suddenly, while in the low speed range (85% and 80% Nn) it increases more before dropping.

The drop corresponds to the flow breakdown and the appearance of rotating stall. A sudden change in the slope of the characteristic, as for the higher regimes, is representative of an abrupt stall inception. A curve such as the one of the low speed range, in which a negative slope is changing before becoming positive, suggests the presence of higher losses, hence the presence of instabilities preceding the flow breakdown.

A typical time resolved pressure signal recorded in each of the speed lines investigated is presented in Figures 4.5 and 4.6. As an example is chosen the signal retrieved with the sensor at the wall rotor inlet. Not only the raw signal is presented but also the corresponding low pass filtered at 50 Hz.

In the time resolved pressure signals, presented in Figures 4.5 and 4.6, the flow breakdown appears as high amplitude fluctuations. At high rotational speed, at 100% and 96% rpm, only a small precursor fluctuation is visible (see Figure 4.5, case a, rev 450).

At 90% rpm the stall inception is preceded by instabilities modulated by a lower frequency component (between points 1 and 2 in Figure 4.5, case c). The instabilities have a period of approximately five revolutions, while the modulation of 26 revolutions. The closing of the throttling valve has the effect of starting the fully developed stall transient.

At 85% Nn the fluctuations arise at first as in the case at 90% Nn (points 1 and 2 in Figure 4.6, case d), then, while closing the throttling valve, the low frequency component disappears and the oscillations increase in amplitude (between points 2 and 3) until the drop of the pressure ratio (point 3).

At 80% Nn various phenomena are observed while closing the throttling valve. The link between the slope of the pressure rise curve and the oscillations is highlighted by presenting two consecutive parts of the transient: Figure 4.6, case e and case f. In point 1 (Figure 4.6, case e) the slope presents lower negative values and the instabilities appear as in the previous case (85% Nn, Figure 4.6, case d). The progressive reduction of the mass flow corresponds in this case to a decrease in the amplitude of the fluctuations (between points 2 and 3 in Figure 4.6, case f) before the stage enters into stall. This second stability zone is typical of centrifigal compressor and it is very rare on axial machines. This topic is thouroughly analyzed in the next section 4.3.3.

In order to have an overview on the kind of phenomena developing in the stage at the stall inception and in the post-stall behavior, the signals recorded in various locations of the machine and low pass filtered at 50 Hz are presented in Figures 4.7 and 4.8.

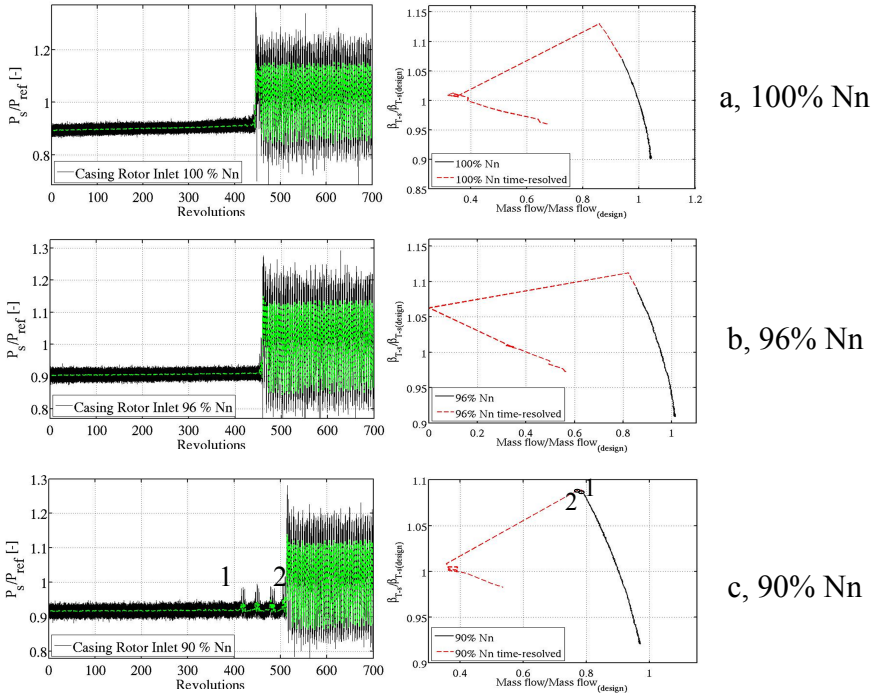


Figure 4.5.: Time-resolved pressure signal at the casing rotor inlet, static-to-total performance map.

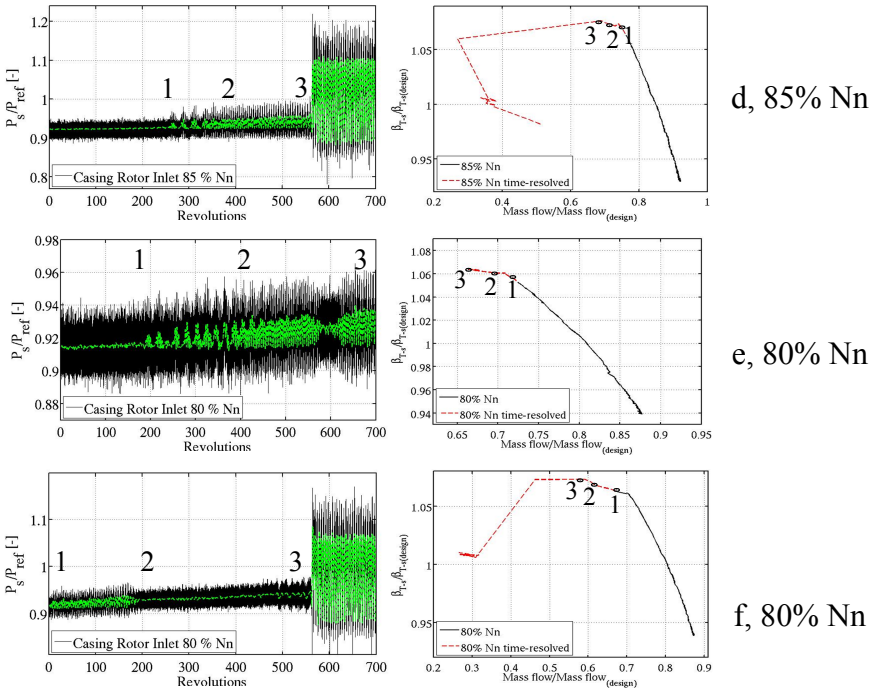


Figure 4.6.: Time-resolved pressure signal at the casing rotor inlet, static-to-total performance map.

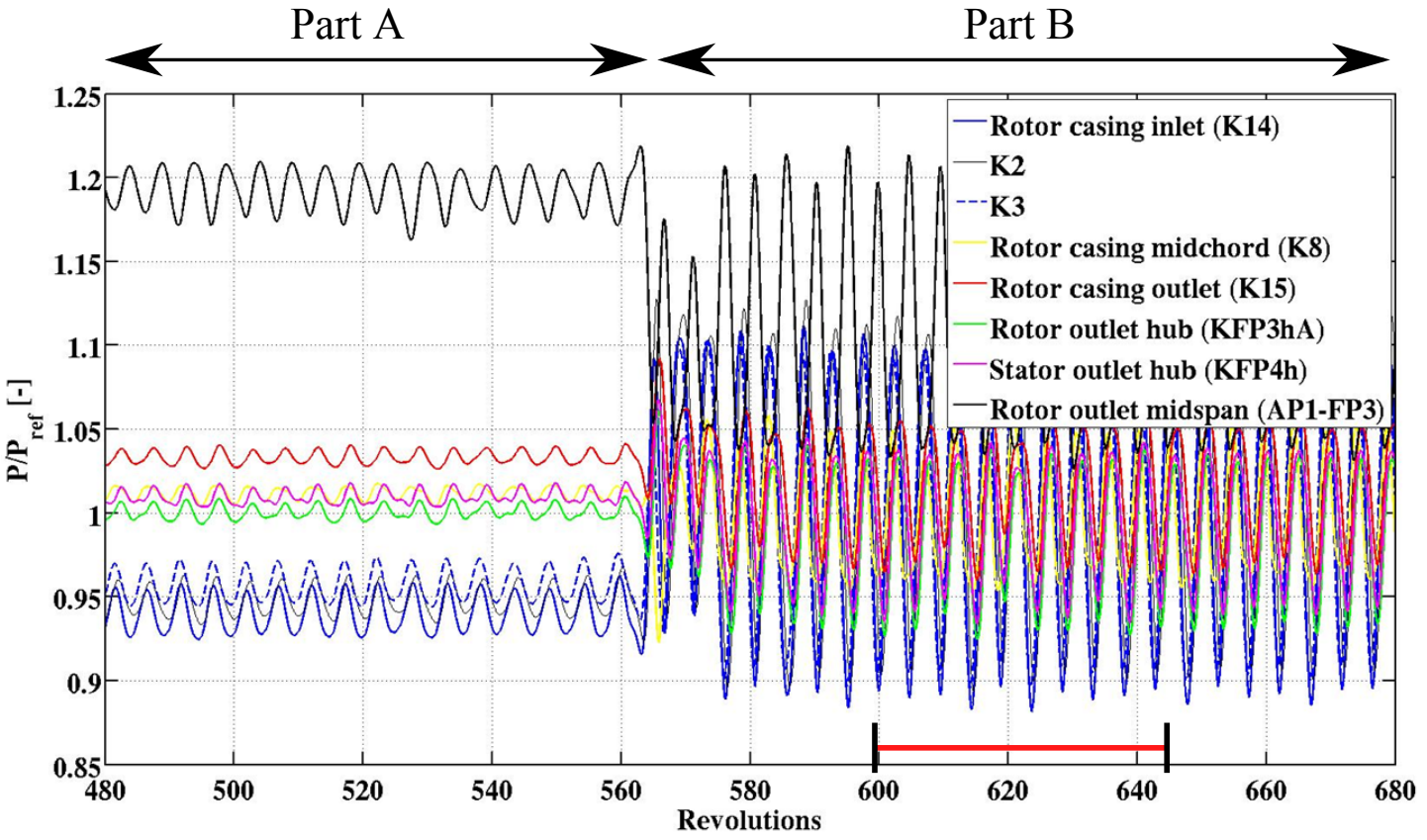


Figure 4.7.: Time resolved pressure signals (low-pass filtered at 50 Hz) at 85% Nn.

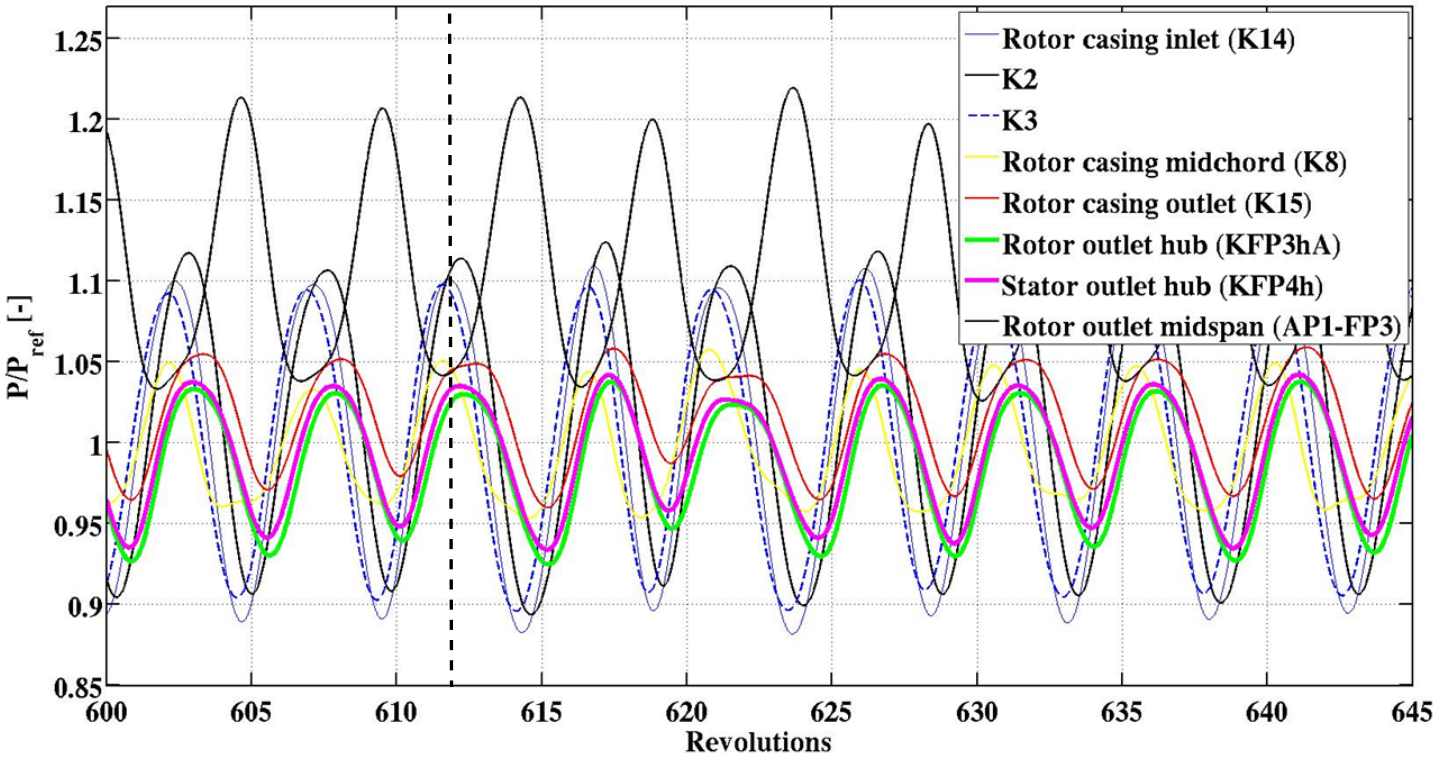


Figure 4.8.: Zoom of the time resolved pressure signals (low-pass filtered at 50 Hz) at 85% Nn shown in Figure 4.7 in the part highlighted in red.

For a better understanding on the patterns appearing at both the stall inception and after the flow breakdown, it is chosen the case 85% Nn, as it contains both. The signals covering axially the whole stage are presented: casing rotor inlet (K14), casing rotor outlet (K15), midspan rotor outlet (FP3), hub rotor outlet (KFP3hA), hub stator outlet (KFP4h). The sensors located most circumferentially apart K2 and K3 (see Figure 4.1) are shown in addition. The filtering frequency has been chosen according to the frequency analysis performed (see section 4.2.1) and it is focusing on the unstable phenomena.

The post-stall behavior is presented in Figure 4.8, which corresponds to the time interval underlined in red in Figure 4.7. A time shift between the sensors located more circumferentially apart (K2 and K3) appears in the maxima of the low pass filtered signals, while the time distance between the sensors at an equal azimuthal position (K14, K15, KFP3hA, KFP4h) is much lower. In the figure a vertical dashed line denotes the maxima of these points, suggesting the presence of a rotating phenomenon, such as rotating stall, which extends from the rotor inlet to the stator outlet. This behavior corresponds to a stable operating point in the performance map on the stalled characteristic. A more accurate description of the rotating stall patterns is provided in section 4.4.

Also the instabilities preceding the flow breakdown appear to extend to the whole stage (see Figure 4.7). This topic is thoroughly explained in section 4.3.

4.2.1. Frequency analysis

The frequency analysis is performed utilizing both a Fast-Fourier transformation and a wavelet transformation.

All the signals considered in the frequency analysis are low pass filtered at 50 Hz. The cutting frequency is chosen in order to focus on the stall phenomena and to distinguish the stall inception features from the flow breakdown, which are both appearing in the low frequency range. The comparison between the FFT of the filtered and the unfiltered signal is utilized to determine the cutting frequency.

Given its time-frequency analysis capability, the wavelet transformation is a suitable tool to detect the onset and the developing of flow instabilities such as those appearing in a stall transient (Lin et al. [99]). The most appropriate mother wavelet was found to be the Morlet with a centering frequency of 1 Hz and a time window of 0.001 s since it provides the best correlation with the signal. The frequency range analyzed is between 2 and 60 Hz.

As it can be inferred from the wavelet transformation, the number of stall cells remains constant during the transient: a splitting into a higher number of cells would correspond to a sudden increase in frequency. While the throttling valve is reopening the stall cell size reduces: during the tran-

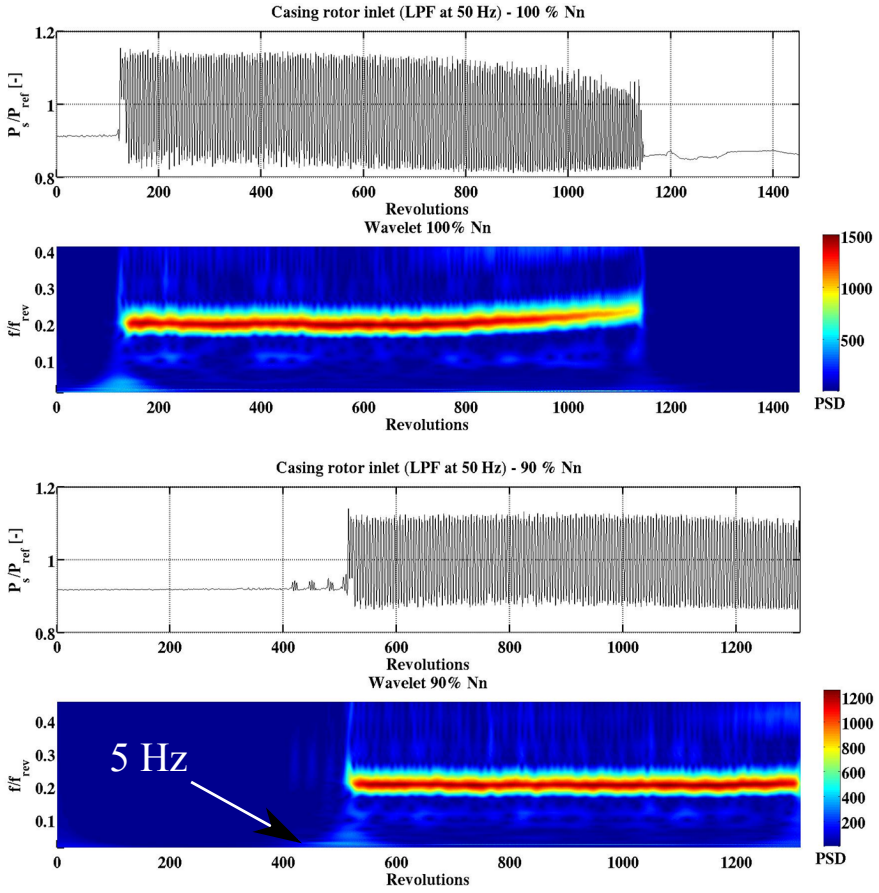


Figure 4.9.: Time-resolved signals (low pass filtered at 50Hz) and corresponding wavelet transformations for the cases 100% (top) and 90% Nn (bottom).

sient the time-resolved signal show an amplitude decrease, while the wavelet transformation present an increase in the stall cell frequency. This feature results particularly evident in the case 100% Nn (Figure 4.9): as the whole transient is represented the reduction in size is visible between revolutions 800 and 1100, before the stage stabilizes on the choke condition. This pattern is retrieved in all the rotational speeds investigated (see Figures 4.9 (bottom), 4.10 (bottom), 4.11 (bottom)).

The instabilities present a decreasing frequency while reaching the flow breakdown at all the speed lines investigated. This represents a typical issue of modal waves: as explained in McDougall et al. [41] and confirmed in Garnier et al. [22] modal waves start with an infinitely small circumferential

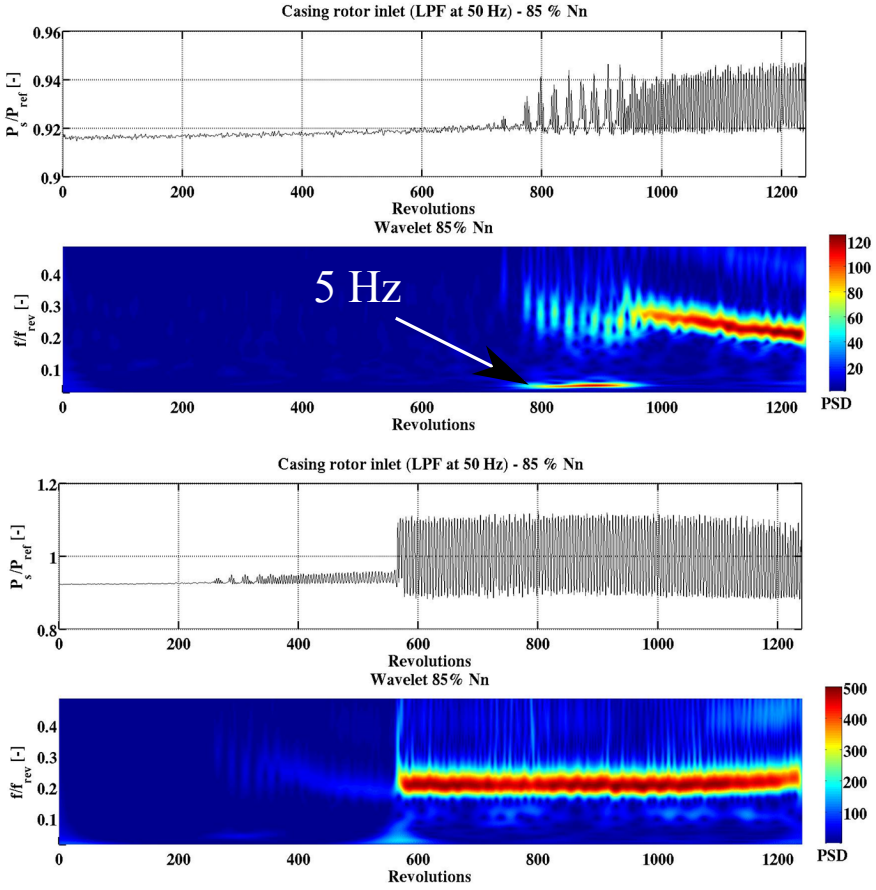


Figure 4.10.: Time-resolved signals (low pass filtered at 50Hz) and corresponding wavelet transformations for the case 85% Nn, at the stall inception (top) and during the whole transient(bottom).

perturbation which grows while increasing its size until reaching the rotating stall condition. This pattern is visible at 90% Nn (between revolutions 400 and 500), but is even more clear at 85% and 80% Nn: the Figures 4.10 (top), 4.11 (top) show a decreasing peak in the wavelets, which corresponds to an amplitude increase in the time-resolved signal.

The peculiarity of the Dream compressor stage is that the instabilities preceding the flow breakdown always appear at first modulated by a low frequency component, whereas modal waves are typically visible as continuous fluctuations. Moreover the modulating low frequency component seem to be constant at all the rotational speeds investigated (see Figures 4.10, 4.11) and approximately equal to 5 Hz. Further analyses are required to fully

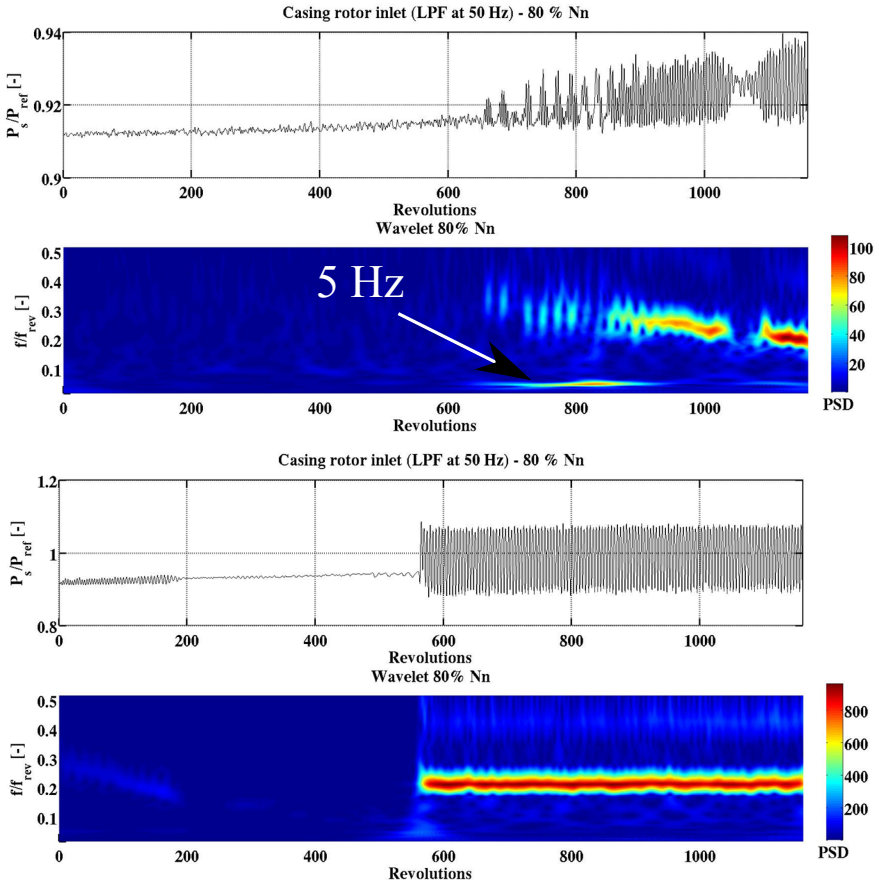


Figure 4.11.: Time-resolved signals (low pass filtered at 50Hz) and corresponding wavelet transformations for the case 80% Nn, at the stall inception (top) and during the whole transient(bottom).

understand its origin. The details of the discussion represents the objective of section 4.3.2.

On the other hand the low frequency peak which seems to trigger the rotating stall is due to the pressure drop, which in the spectrum appears as a pulse exciting all the frequencies, low range included.

4.3. Stall inception

4.3.1. Characterization of the instabilities

In the previous chapter it is shown that the Dream compressor stage is hub loaded, therefore it is likely to present hub corner stall, which often corresponds to modal waves type stall inception. This will be verified throughout this paragraph. As an example it is considered the speed line 85% Nn, in fact it contains both the modulated and the continuous instabilities.

The two "classical" stall inception patterns, shown in the contribution of Day [19], are considered at first in the analysis: spikes and modal waves.

As discussed in the literature survey, spikes are a localized flow breakdown happening at tip. This hypothesis has been immediately discarded: not only the stage is hub loaded and it is characterized by a small tip gap, but also the fluctuations cover the whole span. The pressure signals recorded at the rotor outlet at the hub, at the shroud and at midspan, presented in Figure 4.7 (part A) together with those at the rotor inlet, midchord and stator outlet, show indeed the presence of extended instabilities, whereas the spikes would be confined to the tip region. Oscillations cover indeed the whole stage: the time resolved pressure signals recorded at the rotor inlet and at the stator outlet in a corresponding circumferential position are in phase.

The analysis of the time resolved signal at various span locations at the rotor outlet may provide a better understanding on the nature of the stall inception and allows also to verify if the instabilities can be attributed to modal waves.

Figures 4.12 and 4.13 present the evolution along the characteristic at 85% Nn employing the pressure signals at the rotor outlet at midspan, at the hub and on the casing from the choke operating point until reaching the flow breakdown.

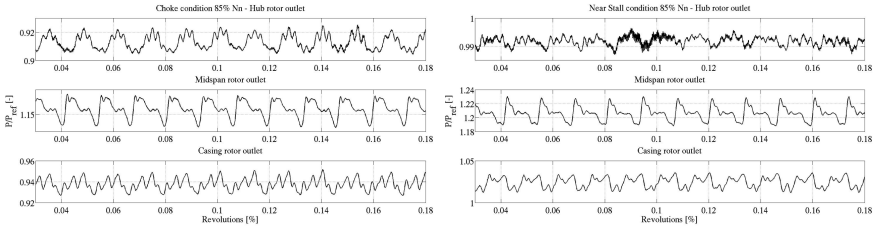


Figure 4.12.: Ensemble average of the signals at the rotor outlet at hub, midspan and tip at choke (left) and near stall (right) condition.

The choke condition is shown in Figure 4.12(left) in terms of ensemble average based on the rotor revolution frequency, detected by the trigger placed on the shaft, and in which 142 revolutions are considered. This acquisition has been obtained by recording the transient from a point between points 2 and 3 of Figure 4.6, case d and the reattachment to the pressure rise curve

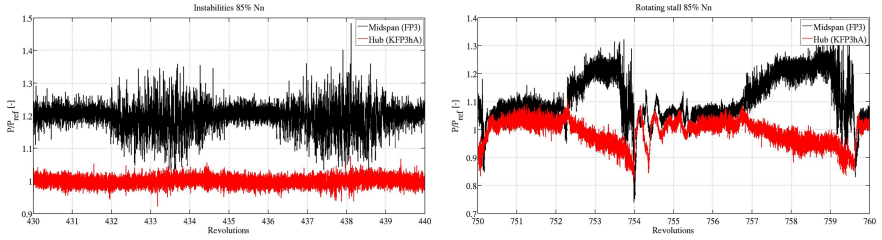


Figure 4.13.: Raw signal at hub and midspan corresponding to Part A (left) and part B (right) of the signal shown in Figure 4.7.

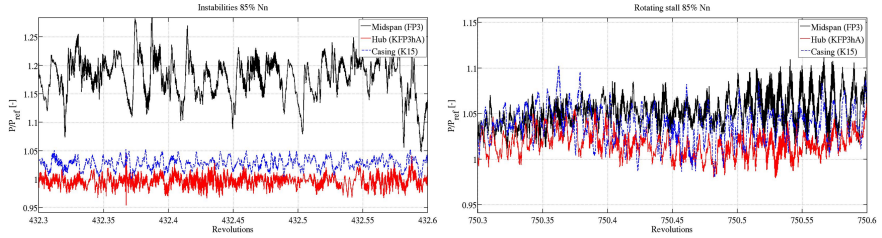


Figure 4.14.: Zoom on the raw signals presented in Figure 4.13.

at choke condition due to the opening of the throttling valve. The near stall condition is also presented (Figure 4.12, right) in terms of ensemble average based on the rotor revolution frequency and for which is considered an equal amount of revolutions. The average has been applied on the signals recorded before point 1 in Figure 4.6, case d. On the other hand the instabilities and the stall cell are presented in terms of raw signal.

The blade passages are visible in the ensemble average both at choke and at near stall condition. At near stall condition though the wakes appear to occupy a larger part of the blade passage than at choke. This effect is more evident in the hub region and at midspan than on the casing. When the instabilities arise (part A of Figure 4.7, for which is reported the raw signal in Figure 4.13) this effect is amplified: the raw signals show the blade passages at the tip, though affected by the presence of the instability, but not at the hub (see Figure 4.14, left). In the fully developed cell the blade passages are not observed at any span location (Figure 4.14, right).

The analysis of the instabilities has been carried out utilizing the Fast Fourier transformation shown in Figure 4.15 and focusing in the range of the blade passing frequency at 85%Nn. When the instabilities arise the blade passing frequency appears as a high peak. The amplitude of the peak is also linked to the quantity measured: the total pressure signal retrieved by the probe will provide a higher amplitude peak than the static pressure signal retrieved by the sensors in the casing and in the hub.

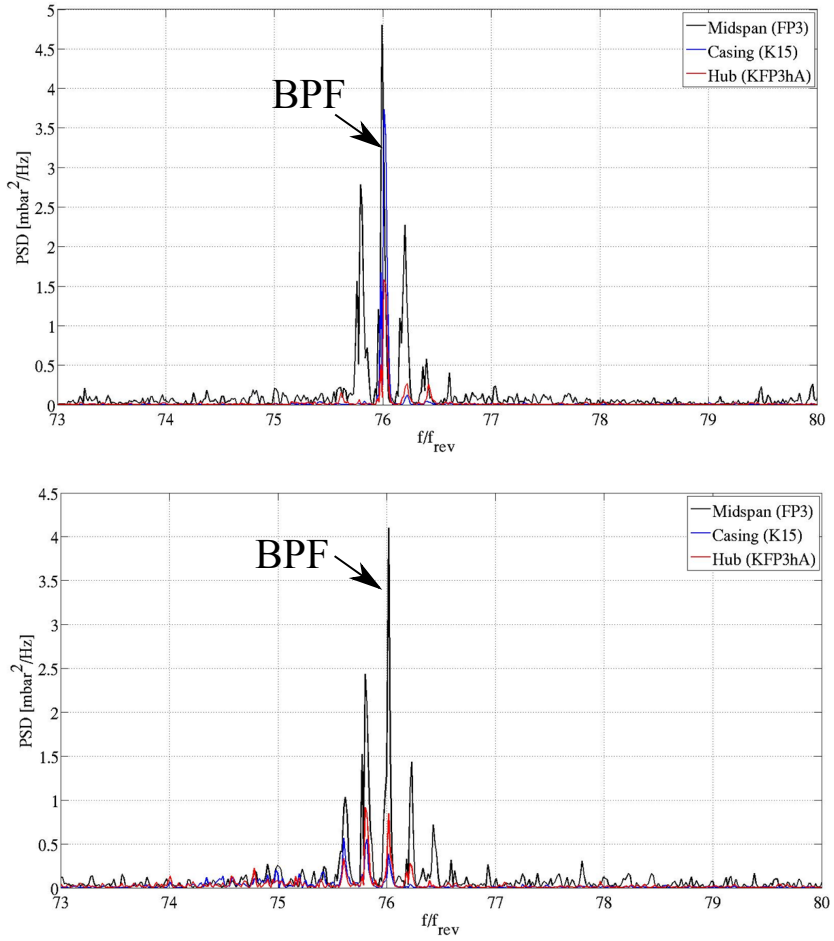


Figure 4.15.: Zoom around the BPF of the spectra retrieved for Part A (left) and Part B (right) of Figure 4.7.

The blade passing frequency appears as a high peak at midspan and on the casing when the instabilities arise (part A of Figure 4.7), whereas at the hub presents a lower amplitude (see Figure 4.15, top). During the transient, when the rotating cell is fully developed, both the peaks at the hub and at the tip disappear, meaning a full span separation (see Figure 4.15, bottom).

This may indicate that the instability starts to propagate from the hub and reaches the full span in the rotating stall condition. Indeed, as it was shown by McDougall [41] and then analyzed by Day [16], modal waves arise from a hub corner separation, and produce mass flow fluctuations extended to the whole span height. They are indeed described as waves characterized by very little variations in the radial direction, thus considered as bidimen-

sional.

The signal shows instabilities which at first are modulated by a low frequency component, and which then become continuous. Appropriate measurements would be performed by keeping the throttling valve opening fixed in order to evaluate the stability of the system. In this case it would also be useful to distinguish the two features (modulated and continuous instabilities) and to have a better understanding on their evolution in time. The casing carpet plots, such as those employed for the tip flows characterization in the previous chapter, allow a better understanding on the patterns retrieved, and to verify also if in both cases the influence of the separation reaches the tip region, as in the case presented by McDougall [41].

The casing static pressure carpet plot is presented in Figures 4.16 and 4.17. As in the graphs presented in the previous chapter for the description of the rotor tip flows (Figures 3.24, 3.25), a phase shift and a low pass filter at 40 kHz are applied to obtain them. In the stable operating points the flow field is dominated by the blade passing frequency, and the phase shift is based only on this frequency component, whereas in this case different phenomena have to be taken into account: the instability, the modulating component and the blade passing frequency. It is obvious consideration that the modulating component phase shift is applied only in the part of the signal where it appears, therefore not in the shift of the continuous instabilities.

The contribution of Day [16] thoroughly explains the propagating mechanism of modal waves and it corresponds to the thickening and thinning of the hub corner separation, which produces mass flow fluctuations as shown in Figure 1.24 and thus an axial velocity deficit. Figures 4.16 and 4.17 show high static pressure regions at the rotor inlet which may be attributed to an axial velocity variation such as the one presented by Day.

In the carpet plots it is also possible to observe the evolution of the instabilities: the period increases from 1.5-2 revolutions in the modulated ones to approximately 4 revolutions in the continuous ones. The latter corresponds to the typical period retrieved in the case of modal waves: the article of Day [19] reports values comprised between 3 and 5 revolutions.

The fluctuation evolution represents another typical feature of the modal waves: they arise as a small perturbation which grow with the closing of the throttling valve, until the flow breakdown is reached. In this case it is visible in the wavelets (Figure 4.10), as their frequency reduces during the transient, but also in the amplitude of the time-resolved signals, which increases (Figure 4.6).

The low frequency modulation appearing at the inception of the instabilities has the effect of periodically increasing and decreasing the period of the fluctuation (see Figure 4.16).

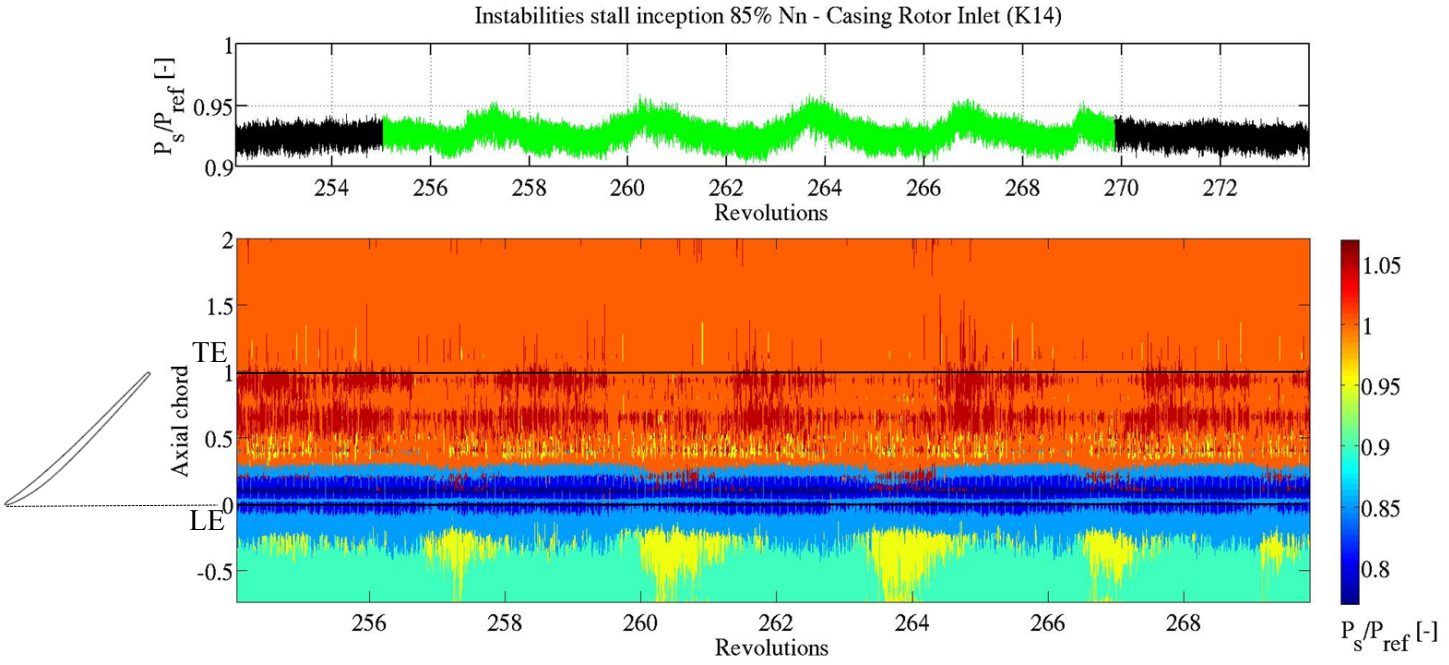


Figure 4.16.: Carpet plot of the modulated modal waves at 85% Nn (bottom), the corresponding raw signal at the rotor inlet (K14) is presented on top.

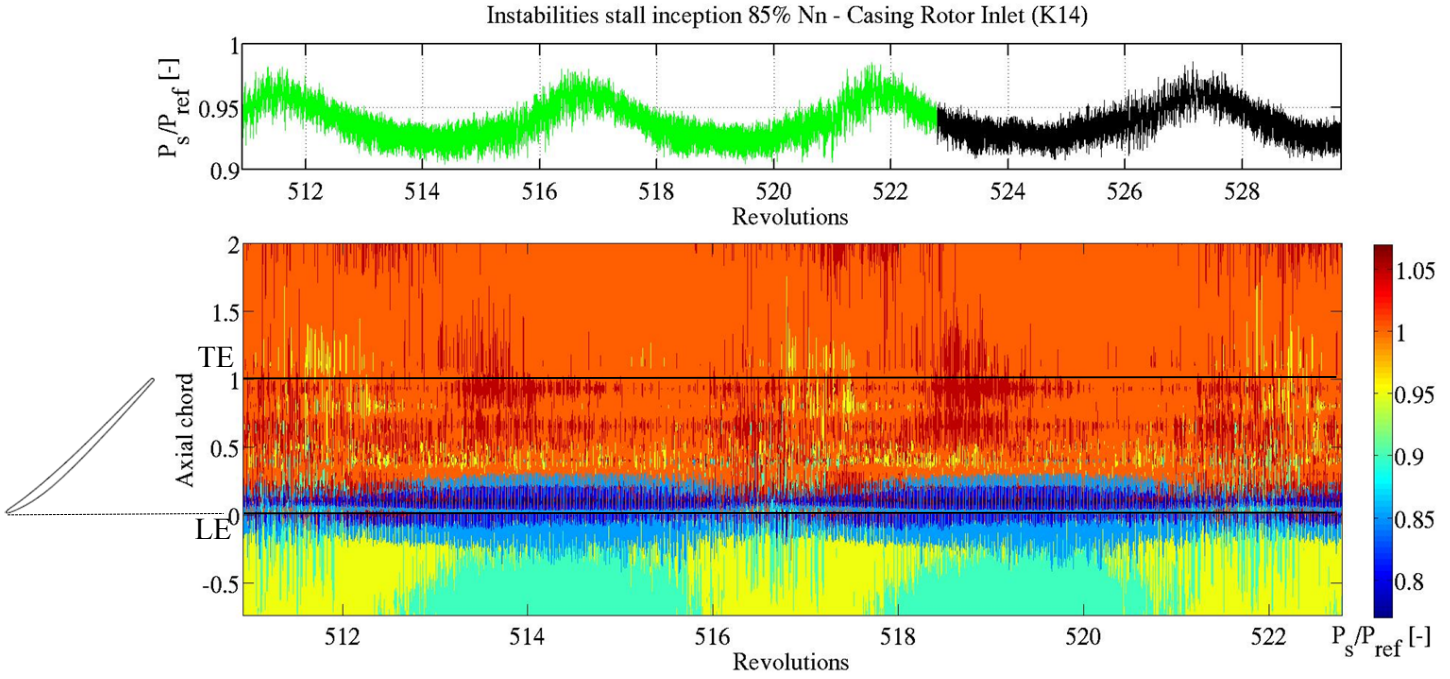


Figure 4.17.: Carpet plot of the continuous modal waves at 85% Nn (bottom), the corresponding raw signal at the rotor inlet (K14) is presented on top.

As the "classical" modal waves the instabilities increase their activity while lowering the rotational speed: at 100% and 96% Nn only one fluctuation is visible prior to the flow breakdown, whereas all the patterns described in the previous paragraph are retrieved in the low speed range. They are also found to be characterized by parameters similar to those of the stall cell: they occupy approximately 47% of the annulus (vs approximately 50% of the stall cell) and they rotate at approximately 22% of the shaft speed (vs 21% of the stall cell). A case with modal waves having similar features of those of the stall cell is presented by McDougall [41].

The hypothesis of modal waves seems therefore to be the most appropriate: not only they seem to arise from the hub, but they also grow in size until reaching the size of the fully developed stall cell, moreover their activity increases while lowering the rotational speed. All these features are matching with the modal waves characteristics, thus it is possible to conclude that the Dream compressor stage is likely to present a modal wave stall inception.

4.3.2. Explanation of the low frequency component

In the low speed range the Dream compressor stage shows a modulation of the modal waves by a lower frequency component, which corresponds approximately to 5 Hz for all the rotational speeds investigated.

This low frequency component is equal at all the rotational speeds at which it appears (i.e. 90, 85 and 80% Nn). The spectra retrieved for the three rotational speeds show this peculiarity very clearly. They are presented in Figure 4.18. The peak is equal to 4.7 Hz at 90% Nn, 5.2 Hz at 85% Nn, and 5.7 Hz at 80% Nn.

As shown in the spectra retrieved with different signals located in various parts of the stage and presented in Figures 4.18, this low frequency component is retrieved in the whole machine, therefore it is hypothesized to be linked to a surge-like motion, i.e. an axial motion involving the entire stage.

The time-resolved pressure signals are evaluated in order to distinguish the dominant sense of motion of this low frequency component. As an example it is considered the case at 85% Nn.

At first the low-pass filtered signals at 50 Hz are considered, however, as visible in Figure 4.19, it is only possible to distinguish a rotating component in the instabilities: the sensors located more circumferentially apart present a time shift, which results to be higher than the one of the sensors which are axially aligned.

The signals are therefore low-pass filtered at 10 Hz in order to focus on the low frequency component. The part of the signal analyzed comprises only the part in which the 5 Hz component is evident and periodic in the whole stage, i.e. between revolutions 240 and 340.

The determination of the axial or circumferential motion of the low frequency component would require the presence of sensors covering the whole

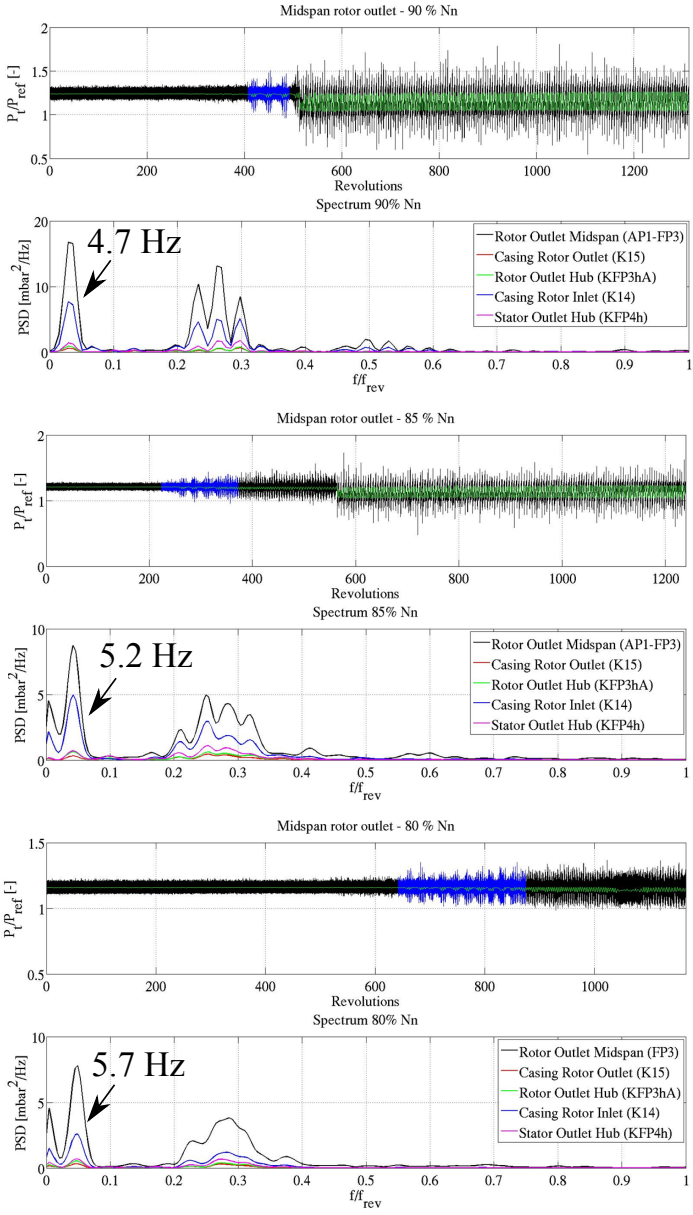


Figure 4.18.: Time resolved total pressure signal (top) retrieved during the stall transient at 90%, 85% and 80% Nn and corresponding spectrum (bottom) obtained for the pert of the transient in which the low frequency component appears (in blue in the top graphs).

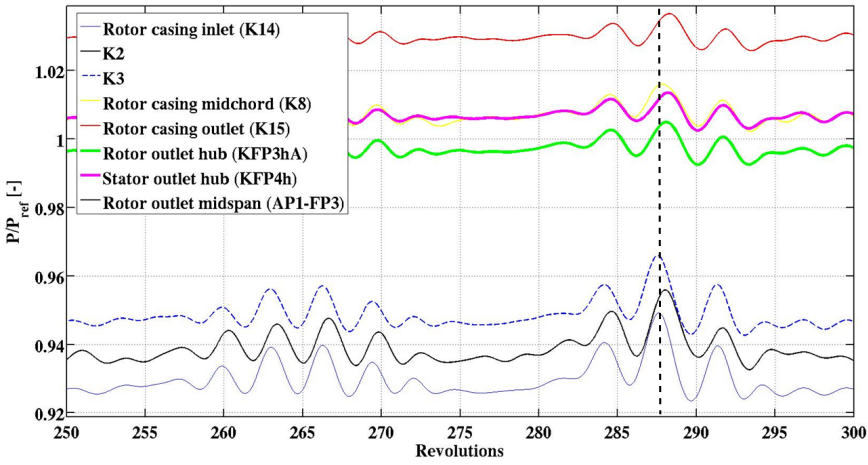


Figure 4.19.: Time resolved pressure signals low-pass filtered at 50 Hz retrieved at 85% Nn, in the condition where the low frequency component appears.

annulus at a corresponding axial location, as well as the presence of sensors at various axial locations in a corresponding azimuthal position. The latter condition is satisfied in the test section with the inserts located in the casing in planes 2 and 3, and the one at 40% of the rotor axial chord (respectively K14, K15, and K7, as shown in Figure 4.1). On the other hand the full circumference is not covered, however the sensors K3 and K2 are set at a tangential distance of 42° and an axial distance of 10% of the axial chord, therefore allowing the detection of a tangential motion.

At first it is verified if an axial motion appears, hence the three signals at a corresponding azimuthal location and shifted along the axial direction are considered (K14, K7, K15).

The three axial locations are characterized by very different pressure levels, resulting in graphs of difficult interpretation, thus the mean value is removed from the low-pass filtered signals at 10 Hz. The graph is reported in Figure 4.20. The maxima (in red) are considered as a reference to observe the time shifts on the curves.

The signals appear to be slightly shifted in time in the axial direction, as it could be in the case of surge. However the shift is not proportional to the distance between the sensors, and the time shift seem to increase during the transient. For a clearer interpretation the four consequent maxima are isolated and plotted in Figure 4.21, in which are represented in black, together with the corresponding maxima of the signals retrieved with the two sensors more circumferentially apart (K2 and K3, in red), and all the other sensors. The sensors located at a corresponding azimuthal position and a different

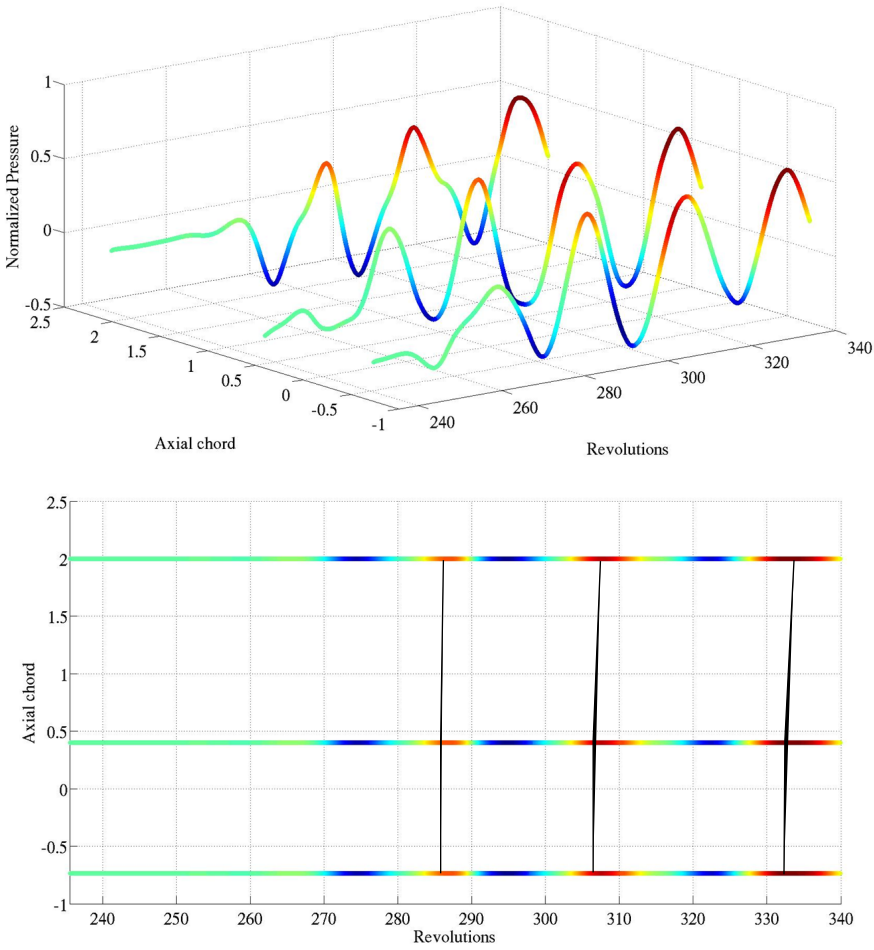


Figure 4.20.: Top: time-resolved static pressure signals retrieved with K14, K7 and K15 low pass filtered at 10 Hz. Bottom: top view of the 3D plot presented on the right.

axial location are represented with a big dot (two couples are presented: K1 and K11, and K4 and K12).

The plot of the signals retrieved with sensors at a very close axial location but far in the azimuthal direction (K2 and K3) show a time shift, thus meaning a not purely axial motion. The sensors located at different axial locations (K14, K7, K15) but at a corresponding azimuthal position also present a time shift. The shifts visible in the two directions are of the same order of magnitude.

The graph indicates also that the motion is not tangential: a purely cir-

cumferential movement would present maxima at the same time for the sensors located at an equal azimuthal position and distant in the axial direction, such as K12 and K4, and K11 and K1. Also it is likely to recognize a start of the motion from the aft part of the rotor blade which moves upward towards the rotor inlet. Therefore the low frequency component does not seem to be subjected to an axial nor a circumferential movement but to a helicoidal one, and it is likely to arise in the rear part of the rotor blade and to follow the flow streamlines, propagating upstream.

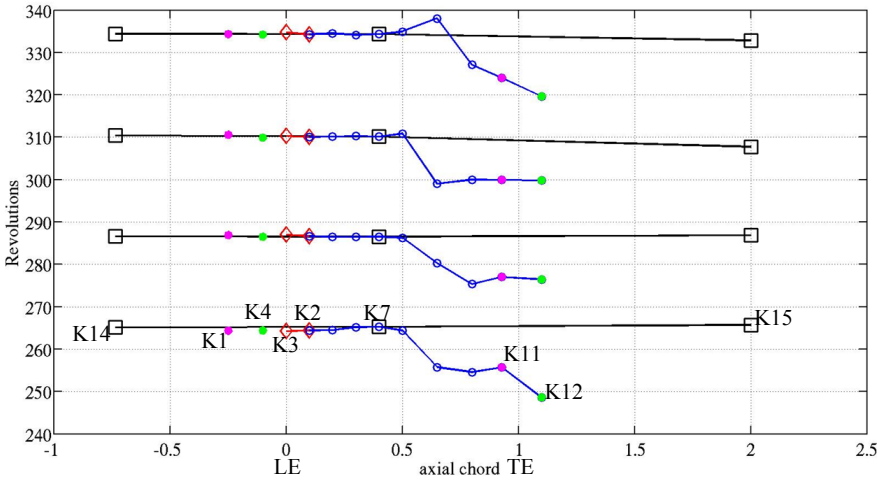


Figure 4.21.: Maxima of the curves shown in Figure 4.20, in black. The maxima of equivalent curves retrieved with the other sensors on the casing are also represented.

The same graph obtained with the shifted signals, which is presented in Figure 4.22, shows a similar trend. The signals are shifted with the same methodology applied to retrieve Figure 4.16.

The shifted signals have the property of "following" the flow field, which is represented in its three main frequency components. Also in this case the 5 Hz component appears to propagate from the aft part of the rotor blade following a helix towards the rotor inlet.

A shift of the signals in the axial direction provides a similar trend, confirming the results retrieved in the other two cases.

Similar results are retrieved also for the other two speed lines investigated: 90% and 80% Nn.

The hypothesis of surge-like motion is thus discarded. On the other hand the possibility of a helix motion suggests the presence of a wave which propagates on the flow streamlines, moving upstream.

The second hypothesis is to link this frequency to an acoustic mode. In fact the Helmholtz frequency of the facility results to be approximately equal

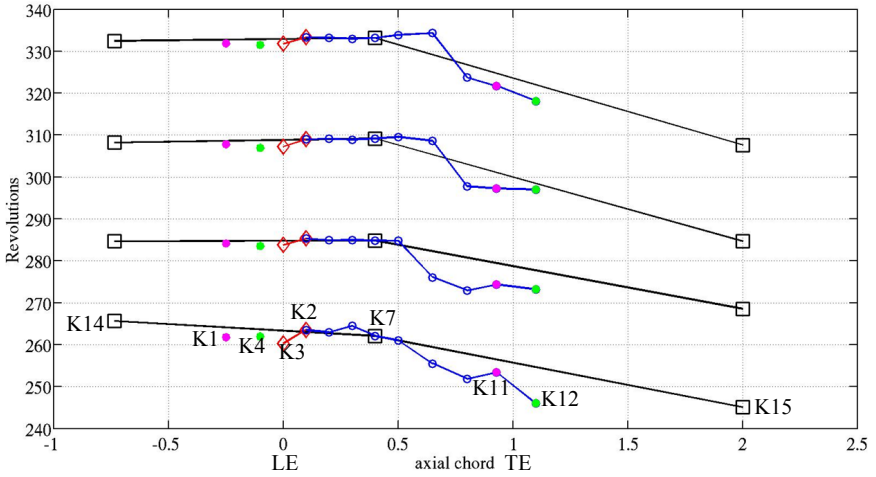


Figure 4.22.: Corresponding representation of the one of Figure 4.21 for the shifted signals.

to 5 Hz (computed by taking into account the reservoir as volume, and the test section as duct).

The 5 Hz component is visible in the signals also in stable conditions, though it is not confined in a specific location of the machine, nor in a defined operating condition. On the other hand it arises only at the stability limit in the low speed range.

The graphs commented before (Figures 4.21, 4.22) show that this low frequency propagates from the aft part of the rotor blade moving towards the inlet. The previous paragraph hypothesizes a hub corner separation which extends to a hub corner stall while closing the throttling valve. This may explain why the low-frequency component starts to propagate from the rear of the rotor blade: at a certain closure of the throttling valve the hub corner separation reaches the condition of zero velocity (such as in an acoustic field) and the acoustic mode is able to propagate.

Adequate measurements would be performed while keeping the throttling valve at a constant opening. In any case the closure of the throttling valve do not seem modify the presence of this low frequency component. On a corresponding speed line it always appears at a certain closure of the throttling valve. Thus a slow or a fast throttling has the mere effect of remaining for longer or shorter time at the condition in which the low frequency component develops, resulting in a higher or lower number of fluctuations observed in the time-resolved signal.

The acoustic mode hypothesis seems to match with the propagation direction of the low frequency component, and also coherent with the fact that it does not significantly vary with the rotational speed.

The hypothesis of the acoustic resonance of the flow field is therefore the most accredited.

As a conclusion it is possible to say that a striking proof of a helicoidal motion of the low frequency component would be provided by measurements performed with fast-response sensors covering the whole annulus at various axial locations, as well as with additional fast-response sensors covering the whole stage from the inlet to the outlet, located at a corresponding azimuthal position.

4.3.3. Redistribution of the flow field at 80% rpm

The Dream compressor stage presents for one of the speed lines investigated a second stability zone prior to the flow breakdown, as sometimes is remarked in centrifugal compressors. This phenomenon is observed in the case 80% Nn and it is characterized on the performance map by a higher negative slope, different from the one of the first stable region, and by the absence of instabilities, as it is shown in Figure 4.6 (cases e, f). This rotational speed differs from all the others investigated, which mostly show a sudden drop in the characteristic (cases 100%, 96% and 90% Nn), accompanied by a slope variation (from negative to positive).

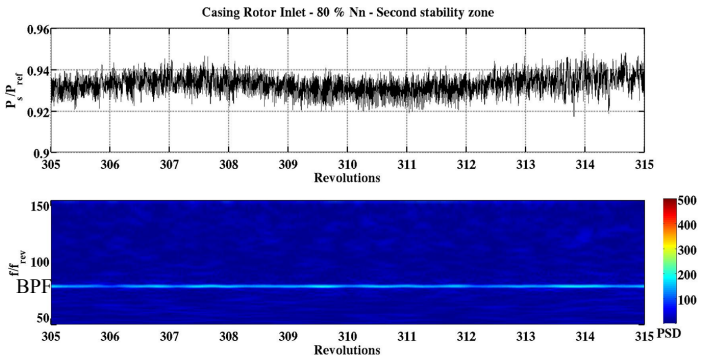


Figure 4.23.: Signal retrieved at the casing rotor inlet (K14, top) in the second stability zone at 80% Nn and corresponding wavelet transformation (bottom).

In the literature, both Diez et al. [100] and Pampreen [101] present a case of a centrifugal compressor having a second stability zone for one of the speed lines in the low speed range. Diez et al. [100] remark a flow reorganization characterized by a tip separation in this operating range.

In the case of the Dream compressor stage, given the hypothesis of hub corner stall, it is at first supposed a rearrangement of the flow field with a hub separation. It is verified by applying wavelet transformations to the time-resolved pressure signals. By studying different transducers at various

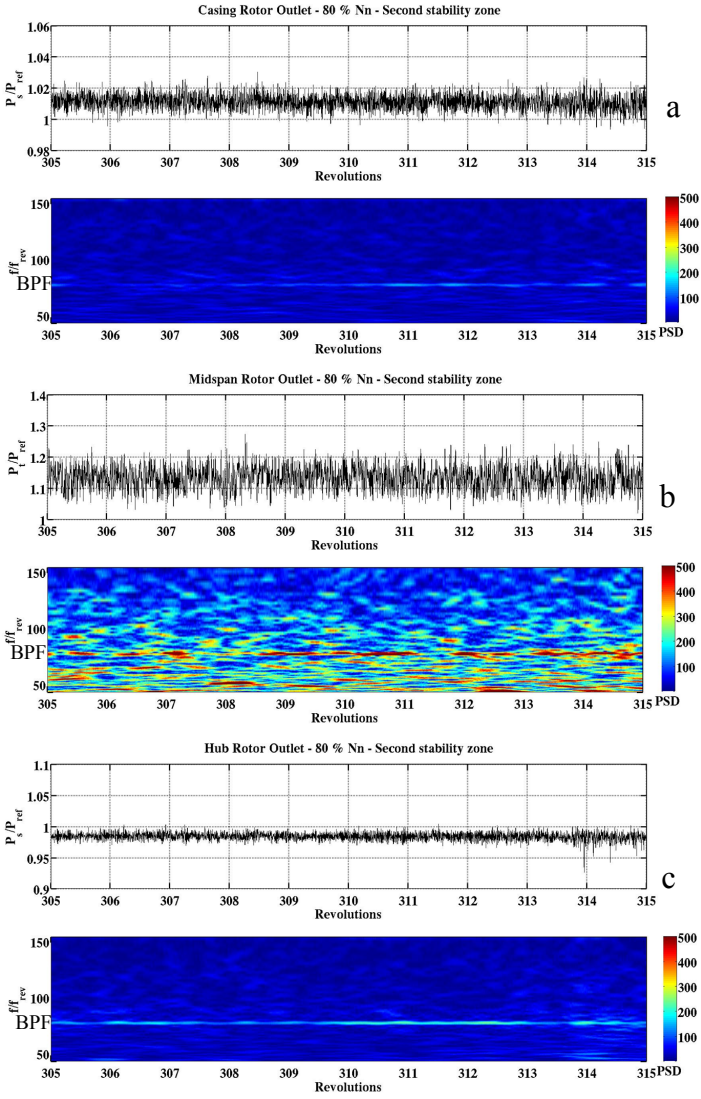


Figure 4.24.: a: Signal retrieved at the casing rotor outlet (K15, top) in the second stability zone at 80% Nn and corresponding wavelet transformation (bottom). b: Signal retrieved at midspan rotor outlet (FP3, top) in the second stability zone at 80% Nn and corresponding wavelet transformation (bottom). c: Signal retrieved at hub rotor outlet (KFP3hA, top) in the second stability zone at 80% Nn and corresponding wavelet transformation (bottom).

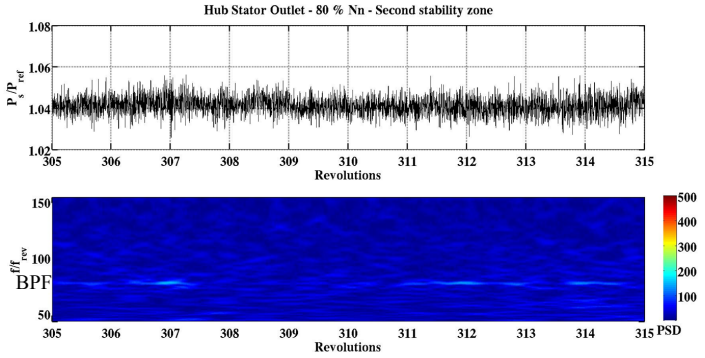


Figure 4.25.: Signal retrieved at hub stator outlet (KFP4h, top) in the second stability zone at 80% Nn and corresponding wavelet transformation (bottom).

machine locations it is possible to understand in which part of the stage the separation occurs. The wavelets are indeed observed in a range which comprises the blade passing frequency.

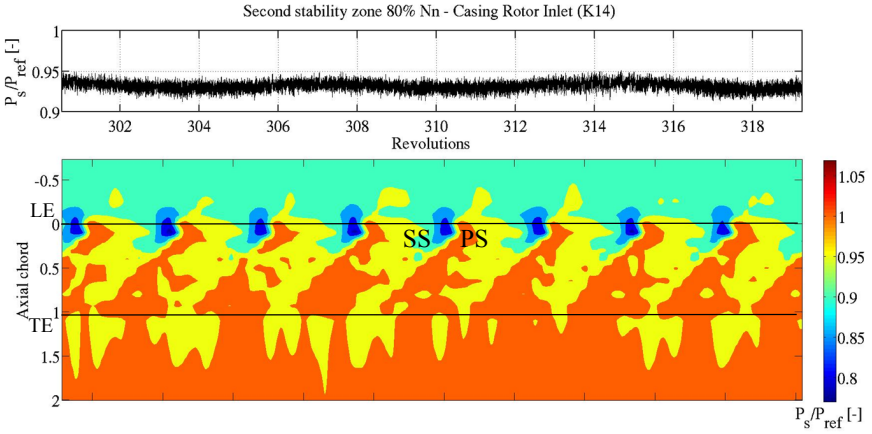


Figure 4.26.: Top: Time resolved static pressure signal at the rotor inlet at 80% Nn, second stability zone. Bottom: Instantaneous static pressure distribution on the rotor casing at 80% Nn, second stability zone.

The wavelets chosen are a sum of complex sinewaves, as they provide the best correlation with the signal. The frequency range considered is between 5 and 18 kHz and the window is 1 μs.

The analysis is applied to the following signals: at the casing rotor inlet (sensor K14) and outlet (K15), at the rotor outlet at midspan (probe FP3) and hub (sensor KFP3hA), and at the hub stator outlet (sensor KFP4h).

The time-resolved pressure signals and the corresponding wavelet transformations are reported in Figures 4.23, 4.24 and 4.25.

The frequency analysis indicates a partially separated rotor: on the contrary to the first hypothesis the rotor hub seem to present a clean flow, as the blade passing frequency is visible, whereas the tip region appears to be separated in the aft part, reaching midspan. The stator blade row is also affected by separation, however it is not possible to determine its extension as only the signal at the hub stator outlet is available.

The rotor casing carpet plot enables to provide a further explanation. The methodology applied follows the one utilized in the stable operating points for Figures 3.24, 3.25. In this case the plot is obtained by filtering at first the signals at 40 kHz, then by shifting the signals and considering only the blade passing frequency, as no other structures are detected in this time window with the frequency analysis (Figures 4.23, 4.24 and 4.25). The graph is presented in Figure 4.26.

The figure highlights a separation in the aft part of the tip rotor blade, which is possibly due to the size increase of the tip leakage flows caused by the higher incidence.

Centrifugal compressors are typically characterized by a higher pressure ratio than axial machines, and local recirculations do not impact significantly on the performance, as they are compensated by the radius increase. Either the high degree of reaction or the rotor blade radial loading distribution may similarly impact on the Dream compressor stage: either the stator or one of the two parts (upper or lower) of the rotor blade is able to compensate the local recirculation.

A complete explanation could be provided only by additional measurements at the rotor inlet and outlet and at the stator outlet as well.

4.4. Characterization of the stall cell

This section targets the analysis of the stage in its unstable range, at the drop of the characteristic, when the flow breakdown takes place. As previously stated, this study is based on the time-resolved pressure measurements retrieved in the various measurement planes in the machine. The number of cells is at first computed, together with their rotational speed and size, for all the speed lines. The shape of the cell is then illustrated, defining its leading and trailing edge and its extension across the machine.

4.4.1. Number of stall cells

As inferred from the frequency analysis (section 4.2.1), the number of cells is constant for the whole duration of the transient. In order to compute the number of cells, their rotational speed and size, the methodology introduced by Levy [102] is employed.

The detection of the number of stall cells is typically retrieved with sensors located in different circumferential locations at an equal axial position. Their distribution is usually not equally spaced around the circumference, in case the number of cells is a multiple of the number of sensors. The pressure signals are modeled as sinewaves oscillating in time (denoted with t):

$$p = Bsin(\omega_{OSC}t + \phi) \tag{4.1}$$

in which B represents the amplitude of the sinewave, ω_{OSC} the pulsation and ϕ the phase shift.

The signals retrieved by K2 and K3 are chosen, as they represent the most neighboring sensors in the axial direction and the most separated circumferentially. The signals are low pass filtered at 50 Hz, in order to be modeled as sinewaves, and shifted in space by their angular distance. The number of cells appearing in the transient can be determined by a graph representing the two signals separated by their angular distance, and repeating the first one, as shown in Figure 4.27.

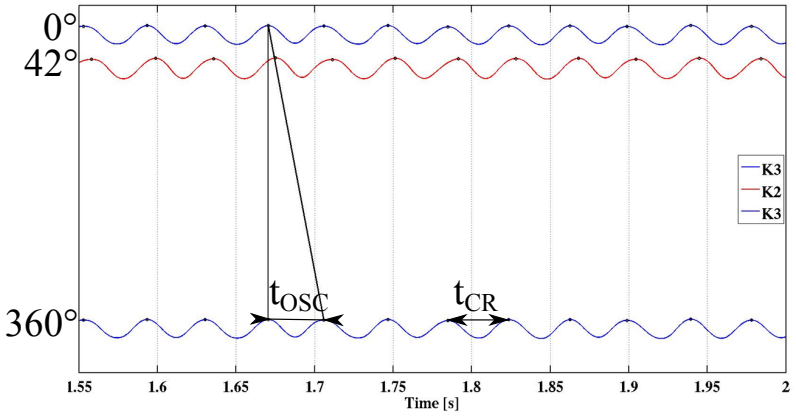


Figure 4.27.: Graphic method to determine the number of cells.

The peaks of the various signals are due to the same stall cell and can be linked by a line of constant phase, therefore the number of stall cells can be determined. The time of the complete rotation of the stall cell t_{CR} (CR stands for Cell Rotation) is defined by the crossing of the constant phase line and the pressure signal of the sensor at 0° and 360°. The time of a pressure fluctuation t_{OSC} (OSC stands for oscillation) is defined as the time between two maxima of the signal. The number of stall cells is determined as:

$$n = \frac{t_{CR}}{t_{OSC}} \tag{4.2}$$

In all the cases examined the number of cells has been found to be 1.

Being defined the number of stall cells and the frequency of one pressure fluctuation f_{OSC}, the frequency of the cell rotation is calculated as:

$$f_{CR} = \frac{f_{OSC}}{n} \tag{4.3}$$

The value obtained corresponds to the peak retrieved in the frequency analysis, indicated in table 4.1 as f_{CR} Levy. This confirms the presence of one stall cell as hypothesized. The stall cell has been found to rotate at approximately 20% of the rotational speed of the machine in all the tests performed.

The percentage circumferential extension of the cell is also computed:

$$\phi_{covered} = \Delta t_{cell} \times f_{CR} \times 100 \tag{4.4}$$

where Δt_{cell} is the period of the fluctuation between two maxima, f_{CR} is the frequency of the stall cell.

A summary of all the values retrieved in the various acquisitions is presented in Table 4.1. The size and the percentage speed of the cell remain constant for the different rotational speeds.

Table 4.1.: Stall cell characteristics.

$\%Nn$	Nbr Cells	f_{CR} FFT	f_{CR} Levy	$\phi\%$	$\omega\%$	f_{CR}/f_{Rot}
100%	1	29.5	29.1	49.9	20.8	0.20
96%	1	28.5	28.2	49.9	21.0	0.20
90%	1	26.9	25.9	49.7	20.6	0.21
85%	1	25.8	24.7	49.5	21.2	0.21
80%	1	24.8	21.9	50.9	21.3	0.21

4.4.2. Shape of the stall cell

This section provides a more detailed representation of the stall cell. To this aim the time-resolved pressure measurements are employed and post-processing techniques such as phase average locked to the cell period, wavelet transformations and representation of the casing static pressure are applied.

In order to be coherent with the previous paragraphs in which the stall inception is described, as an example is considered the case 85% Nn. However the results concerning the shape of the stall cell retrieved in the other rotational speeds, given the low-pass filtered signals investigated [103], do not expect to vary significantly from this one.

4.4.2.1. Phase average locked to the stall cell

In order to capture the mean component of the rotating stall cell a phase average locked to the cell period is applied. The RMS, skewness and kurtosis

are also computed to detect its random component and the accelerations (or decelerations) of the flow field.

As the signals are recorded in the whole transient, from the stable, near stall condition to the unstable one, the average is computed only in the part exhibiting rotating stall in a time interval of 2 s (corresponding to 248 revolutions, see Figure 4.28). The signals chosen for the phase averaged representation are those up- and downstream the rotor on the casing, at the rotor outlet at midspan and hub and at the hub stator outlet respectively.

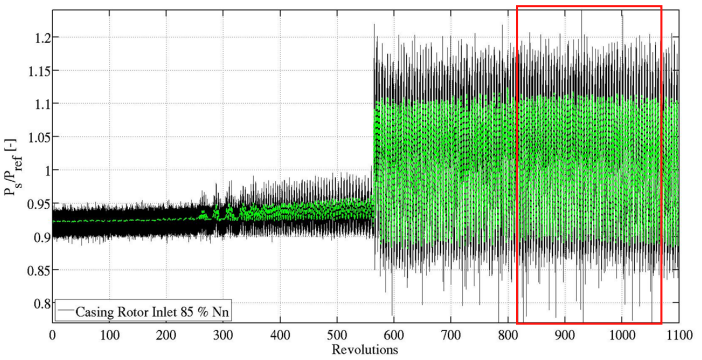


Figure 4.28.: Time-resolved pressure signal and interval to which the phase average has been applied.

All the different sensors and the probe are acquiring simultaneously but are spatially shifted as shown in section 2.4.2. The angular space shift has to be compensated as explained in section 3.3.1.2.

In the unstable range the flow field is dominated by two rotating structures: the stall cell and the phenomena comprised within the blade passage. The former is characterized by a rotational speed equal to 21% of the shaft speed (Ω_{shaft}), the latter by a rotational speed equal to $76 \times \Omega_{shaft}$. Both have to be taken into account in the time lag.

All the signals are shifted with respect to the probe position, which is considered as the reference signal.

Once the signals have been shifted with respect to the probe considering the time lags, the phase average is applied. The probe (reference) signal is divided according to the minima, as shown in Figure 4.29, in order to have an average independent on the cell period. Then each segment is divided in 200 classes and averaged as explained in Appendix B.1.

The other signals are divided according to the same reference points and averaged.

The RMS and skewness are computed as explained in Appendix 3.3.1.1.The results obtained are shown in Figures 4.30, 4.31, 4.32 and will be discussed in the next section.

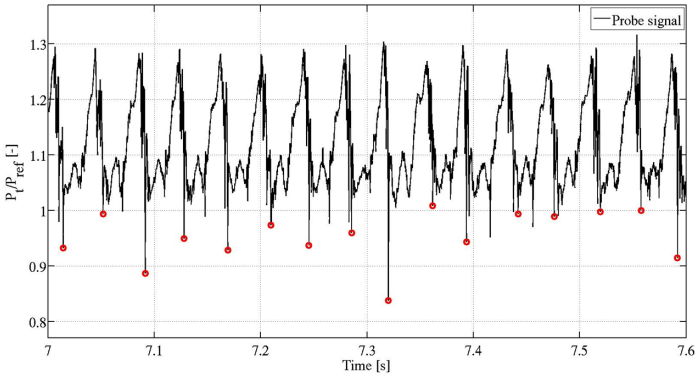


Figure 4.29.: Probe signal division for phase average computation.

4.4.2.2. Discussion on the shape of the stall cell

For the sake of clarity the leading and the trailing edge of the stall cell are defined with respect to a relative frame of the stall cell, as shown in the examples provided by Cumpsty and Greitzer [23], Day [79], Mathioudakis and Breugelmans [24]. In the absolute frame the stall cell is rotating in the same direction as the rotor at 21% of the shaft speed, therefore the rotor blades are entering the stall cell from the trailing edge and leaving it from the leading edge.

Rotor outlet

The first objective is the definition of the stall cell boundaries, i.e. the leading and the trailing edge. Their location can be established with the phase average locked to the cell, and the corresponding RMS, skewness and kurtosis, which are presented in Figure 4.30.

As already proven by Das and Jiang [77], [78], Breugelmans et al. [80] and Day [79], the cell affects the flow field in such a way to create abrupt changes in the various quantities. Indeed in the phase averages (Figure 4.30) the total pressure drops while the static pressure rises.

Mathioudakis and Breugelmans [24], in their detailed description of the flow field, remark how the trailing edge is characterized by a static pressure peak in the outer wall downstream the rotor. This pressure difference across the row is such to create reversed flow.

In the Dream compressor the downstream pressure trace rises without presenting a peak, though it is still possible to link it to the trailing edge of the cell: an RMS peak appears at the same location (at approximately 1.55) for all the quantities downstream the rotor.

The leading edge is located at around 1.05: the flow field is forced to surround the cell when facing it, therefore accelerates yielding a static pressure

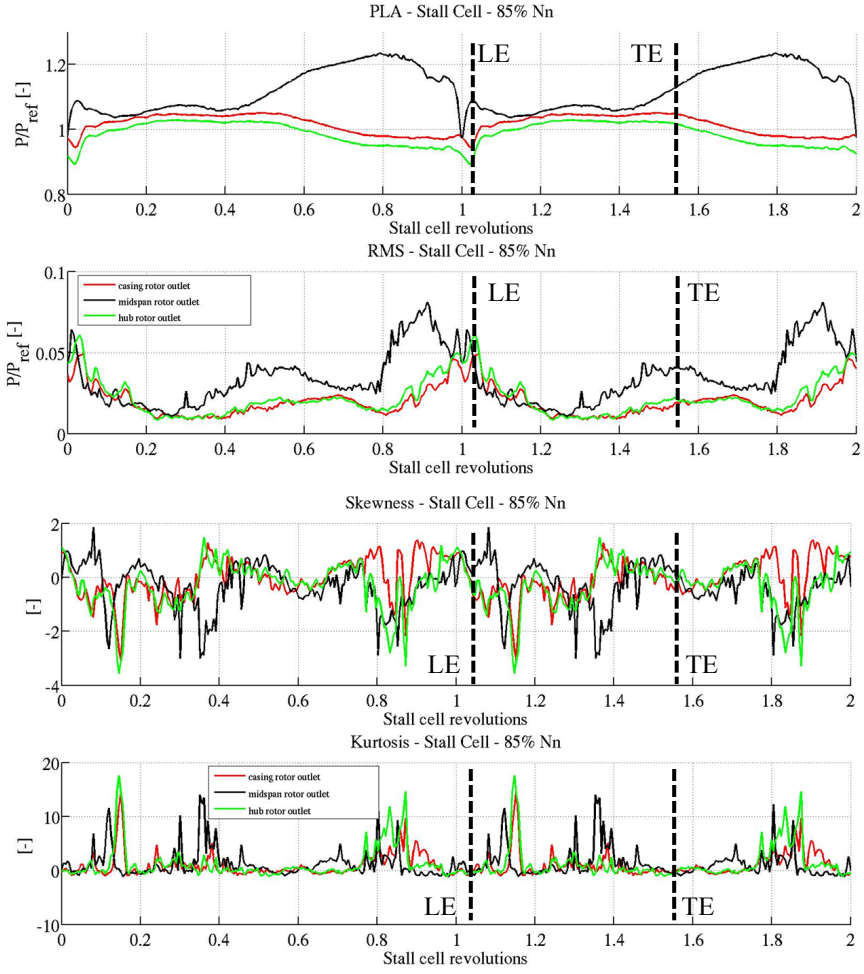


Figure 4.30.: Phase locked average of the stall cell retrieved at the rotor outlet at tip (K15), at midspan (FP3) and hub (KFP3hA) and corresponding RMS, skewness and kurtosis.

minimum together with a positive peak of skewness in the rotor downstream traces.

The total pressure minimum is attributed to a probe effect: for a short time the probe is facing a reversed flow and the sensor is reading a static pressure instead of a total one. The acceleration of the flow field is visible as a positive skewness at around 1.

In some cases the leading edge in the hub region is likely to appear slightly before than at the tip, therefore the stall cell varies its circumferential extent along the radius. This is visible in the wavelet transformations where the

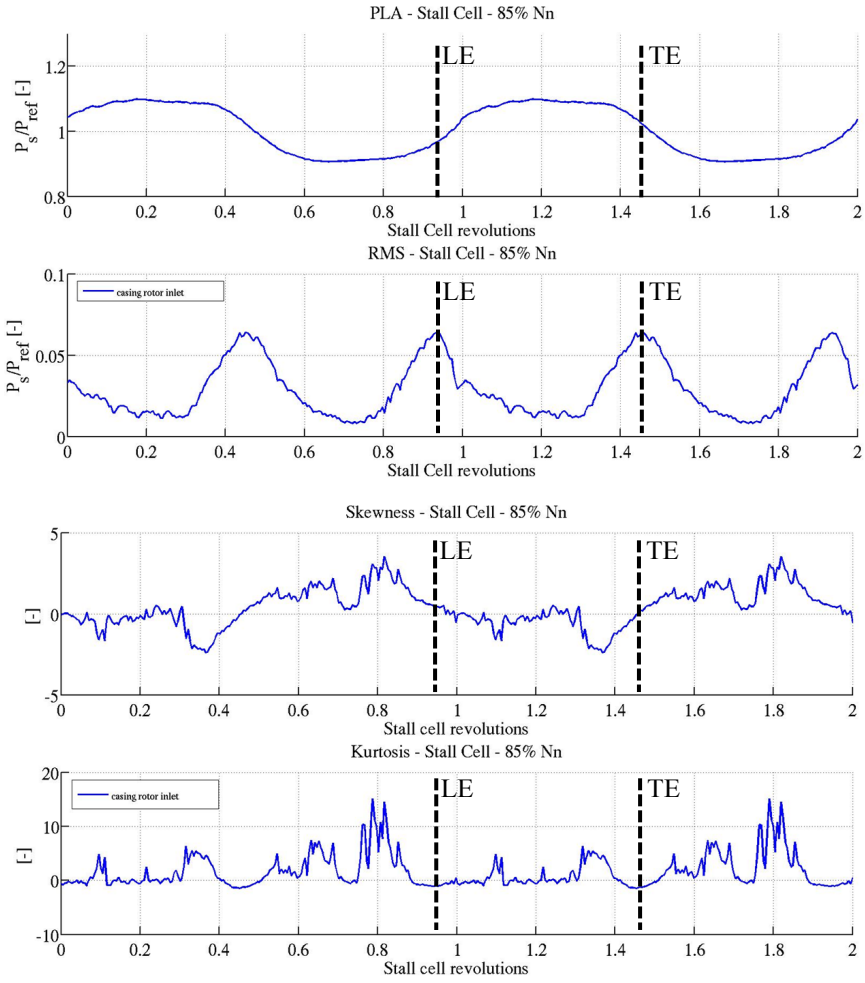


Figure 4.31.: Phase locked average of the stall cell retrieved at the casing rotor inlet (K14) and corresponding RMS, skewness and kurtosis.

BPF appears for longer time at the hub than at the tip. The kurtosis indeed, which represents the intermittency of the phenomenon, i.e. its fluctuations in time, presents higher values at the cell leading edge. This behavior is shown across the whole stage.

The phase average is able to provide a global idea about the stall cell shape. However the amount of sensors in the casing allow a detailed representation of the cell by means of a carpet plot, which is shown in Figure 4.33. The signals have been shifted as in the phase average. The stall cell period is approximately 4 revolutions, therefore the graph is on 6 revolutions in order

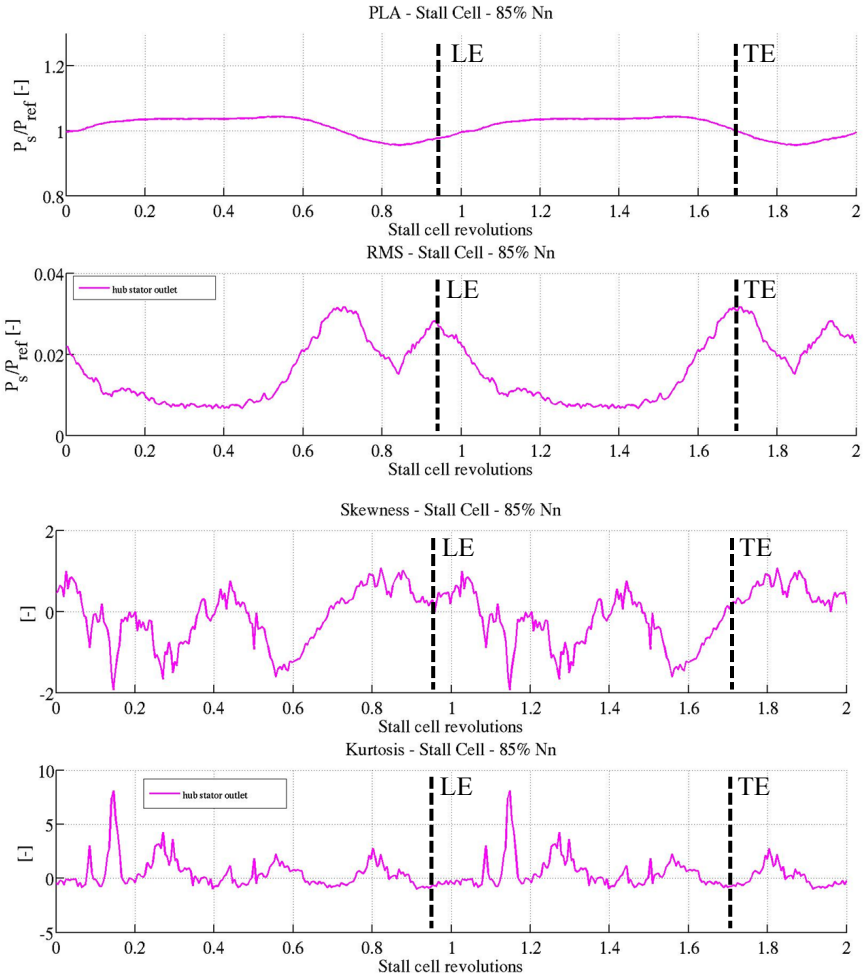


Figure 4.32.: Phase locked average of the stall cell retrieved at the hub stator outlet (KFP4h) and corresponding RMS, skewness and kurtosis.

to cover the whole cell and to be able to distinguish it from the "clean" flow.

The outlet pressure growth, previously identified at the cell trailing edge, is located at approximately revolution 834.8. Downstream the rotor a region of constant pressure indicates a separation zone which occupies the whole cell, from its leading to its trailing edge.

Wavelets transformations are also employed to define the stall cell extent. As in the case of the second stability zone presented in section 4.3.3, the wavelets focus on the blade passing frequency in order to understand where

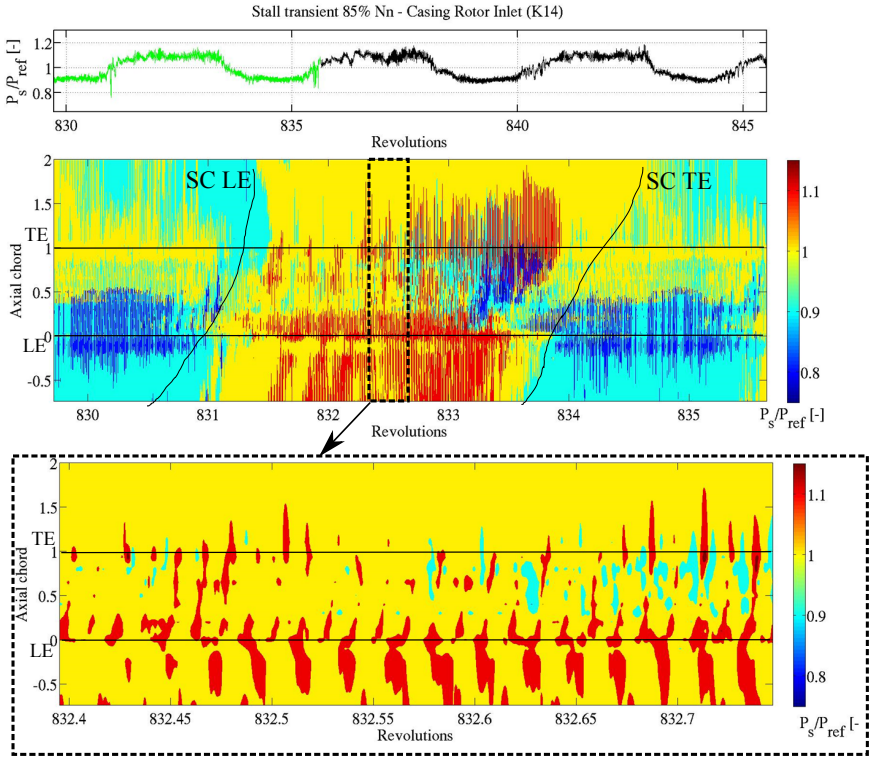


Figure 4.33.: Top: Raw signal retrieved at the casing rotor inlet (top), and casing static pressure contour plot retrieved during rotating stall. The revolutions represented in the contour plot are highlighted in green in the raw signal. Bottom: zoom on revolution 832.

the separations occur. The wavelets utilized correspond to those previously presented (section 4.3.3). Their representation is shown in Figures 4.35, 4.36, 4.37: not only the rotor outlet is considered but also the casing rotor inlet and the hub stator outlet.

As shown in Figures 4.36 (a, b, c), the cell affects the spectrum at the three span locations. The cell downstream the rotor is thus likely to be full span. The skewness hub and tip traces are approximately null within the cell and present a similar trend.

Rotor inlet

In the carpet plot the stall cell emerges between revolutions 830.5 and 833.5 and it is skewed across the rotor towards the trailing edge. The RMS peaks up- and downstream the wheel are indeed shifted (see Figures 4.31 and 4.30). The “clean” flow seem to accelerate to surround the leading

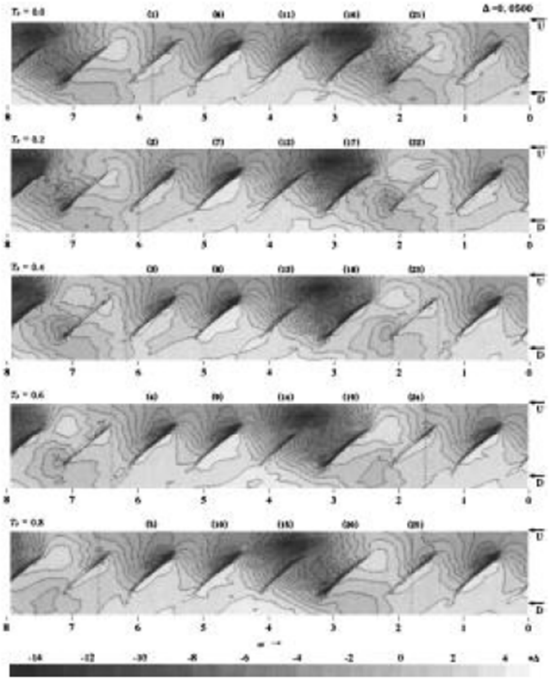


Figure 4.34.: "Variation of ensemble-averaged pressure distribution on the casing" in the case presented by Inoue [14].

edge of the cell and appears as a zone of constant pressure at $rev \approx 830.5$, covering the rotor from its inlet to its outlet. In the contour it is denoted by the black line (SC LE (stall cell leading edge)) on the left.

The skewness of the rotor upstream trace, shown in Figure 4.31, provides a further indication to this: the positive peak at around 0.85 corresponds to the acceleration of the flow field. The cell seem also to vary its size at this location, appearing in a kurtosis peak.

The literature shows typically high tangential velocities upstream the rotor and low ones downstream. Also in the Dream compressor stage the upstream flow field presents a different behavior with respect to the outlet: a separation zone at the stall cell leading edge seems to be followed by the formation of defined structures propagating in the circumferential direction until the cell trailing edge. These flow structures appear as oscillating static pressure with a period of approximately two blade passages (see Figure 4.33 (bottom)).

As explained in section 3.3.1.2 (rotating instabilities), one of the peaks attributed to the rotating instabilities in stable conditions, corresponds to approximately half of the BPF and it is the only component remaining during rotating stall as a wide peak. It can be hypothesized that, as for the

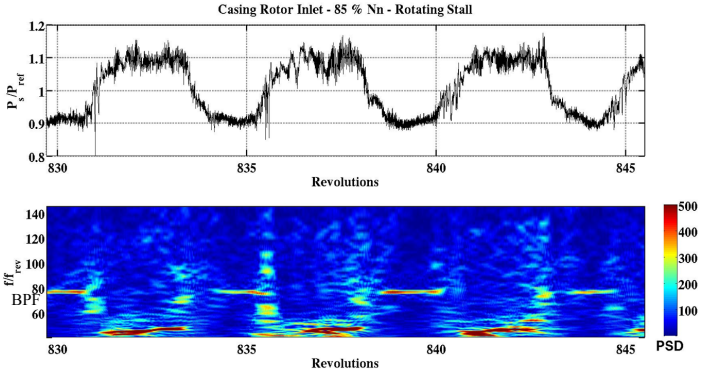


Figure 4.35.: Signal retrieved at casing rotor inlet (K14, top) during rotating stall at 85% Nn and corresponding wavelet transformation (bottom).

second stability zone, the tip region is separated whereas the hub is not: low pressure areas are indeed visible within the blade passages in the carpet plot, and in the wavelets the BPF is not visible within the stall cell(Figure 4.35).

In fact the zoom in the stall cell (Figure 4.33) shows a constant pressure zone within the blade passage, which is possible to remark from the high pressure trace along the chord.

On the other hand the succession of low and high pressure regions ahead of the rotor leading edge indicate a defined flow structure. The hypothesis is to attribute it to tornado like vortices such as those presented by Inoue [14], being indeed observed as the alternation of high and low pressure zones, occupying one or two blade passages. Figure 4.34 reports the outcome presented by Inoue.

The low pressure region occupying the whole blade passage observed by Inoue (Figure 4.34) is linked to the increase of angle of attack, and it is explained as a tornado like vortex released on the blade suction surface to reduce the blade circulation. It is anchored on one side to the blade suction surface, at the location where it is not separated and to the casing on the other side.

In the Dream compressor stage it is therefore supposed that the stall cell covers only a part of the span at the rotor inlet.

On the other hand the zone comprised between revolution 830 and 830.5 seem to be affected by a full span separation as it presents constant pressure: if the formation of defined structures, as between revolutions 831.5 and 833.5, causes a tip separation, their absence may yield a full span separation.

Additional measurements at the rotor inlet would enable to complete the description of the flow topology.

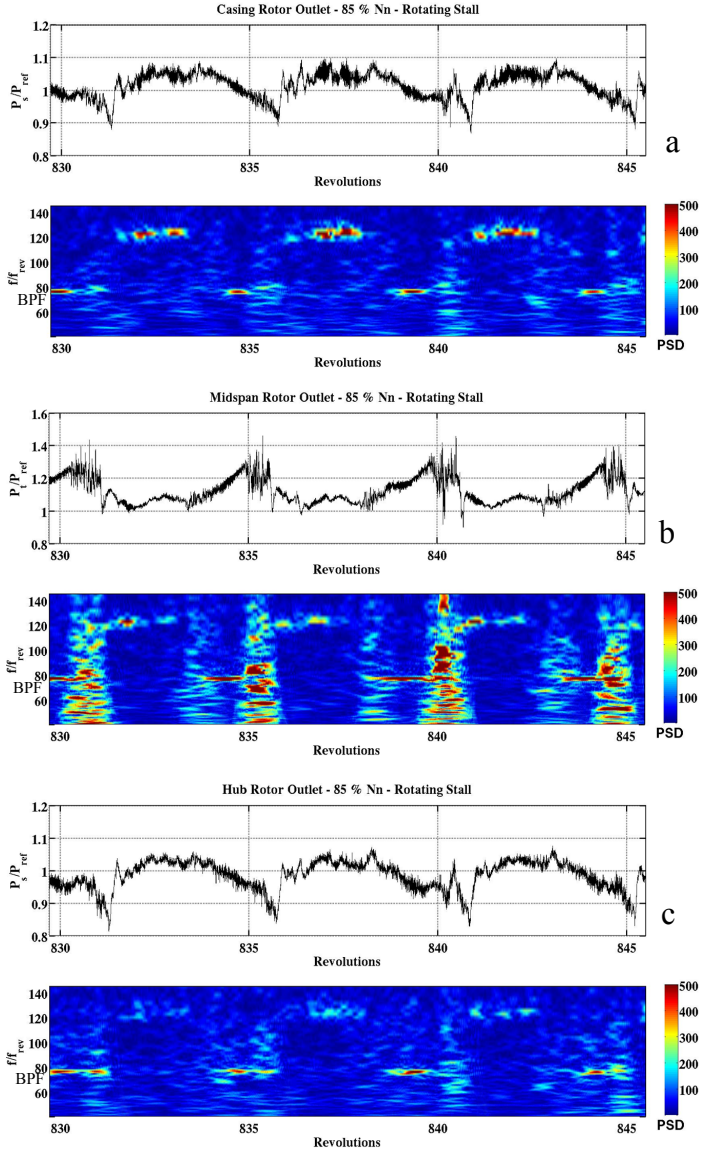


Figure 4.36.: a: Signal retrieved at casing rotor outlet (K15, top) during rotating stall at 85% Nn and corresponding wavelet transformation (bottom). b: Signal retrieved at casing rotor outlet (FP3, top) during rotating stall at 85% Nn and corresponding wavelet transformation (bottom). c: Signal retrieved at casing rotor outlet (KFP3hA, top) during rotating stall at 85% Nn and corresponding wavelet transformation (bottom).

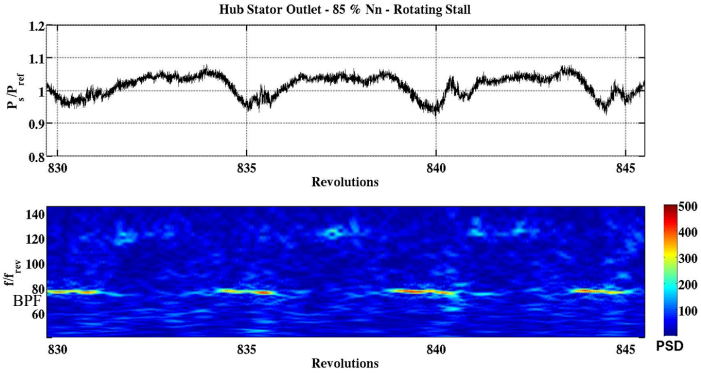


Figure 4.37.: Signal retrieved at hub stator outlet (KFP4h, top) during rotating stall at 85% Nn and corresponding wavelet transformation (bottom).

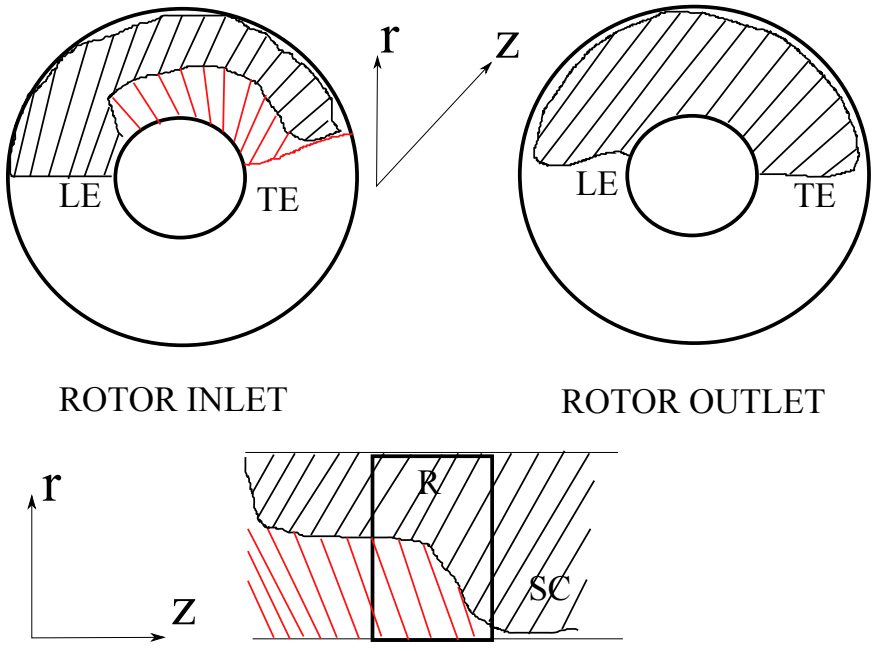


Figure 4.38.: Principle sketch of the shape of the cell up- and downstream the rotor, and across it.

Stall cell extension across the stage

The inlet and outlet description of the stall cell hypothesize a radial extension which varies along the axis: upstream the rotor is locally part-span, while downstream is full span. Figure 4.38 shows a possible representation

of the cell.

Still to understand is what happens at the LE of the stall cell where the wavelets show a "pulse" exciting all the spectrum (see Figure 4.36 (b)). Also it would be interesting to verify the tip separation at the rotor inlet with additional measurements.

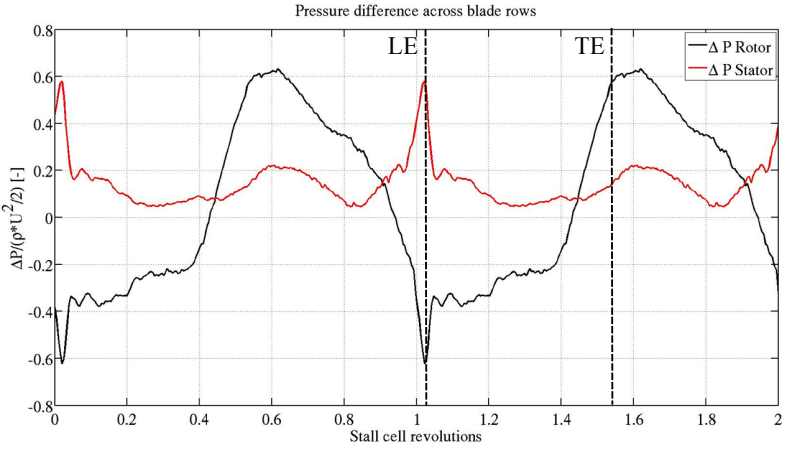


Figure 4.39.: Pressure differences across the blade rows.

The description of the stall cell across the stage is not trivial, as only one sensor at the hub stator outlet is available in addition to those employed for the description around the rotor blade row. The phase average locked to the cell and the corresponding RMS suggest a wider extension with respect to the rotor outlet: the stall cell is visible in the zone of higher pressure and between the two RMS peaks, which are located at 0.9 and 1.7.

In order to have further information about its extent it is possible to determine the leading and the trailing edge by applying pressure differences across the blade rows. Indeed, as shown in Cumpsty and Greitzer [23]:

1. the trailing edge resides at the local positive peak on the ΔP_{Rotor}, at the local negative peak on the ΔP_{Stator}

2. the leading edge resides at the local negative peak on the ΔP_{Rotor}, at the local positive peak on the on the ΔP_{Stator}

The difference has been computed for the rotor with the phase locked averages at the inlet and at the outlet casing (K14 and K15 respectively), for the stator with those of the sensors at the hub rotor outlet and hub stator outlet (KFP3hA and KFP4h respectively). The differences have been non-dimensionalized with the inlet kinetic energy and the result is shown in Figure 4.39. The leading edge assigned with the PLA and RMS traces corresponds to a sharp minimum in the ΔP_{Rotor} trace and a maximum in

the ΔP_{Stator} one. Regarding the trailing edge the peak appears in the rotor trace at around 1.55, whereas for the stator it is not really possible to come to a conclusion: no real negative peak is shown in the ΔP_{Stator} trace.

Concerning the boundaries of the stall cell across the stator blade row the averaged values can provide very few informations: only the leading edge can be defined with the pressure difference. On the other hand the wavelet transformation of the stator outlet can provide an idea: the stall cell is where the BPF does not appear, by comparison with the other wavelets the cell seem to propagate with approximately the same circumferential extension as in the rotor (see Figures 4.35, 4.36, 4.37).

Also in this case additional measurements at the stator outlet would be useful to complete the stall cell description.

4.5. Conclusions

The Dream compressor stage reports a stall inception pattern which varies with the rotational speed and the presence of rotating stall in the post-stall behavior.

As foreseen in the characterization of the stable operating points, the stage seem to show a hub corner stall which develops until occupying the whole blade passage at the flow breakdown. The loading of the stage is such to allow the development of instabilities which are attributed to modal waves. They intensify their activity at the lowering of the rotational speed.

The variations encountered in the stall inception patterns are not only due to the intensification of the modal waves activity which typically appear while lowering the rotational speed, but also to the presence of a low frequency modulation at approximately 5 Hz. Indeed in the low speed range the modal waves appear to be at first modulated by a low frequency component, then continuous.

The modulation is attributed to an acoustic mode of the facility, however its nature still has to be completely defined.

The detection of the 5 Hz component points out the necessity of a different experimental set-up: several sensors should be aligned in each of the two directions (axial and circumferential) in order to distinguish the propagation direction. This would simplify the description of the unstable range of any machine, e.g. the detection of stall cells or surge.

The peculiarity of the Dream compressor stage is that it shows a second stability zone for one of the speed lines investigated (80% Nn), similarly to what is sometimes observed in centrifugal compressors. This pattern appears with a higher negative slope before the flow breakdown, and with a tip separation.

The post-stall behavior is characterized by the presence of rotating stall, with only one stall cell at all the rotational speeds investigated. The stall cell rotates at approximately 20% of the shaft speed and occupies approximately

50% of the annulus. The stall cell axially extends from the rotor inlet to the stator outlet. On the rotor it appears to be skewed towards the outlet. At the rotor outlet the cell presents a full span separation, whereas at the inlet it is remarked the presence of defined flow structures visible in the spectrum.

The flow field in the stall cell appears to contain one of the components of the rotating instabilities visible in the stable conditions. The presence of these structures has already been identified in the literature in unstable conditions, however they have never been associated to tornado like vortices.

Additional measurements would be required at the rotor inlet and at the stator outlet in order to provide the accurate description not only of the stall cell, but also of the flow reorganization presented in the case 80% Nn. The contribution of the stator in both the stall inception mechanism and the post-stall behavior remains indeed partially unclear.

Chapter 5.

Conclusions and Perspectives

5.1. Conclusions

The first objective of this work was to provide a deep understanding on the unstable range of a state-of-the-art booster.

The one and half Dream compressor stage has been characterized in details.

The unsteady flow structures appearing in the stable range have been identified and their evolution has been tracked in order to understand the origin of the stall inception and the structure of the rotating stall cell. The stage appears to be hub loaded, and the stall inception seem to derive from a hub corner separation. The tip leakage flows always remain confined within the blade passage in stable conditions. The presence of rotating instabilities seem to affect the stable range and one of their components to appear also in the rotating stall cell.

The stall inception has been described for different speed lines. The peculiarity of this stage is to present different stall inception patterns for almost all the speed lines investigated. It is indeed shown to be abrupt at high speed (100, 96% Nn), whereas the low speed range seems to be dominated by the presence of modal waves, which appear at first modulated by an acoustic mode of the facility and then continuous. The speed line at 80% Nn exhibits a sadle type characteristic, corresponding to the reorganization of the flow field, similarly to what happens in centrifugal compressors. This feature represents a peculiarity of this stage, as it is rarely retrieved in axial compressor stages.

The post-stall behavior is also defined: the Dream compressor stage presents only one stall cell, rotating at approximately 20% of the shaft speed and occupying the 50% of the annulus for all the rotational speeds investigated. The shape of the stall cell is analyzed: it appears to be skewed in the axial direction and to present a full span separation at the rotor outlet, whereas defined flow structures, associated to the rotating instabilities mechanism, dominate the rotor inlet. These structures are assumed to be due to tornado like vortices.

The second objective of the present thesis was to contribute to the im-

provement of the design of new engines.

The analysis of the flow field in different operating conditions of a state-of-the-art booster allows to have a better understanding on this stage design.

The hub loading of the stage results to be advantageous to delay the stall inception: rotating stall is favoured at partial speed in the low pressure compressor, thus the booster represents the limiting component of the engine in the low speed range. In the Dream compressor stage the presence of modal waves in the low regimes mitigates this hindrance, in fact they appear hundreds of revolutions before the stall inception, leaving the time to employ any kind of control to prevent the formation of rotating stall.

In an axial compressor stage the rotor is often the first component to stall, however a high degree of reaction emphasizes this tendency, as in the case of the Dream compressor stage. The higher loading on the rotor indeed enhances the possibility to make it stall first.

The high degree of reaction does not seem to leave a wide margin to increase the stage loading by reducing the blade number. The loading is indeed responsible for the formation of unsteady flow structures, such as the hub corner separation, which represents an important source of losses already in this configuration. The presence of a supersonic pocket indicates that a higher loading of the rotor blade row would translate in a supersonic configuration, whose effectiveness on a booster stage is questionable. The aim of a booster is in fact to provide uniform flow conditions in the spanwise direction. A reduction of the degree of reaction is therefore envisaged for this scope. A solution to maintain the high degree of reaction while increasing the loading is a higher rotational speed of the rotor blade row. This alternative would be in line with the utilization of a gearbox, decoupling the fan from the booster, which represents a tendency of the last years. In this configuration the presence of shocks in the tip region has to be considered.

The utilization of NLH simulations for the characterization of the single blade rows with time-averaged quantities has shown comparable outcomes with respect to RANS simulations in the Dream compressor stage. This result suggests the application of unsteady simulations (URANS) in order to properly detect the presence of the unsteady flow structures responsible for the losses.

The analysis of the Dream compressor stage reveals the lack of measurements not only for the complete characterization of various phenomena, but also for an appropriate use of the instrumentation.

The dynamic calibration of fast-response pressure probes and sensors results to be fundamental for their appropriate utilization. The definition of their bandwidth represents indeed a basic knowledge for the detection of the flow field in a turbomachinery facility.

A “shielded” fast response pressure probe, such as the one employed,

proves not to be suitable for virtual-three hole mode application: the probe-flow field interaction is likely to limit the probe bandwidth, resulting in a not satisfactory reconstruction of the flow field topology.

In the detection of the stable operating points the blade row periodicity appears to impact on the probes or sensors location: a distance equal to a rotor blade pitch between the different sensors allows to perform phase averages without applying any time shift to the signals. On the other hand this configuration presents the drawback of being influenced by the presence of the stator wakes, therefore a stator pitch periodicity is favored.

The stall inception and its time evolution results to be influenced by the system when the characterization is performed by continuously closing the throttling valve.

Axial or circumferential motions across the machine can only be detected with sensors aligned in the direction of motion. An appropriate set-up for the determination of the post-stall behavior should be comprehensive of several sensors aligned in both the axial and the tangential direction, in order to distinguish surge and rotating stall. This configuration would also be beneficial for the characterization of other unsteady phenomena in the stable regime such as rotating instabilities.

Most of the times these obstacles have been overcome by the post-processing techniques applied for the characterization of the different phenomena, however their detection is always preferable with an appropriate experimental set-up, targeted to the specific event.

Last, this work represents a contribution to the literature, which shows a lack in the characterization of low-pressure compressors for aeronautical applications. This case presents also some peculiarities: first of all different stall inception patterns at the different rotational speeds, then the sadle type characteristic for one of the rotational speeds, which corresponds to a flow reorganization in the low speed range. It has to be highlighted also the presence of defined flow structures in the rotating stall cell, which is attributed to the rotating instabilities mechanism, together to the tornado like vortex flow structure.

5.2. Future perspectives

The analysis of the flow field shows that a possibility to improve the performance of a stage of this kind is to apply a hub contouring in the rotor blade row, allowing the extension of the stable range. The hub contouring consists in a local concave flow path capable of increasing the diffusion in the front part of the blade, and thus reducing the development of the hub corner separation.

A possibility to increase the blade loading by reducing the blade number,

in a high degree of reaction configuration, is to extend the chord. In this view, if the hub loading distribution is maintained, the hub contouring application may also represent a recommendable solution.

The design correlations and analysis tools to be employed in the new designs should be achieved with a data set based on the remarks on the experimental set-up presented in the previous paragraph. Some suggestions on their application are reported hereunder.

The use of cylindrical probes with a protected sensor is suggested for the application in virtual-three-hole mode. The shape of the probe is also likely to influence the study of the flow field within the stall cell, and a wide range of incidences (including the reversed flow condition) has to be taken into account in the choice of the probe.

The complete analysis of the stable operating range is comprehensive of rotor/stator interactions, which require the circumferential description of the stage. This is possible with the motion of either the probe or the one of the fixed blade row(s), and has to cover at least one rotor plus one stator pitch, although the stage periodicity is preferable. Therefore the rotor/stator interaction characterization can be simplified by a small periodicity of the machine.

The stall cell description results to be complete if several sensors cover the whole annulus and are located at different radial locations, at a corresponding axial position. The number of stall cells in fact can be detected by a number of sensors which are shifted in the azimuthal direction by a consecutive different angle and are located at the same axial coordinate. A radial distribution of sensors is useful for the radial description of the stall cell structure.

The presence of several sensors at a corresponding axial location is found to be useful also for the characterization of the rotating instabilities which typically appear in the stable range of a compressor. The higher the spatial resolution around the annulus, the higher the number of circumferential modes that can be detected. The angular speed of the rotating instabilities can also be calculated with this configuration. Their description is completed by the presence of sensors in the moving frame, placed in order to compute both the relative and the absolute speeds of these flow structures.

The investigation of the experimental data of the Dream compressor stage can be employed for a better use of aerodynamic analysis tools such as CFD numerical simulations and the mechanical design of new machines.

First of all the measurements can provide the inlet and outlet boundary conditions to the test section, which can be utilized in numerical CFD simulations. The data are available with the rakes measurements on the five speed lines investigated at all the operating points. The data though are time-averaged on a period of 0.5 s and their utilization is recommended only in the stable range, reaching the stability limit. The rakes dispose of

six heads for the radial profile description. More refined measurements are available with pressure probes and thermocouples radial traverses, which describe the flow span distribution on more than 20 points. The traverses have the advantage of a higher spanwise definition, though are available only at maximum mass flow, design and near stall condition at 90, 96 and 100% Nn.

The time-resolved acquisitions in the unstable range result to be helpful regarding the period to consider in the unsteady simulations at the stability limit. At high rotational speed they define the period to enter the stable condition of rotating stall (i.e. with fluctuations of constant amplitude). In the low speed range they could show the time the machine needs to develop modal waves. However the measurements are performed by continuously closing the throttling valve. The description of the evolution from the stable to the unstable condition is thus affected by the changing conditions of the facility, making this indication not reliable.

The presence of rotating instabilities in the stable range suggests the application of full annulus simulations for their appropriate characterization. The domain has to be chosen according to the extension of these phenomena around the annulus, however a small machine periodicity results to be not only more appealing in terms of computational cost, but it would also simplify the stage characterization in terms of rotor/stator interactions. The use of unsteady simulations would be advantageous for the study of the latter, and would enable the appropriate comparison with the time-resolved experimental data.

The mechanical design can benefit from the analysis of the time-resolved pressure measurements. The evolution from the stable to the unstable operating points indeed allows to provide an overview on the possible stresses appearing in the stage, and to identify which are the most critical on the mechanical point of view.

The outcome of this project also suggests some improvements to the VKI-R4 facility.

The stage performance appears to be affected by the elbow at the inlet of the test-section. The bending of the inlet channel indeed produces additional losses in the tip region. A better design of the test section should be applied in order to limit them, for example by employing a test section characterized by an inlet straight channel.

The facility seems to propagate an acoustic mode at certain flow conditions. Indeed the frequency modulating the modal waves at the stall inception in the low speed range appears to correspond to the reservoir Helmholtz frequency. Therefore a first improvement would be done by monitoring the flow field in the whole facility by applying pressure and temperature measurements at different locations. Second the inlet tank can be redesigned by taking into account its resonance frequency. To this aim a theoretical model, such as the Moore-Greitzer one, could be employed. A further amelioration

could be the volume variation of the inlet reservoir. This would allow the testing of compressors not only in stall but also in surge conditions. A model of the facility based on the Moore-Greitzer theory already exists and could be utilized.

Appendices

Appendix A.

Uncertainty calculation method

The ASME uncertainty analysis method [104] is favored over the ISO method [105]. The two techniques mentioned yield the same values, while differing in the way various uncertainty terms are grouped. The ASME method is advantageous in traceability of associated uncertainty terms, categorizing them into systematic and random sources. The ISO method categorizes uncertainty terms into two categories –type A and B– based on the availability of statistical data for calculating standard deviation, which may be more favorable from a statistician's point of view. Dieck [106] states that, "Measurement uncertainty analysis is a function of the measurement system. It is therefore necessary to completely define the measurement system before proceeding with an uncertainty analysis."

Error sources may be treated as either random (precision) or systematic (bias). Random error sources cause scatter in the test results, affecting the data in a random fashion while systematic errors do not, and remain the same during the experiment. It is crucial to distinguish between the errors and uncertainties. While the term *error* defines the difference between the true and the measured value and remains unknown, the term *uncertainty* is defined as an estimate of the error limits within a confidence interval. The error is therefore never known, since the true value is a priori unknown.

Systematic errors are estimated either as tolerances specified by manufacturers or as the calculated calibration uncertainty of the instrument used. In case there are various systematic error sources denoted by b_i, these can be combined as $b = (\sum b_i^2)^{\frac{1}{2}}$. On the other hand, random errors are estimated as the standard deviation of the average.

It is imperative to understand that within the context of measurement uncertainties, that data set in hand should fit a normal or Gaussian distribution, which is sometimes informally called as a *bell curve*. For a normal distribution, the 68-95-99.7 rule (or three-sigma rule) is applicable. According to the three-sigma rule, approximately 68.27% of the values lie within a standard deviation (σ_X) of the mean (μ), while approximately 95.45% and 99.72% of the values lie within two- and three-sigma range respectively.

The standard deviation (σ_X), defining the scatter of individual values (X_i) around their mean value (μ) for a normal distribution with an infinite population is defined as given in eq. (A.1). As a real measurement data set is always of finite length, i.e. consisting of a sample of N points, it is impossible to calculate the actual standard deviation. However for the data set sampled

from a normal distribution, one may define *sample standard deviation* (s_X) as an estimate of the actual value, used to estimate the limits of random error (ϵ), where $\overline{X}$ denotes the population average.

$$\sigma_X = \lim_{N\to\infty} \sqrt{\frac{\sum_{i=1}^{N}(X_i-\mu)^2}{N}} \qquad s_X = \sqrt{\frac{\sum_{i=1}^{N}(X_i-\overline{X})^2}{N-1}} \tag{A.1}$$

In order to estimate the random uncertainty, the term *random standard uncertainty* ($s_{\overline{X}}$), defined as $s_{\overline{X}} = s_X/\sqrt{N}$, is used which may be interpreted as the standard deviation of the average. The number of samples in random standard uncertainty may be different than that of sample standard deviation (e.g. $N_{\text{cal}} > N_{\text{measurement}}$ where number of samples used to calibrate is greater than the number of actual measurements).

In cases where quality of a data fit denoted with $\mathbb{M}$ is considered instead of quality of an average such as for a calibration curve, the *standard estimate of error*, defined in eq. (A.2), is used in lieu of the *sample standard deviation*. In this case, the random uncertainty is estimated using $s_{\overline{\mathbb{M}}}$. In eq. (A.2), $\mathbb{M}_i$ denotes the measured point, $\mathbb{M}_{fit,i}$ stands for the value calculated from the data fit, N represents the number of points and finally K denotes the number of coefficients used for the data fit (e.g. 2 for a straight line). The term $N-K$ represents the degrees of freedom of the random uncertainty source $\mathbb{M}$.

$$SEE_{\mathbb{M}} = \sqrt{\frac{\sum_{i=1}^{N}(\mathbb{M}_i-\mathbb{M}_{fit,i})^2}{N-K}} \qquad s_{\overline{\mathbb{M}}} = \frac{SEE_{\mathbb{M}}}{\sqrt{N}} \tag{A.2}$$

Once the systematic and random uncertainty terms are obtained, the *total uncertainty* may be calculated as given in eq. (A.3), which does not include any confidence interval. On the other hand, the *expanded uncertainty* for 95% confidence interval (i.e. 2σ) is calculated as given in eq. (A.4), where $t_{95}(\nu)$ denotes the appropriate value of the two-sided *t-distribution* for 95% confidence interval.

$$U_T = \sqrt{\sum_{i=1}^{M_b}(b_i^2) + \sum_{i=1}^{M_s}(s_{\overline{X}_i}^2)} \tag{A.3}$$

$$U_{95} = \pm t_{95}(\nu) \times \sqrt{\sum_{i=1}^{M_b}(b_i^2) + \sum_{i=1}^{M_s}(s_{\overline{X}_i}^2)} \tag{A.4}$$

In order to determine the $t_{95}(\nu)$ value required to compute expanded uncertainty, the combined degrees of freedom (ν) must be computed using the Welch-Satterthwaite equation, given in eq. (A.5). In short, Welch-Satterthwaite equation combines the degrees of freedoms of systematic and

random uncertainty sources (ν_i). The degrees of freedom for systematic uncertainty sources (b_i), such as those of reference instruments, may either be known a priori as in the case of a complete calibration certificate, or may be assumed to be infinity in case no information is provided. On the other hand, the degrees of freedom for random uncertainty terms ($s_{\overline{X}_i}$) are determined by subtracting the number of coefficients used for the data fit from the sample size, as explained above ($N - K$) and shown in eq. (A.2).

$$\nu = \frac{\left[\sum_{i=1}^{Ms}(s_{\overline{X}_i})^2 + \sum_{i=1}^{Mb}(b_i)^2\right]^2}{\left[\sum_{i=1}^{Ms}\frac{(s_{\overline{X}_i})^4}{\nu_i} + \sum_{i=1}^{Mb}\frac{(b_i)^4}{\nu_i}\right]} \tag{A.5}$$

Once the Welch-Satterthwaite equation is solved, the value is truncated in order to determine the degrees of freedom for the combined system. Following this step, the appropriate value of t_{95} may be found using two-sided t-distribution table for 95% confidence interval typically found in statistics books (it may also be found on-line from NIST[107]), which is plotted in Figure A.1. It is noteworthy to mention that the t_{95} value for 99.5% confidence interval for infinite degrees of freedom is 1.96, while as seen in Figure A.1, the asymptotic distribution reaches a value of 2 with only 30 degrees of freedom. If a different confidence interval is desired (e.g. 99.5% or 3σ), one may simply use the same combined degrees of freedom and choose the appropriate t-distribution table.

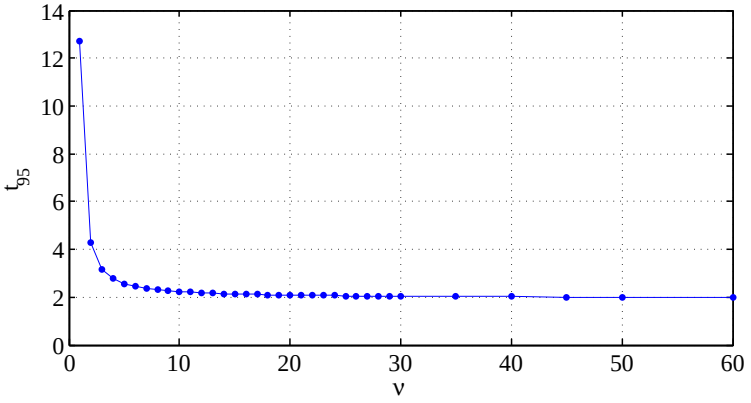


Figure A.1.: Student's t distribution for 95% confidence interval with respect to degrees of freedom.

If the quantity of interest (e.g. $A = f(a, b, c)$) is not directly measured but derived from other measured quantities (e.g. a, b, c), the uncertainty values for the measured quantities need to be propagated in order to estimate the uncertainty on the desired quantity. A Taylor series expansion is used for

this purpose as shown in eq. (A.6). The correlated terms are not present when uncertainty sources are independent, and will not be discussed in this paper. Correlated uncertainties are explained in detail by Dieck [106].

$$b_A = \sqrt{\left(\frac{\partial A}{\partial a}\delta a\right)^2 + \left(\frac{\partial A}{\partial b}\delta b\right)^2 + \left(\frac{\partial A}{\partial c}\delta c\right)^2 + \text{correlated terms}} \tag{A.6}$$

Appendix B.

Post-processing techniques

B.1. Phase-locked average

The phase locked average (PLA) technique is employed for the characterization of both the stable and the unstable operating points, enabling the representation of the typical averaged phenomenon.

The PLA technique utilized in this work considers the effective measurements: the number of classes is always lower than the number of points sampled in the period, allowing to perform a statistical analysis and thus the computation of the uncertainty with the ASME method.

The choice of the number of classes is presented for the representation of the typical blade passage retrieved with the fast response pressure probe at the rotor outlet, as well as the uncertainty calculation on the related phase locked average.

Phase-locked averaging the typical blade passage can be either performed with a once-per-blade signal, such as in the presence of a tip-timing sensor, or with a once-per-revolution signal and dividing it into the number of blade passages in a row.

In this case the signal is first divided according to the revolutions detected using the once-per-revolution signal as explained above and then into blade passages. After the number of classes is selected, typically of the same order as the number of points contained within a period (a blade passage for phase-locked average), the data points contained in each class are averaged as shown in Figure B.1. For this particular measurement campaign, number of classes is chosen between 85 and 90 per blade passage according to the acquisition, to guarantee the existence of at least one point per class in the raw signal ($300,000$ samples/(# of revs$\times$# of blades) ~ 90) yielding a total of approximately 6840 classes used for averaging.

The class length represents a higher frequency than the bandwidth of the sensors, though it has been verified that the result is able to provide a correct representation of the blade passage. A sensitivity analysis on the number of points adopted has been performed and it is shown in Figure B.2 for the total pressure signal at the rotor outlet at midspan.

The pressure RMS value is calculated for each of the classes using the formulation given in eq. (B.1), where N represents the number of points used for calculating one value over both the PLA and the P_{RMS} map ($\sim$#

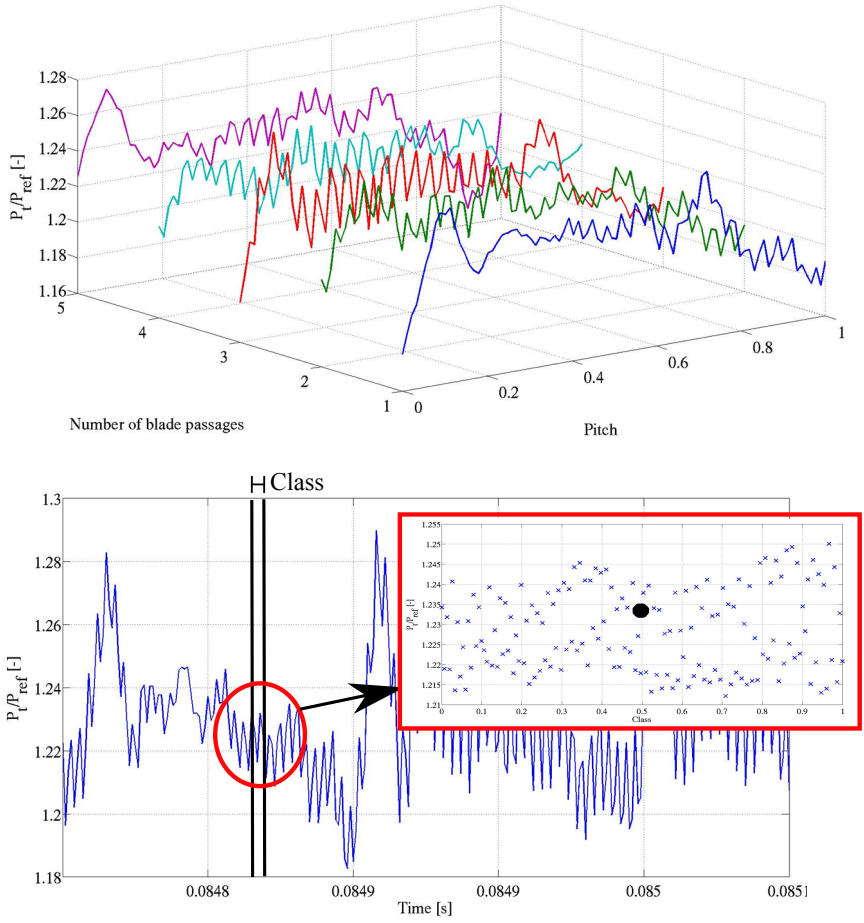


Figure B.1.: Top: Division of the pressure data in blade passages. Bottom: the PLA calculated value for one class in a blade passage.

of revs × # blade passages = 42×76 =∼ 3192), P_i represents the acquired pressure data and finally $\overline{P}$ denotes the averaged value corresponding to the particular class.

$$RMS = \sqrt{\frac{\sum_{i=1}^{N}(P_i - \overline{P})^2}{N}} \tag{B.1}$$

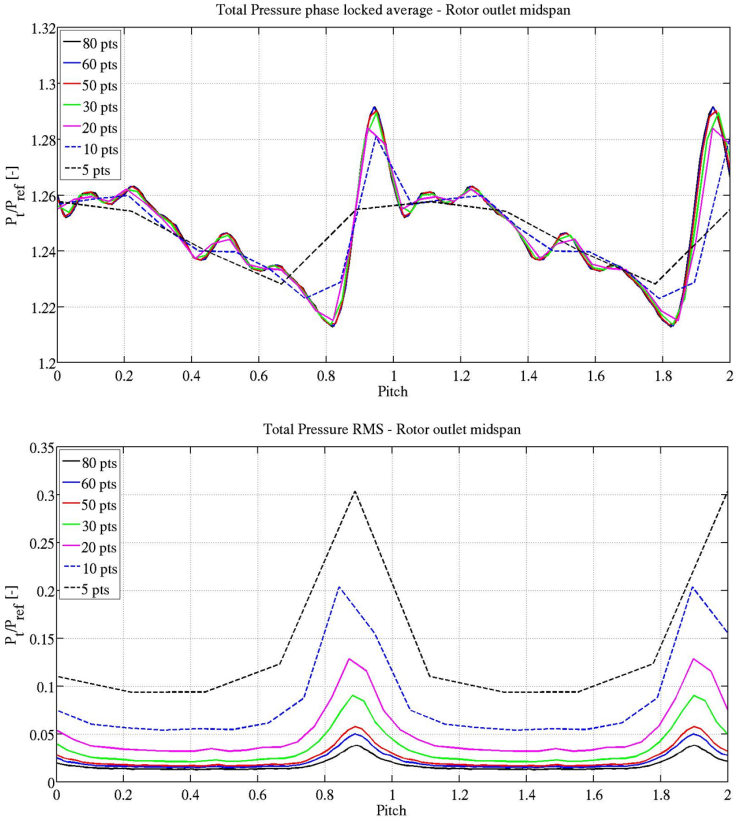


Figure B.2.: Phase locked average and corresponding RMS variation for different number of classes employed across a blade passage.

Bibliography

[1] A.F. Kurzke. Preliminary design. VKI-LS 2013-04 "Aeroengine design: from state of the art of turbofans towards innovative architectures", Rhode-Saint-Genese, Belgium, April 2013. xi, 2

[2] I.J. Day. The fundamentals of stall and surge - part 1: Stall. VKI-LS 2006-06 on "The fundamentals of stall and surge", Rhode-Saint-Genese, Belgium, October 2006. xi, xii, 2, 3, 18, 23, 28

[3] Rolls Royce plc. *The jet engine*. ISBN 0 902121 2 35. Rolls Royce printer, fifth edition 1996. xi, 5, 6

[4] G. Paniagua. Flow in turbomachinery. VKI Course Notes on "Flow in turbomachinery", Rhode-Saint-Genese, Belgium, October 2012. xi, 5, 6

[5] S.L. Dixon. *Fluid mechanics, Thermodynamics of turbomachinery*. ISBN 0 7506 7059 2. Planta Tree, fourth edition 1966. xi, 7

[6] M.H. Vavra. *Aero-thermodynamics and flow in turbomachines*. R.E. Krieger Publishing Co, 1960. xi, 9, 10

[7] G.T. Chen, E.M. Greitzer, C.S. Tan, and F.E. Marble. Similarity analysis of compressor tip clearance flow structure. *Journal of turbomachinery*, 113(2):260–271, 1991. xi, 9, 10

[8] J. Marz, C. Hah, and W. Neise. An experimental and numerical investigation into the mechanisms of rotating instability. *Journal of turbomachinery*, 124(3):367–375, 2002. xi, 9, 10, 15

[9] S.A. Gbadebo, N.A. Cumpsty, and T.P. Hynes. Three-dimensional separations in axial compressors. *Journal of Turbomachinery*, 127(2):331–339, 2005. xi, 9, 11

[10] H.S. Schultz and H.D. Gallus. Experimental investigation of the three-dimensional flow in an annular compressor cascade. *Journal of Turbomachinery*, 110(4):467–478, 2008. xi, 11

[11] R. Mailach, I. Lehmann, and K. Voegeler. Rotating instabilities in an axial compressor originating from the fluctuating blade tip vortex. *Journal of turbomachinery*, 123(3):453–461, 2001. xi, 12, 13

[12] B. Pardowitz, U. Tapken, R. Sorge, P.U. Thamsen, and L. Enghardt. Rotating instabilitiy in an annular cascade: detailed analysis of the instationary flow phenomena. *Journal of turbomachinery*, 136(3):061017–1–10, 2014. xi, 13, 14, 15, 86

[13] B. Pardowitz, A. Moreau, U. Tapken, and L. Enghardt. Experimental identification of rotating instabilitiy of an axial fan with shrouded rotor. *Journal of power and energy*, 229(5):520–528, 2015. xi, 13, 14, 15, 88

[14] M. Inoue, M. Kouroumaru, T. Tanino, and M. Furukawa. Propagation of multiple short-length-scale stall cells in an axial compressor rotor. *Journal of turbomachinery*, 106(1):45–54, 2000. xi, xvii, 15, 16, 129, 130

[15] M. Inoue, M. Kouroumaru, S. Yoshida, and M. Furukawa. Short and long length-scale disturbances leading to rotating stall in an axial compressor stage with different stator/rotor gaps. *Journal of turbomachinery*, 124(3):376–384, 2002. xi, 15, 16, 17, 21

[16] I.J. Day. Stall inception in axial flow compressors. *Journal of turbomachinery*, 115(1):1–9, 1993. xi, xii, 9, 17, 21, 23, 107, 108

[17] A.H. Stenning. Rotating stall and surge. *Journal of fluids engineering*, 102(1):14–20, 1980. xi, 17, 22, 27

[18] I.J. Day and N.A. Cumpsty. The measurement and interpretation of flow within rotating stall cells in axial compressors. *Journal of mechanical engineering science*, 20:101–114, 1970. xi, xii, 18, 23, 24, 25

[19] T.R. Camp and I.J. Day. Study of spike and modal stall phenomena in a low-speed axial compressor. *Journal of turbomachinery*, 120(3):393–401, 1998. xi, 19, 105, 108

[20] S. Weichert and I.J. Day. Detailed measurement of spike formation in an axial compressor. *Journal of turbomachinery*, 136(5):051006–1–9, 2014. xii, 10, 20, 21

[21] G. Pullan, A.M. Young, I.J. Day, E.M. Greitzer, and Z.S. Spakovszky. Origins and structure of spike-type rotating stall. In *ASME Turbo Expo, Paper GT2012-68707*, Copenhagen, Denmark, Jun. 11th - 15th 2012. xii, 10, 20, 21

[22] V.H. Garnier and A.H. Epstein and E.M. Greitzer. Rotating waves as a stall inception indication in axial compressors. *Journal of Turbomachinery*, 113(1):290–302, 1991. xii, 22, 23, 102

[23] N. A. Cumpsty and E.M. Greitzer. A simple model for compressor stall cell propagation. *Journal of engineering for power*, 104(1):170–176, 1982. xii, 25, 124, 133

[24] K.Mathioudakis and F.A. Breugelmans. Three-dimensional flow in deep rotating stall cells of an axial compressors. *Journal of propulsion*, 4(3):263–269, 1988. xii, 25, 26, 124

[25] E.M. Greitzer. Surge and rotating stall in axial flow compressor - part2: Experimental results and comparison with theory. *Journal of engineering for power*, 98(2):190–198, 1978. xii, 27, 28

[26] J.D. Paduano, E.M. Greitzer, and A.H. Epstein. Compression system stability and active control. *Fluid Mechanics*, 33:491–517, 2001. xii, 28

[27] O.H. Unalmis, N.T. Clemens, and D.S. Dolling. Cavity oscillation mechanisms in high speed flows. *AIAA Journal*, 42(10):2035–2041, 2004. xiii, 51, 52

[28] W. F. Ng and A.H. Epstein. Unsteady losses in transonic compressors. *Journal of Engineering for Gas Turbine and Power*, 107(3):345–353, 1985. xiv, 80

[29] C. Hah, M. Hathaway, and J. Katz. Investigation of unsteady flow field in a low-speed one and a half stage axial compressor, part 2: Effects of the tip gap size on the tip clearance flow structure at near stall operation. In *ASME Turbo Expo, Paper GT2014-27094*, Dusseldorf, Germany, Jun. 16th - 20th 2014. xv, 84, 86

[30] Cleansky, www.cleansky.eu/content/homepage/aviation-environment. Online. Last Checked October 2016. 1

[31] Paris agreement, ec.europa.eu/clima/policies/strategies/2020. Online. Last Checked October 2016. 1

[32] Acare, www.acare4europe.org/documents/acare-annual-report. Online. Last Checked October 2016. 1

[33] J.D. Denton. Some limitations of turbomachinery cfd. In *ASME Turbo Expo, Paper GT2010-22540*, Glasgow, U.K., Jun. 14th - 18th 2010. 2

[34] I. Day. Stall, surge, and 75 years of research. *Journal of turbomachinery*, 138(1):011001–1–16, 2015. 2

[35] Fp7 dream european project, ec.europa.eu/research/transport/projects/items/dream-en.htm. Online. Last Checked February 2012. 3

[36] N.H.S. Smith. The aerodynamic design of the lpc system. VKI-LS 2013-04 "Aeroengine design: from state of the art of turbofans towards innovative architectures", Rhode-Saint-Genese, Belgium, April 2013. 8

[37] S. Hiernaux, O. deVriendt, J.-F. Brouckaert, and I. Lepot. Next generation boosters. In *Proceedings of the 18th ISABE Conference*, Beijing, China, 2007. 8, 11

[38] J. Sans, M. Resmini, J.-F. Brouckaert, and S. Hiernaux. Numerical investigation of the solidity effect on linear compressor cascade. In *ASME Turbo Expo, Paper GT2014-25532*, Dusseldorf, Germany, Jun. 16th - 20th 2014. 9

[39] Nicolas Van de Wyer. *Experimental study of the performance and stability of a low pressure axial compressor for a contra-rotating turbofan engine architecture.* PhD thesis, Universite catholique de Louvain, 2012. 9, 18

[40] F.Sh. Gelmedov, V.I. Mileshin, P.G. Kozhemyako, and I.K. Orekhov. Stall margin improvement in three-stage low pressure compressor by use of slot type casing treatments. In *ASME Turbo Expo, Paper GT2014-26298*, Dusseldorf, Germany, Jun. 16th - 20th 2014. 9

[41] N.M.McDougall, N.A. Cumpsty, and T.P. Hynes. Stall inception in axial compressors. *Journal of Turbomachinery*, 112(1):116–125, 1990. 9, 11, 21, 22, 23, 102, 107, 108, 111

[42] J.A. Storer and N. Cumpsty. Tip leakage flow in axial compressors. *Journal of turbomachinery*, 113(2):252–259, 1991. 9, 20

[43] H. Saathoff and U. Stark. Tip clearance flow induced endwall boundary layer separation in a single-stage axial-flow low-speed compressor. In *ASME Turbo Expo, Paper 2000-GT-0501*, Munich, Germany, 8-11th May 2000. 9

[44] D.A. Hoying, C.S. Tan, H.D. Vo, and E.M. Greitzer. Role of the blade passage flow structures in axial compressor rotating stall inception. *Journal of turbomachinery*, 121(4):735–742, 1999. 10, 21

[45] Y. Dong, S.J. Gallimore, and H.P. Hodson. Three-dimensional flows and loss reduction in axial compressors. *Journal of Turbomachinery*, 109(3):354–361, 1987. 10

[46] J.V. Taylor and R.J. Miller. Competing 3d mechanisms in compressor flows. In *ASME Turbo Expo, Paper GT2015-43322*, Montreal, Canada, Jun. 15th - 19th 2015. 11, 12

[47] S.A. Gbadebo, N.A. Cumpsty, and T.P. Hynes. Control of three-dimensional separations in axial compressors by tailored boundary layer suction. *Journal of Turbomachinery*, 130(1):011004–1–8, 2008. 11

[48] Arnaud Naert. Experimental investigation on the possibility of enhancing the aerodynamic performance of a compressor cascade via bleed off-takes. Master's thesis, TU Delft, 2012. 11

[49] Antoine Godard. *Etude numerique et experimentale d'un compresseur aspire*. PhD thesis, Ecole centrale de Lyon, 2010. 11

[50] W. Ma, X. Ottavy, L. Lu, and F. Leboeuf. Intermittent corner separation in a linear compressor cascade. *Experiments in fluids*, page 54:1546, 2013. 12

[51] G. Zambonini and X. Ottavy. Unsteady pressure investigations of corner separated flow in a linear compressor cascade. In *ASME Turbo Expo, Paper GT2015-42073*, Montreal, Canada, Jun. 15th - 19th 2015. 12, 76

[52] K. Mathioudakis and F.A.E. Breugelmans. Development of small rotating stall in a single stage axial compressor. In *ASME Turbo Expo, Paper 85-GT-227*, Atlanta, Georgia, U.S., Jun. 16th - 19th 1985. 12

[53] F. Kamaier and W. Neise. Experimental study of tip clearance losses and noise in axial turbomachines and their reduction. *Journal of turbomachinery*, 119(3):460–471, 1997. 13, 15

[54] F. Kamaier and W. Neise. Rotating blade flow instability as a source of noise in axial turbomachines. *Journal of sound and vibration*, 203(5):833–853, 1997. 13, 15, 86

[55] H.D. Vo. Role of tip clearance flow in rotating instabilitiies and nonsynchronous vibrations. *Journal of propulsion and power*, 26(3):556–561, 2010. 13

[56] H. Wang, Y. Wu, H. Ouyang, J. Tian, and Z. Du. Investigations of rotating instability and fluctuating tip clearance flow in a low-speed axial compressor. *Journal of aerospace engineering*, 230(6):981–994, 2015. 13, 15, 86

[57] H.W. Emmons, C.E. Pearson, and H.P. Grant. Compressor surge and stall propagation. *ASME transactions*, 77:455–469, 1955. 17, 27

[58] E. Poursaeidi, M.R. Mohammadi Arhani, S. Hosseini, M. Darayi, and M. Arablu. Partial stall effects on the failure of an axial compressor blade. *Journal of engineering for gas turbine and power*, 137(1):122602–1–6, 2015. 18

[59] R. Mailach and K. Voegeler. Unsteady aerodynamic blade excitation at the stability limit and during rotating stall in an axial compressor. *Journal of turbomachinery*, 129(4):503–511, 2007. 18

[60] A.D. Jackson. Stall cell development in an axial compressor. *Journal of turbomachinery*, 109(4):492–498, 1987. 18, 19, 26

[61] N. Courtiade and X. Ottavy. Experimental study of surge precursors in a high-speed multistage compressor. *Journal of turbomachinery*, 135(6):061018–1–9, 2013. 18

[62] Nicolas Courtiade. *Experimental analysis of the unsteady flow and instabilities in a high-speed multistage compressor*. PhD thesis, Ecole centrale de Lyon, 2012. 18, 82

[63] Nicolas Gourdain. *Simulation numerique des phenomenes de decollement tournant dans les compresseurs axiaux*. PhD thesis, Ecole Centrale de Lyon, 2005. 18

[64] F. Crevel, N. Gourdain, and S. Moreau. Numerical simulation of aerodynamic instabilities in a multistage high-speed high-pressure compressor on its test-rig - part1: Rotating stall. *Journal of turbomachinery*, 136(1):101003–1–14, 2014. 18

[65] Flore Crevel. *Simulation numerique de l'ecoulement en regime de pompage dans un compresseur axial multi-etage*. PhD thesis, Ecole Centrale de Lyon, 2012. 18

[66] L. Castillon, N. Gourdain, and X. Ottavy. Unsteady numerical simulations of an experimental axial compressor with a multiple frequency phase lagged approach. In *ISABE 2013-1114*, Busan, Korea, 9-13th September 2013. 18

[67] J. Sans, J. Desset, G. Dell'Era, J.-F. Brouckaert, and S. Hiernaux. Performance testing of a low pressure compressor. In *ETC10*, Lappaeranta, Finland, 15-19th April 2013. 18, 55, 67

[68] I.J. Day and C. Freeman. The unstable behavior of low and high-speed axial compressor. *Journal of turbomachinery*, 116(1):194–201, 1998. 19, 27

[69] K. Yamada, H. Kikuta, K. Iwakiri, and S. Gunjishima. An explanation for flow features of spike-type stall inception in an axial compressor rotor. *Journal of turbomachinery*, 135(2):021023–1–11, 2013. 21

[70] V.-M. Lei, Z.S. Spakovszky, and E.M. Greitzer. A criterion for axial compressor hub-corner stall. *Journal of turbomachinery*, 120(3):031006–1–10, 2008. 21

[71] F.K. Moore and E.M. Greitzer. A theory of post-stall transients in axial compressors - part 1: Development of the equations. *Journal of engineering for gas turbines and power*, 108(1):68–76, 1986. 22, 27

[72] F.K. Moore and E.M. Greitzer. A theory of post-stall transients in axial compressors - part 2: Application. *Journal of engineering for gas turbines and power*, 108(1):231–239, 1986. 22, 27

[73] N. Cumpsty. Casing treatment on part of the circumference and the effect on compressor stall. In *ASME Turbo Expo, Paper 89-GT-312*, Toronto, Canada, Jun. 5th - 8th 1989. 22

[74] J.M.Haynes, G.J. Hendricks, and A.H. Epstein. Active stabilization of rotating stall in a three-stage axial compressor. *Journal of turbomachinery*, 116(2):226–239, 1995. 23

[75] I.J. Day, E.M. Greitzer, and N.A. Cumpsty. Prediction of compressor performance in rotating stall. *Journal of engineering for power*, 100(1):1–14, 1978. 24

[76] H.M. Saxer-Felici, A.P. Saxer, A. Inderbitzin, and G. Gyarmathy. Prediction and measurement of rotating stall cells in an axial compressor. *Journal of turbomachinery*, 121(2):365–375, 1999. 25

[77] D. K. Das and H. K. Jiang. An experimental study of rotating stall in a multistage axial flow compressor. *Journal of engineering for gas turbine and power*, 106(3):542–551, 1984. 25, 124

[78] D. K. Das and H. K. Jiang. Flow measurements within rotating stall cells in single and multistage axial flow compressors. In *6th International Symposium on Air Breathing Engines, Paper 83-7072*, June 1983. 25, 124

[79] I.J. Day. Detailed flow measurements during deep stall in axial flow compressors. In *AGARD cp 177*, 1976. 25, 124

[80] F.A. Breugelmans, K.Mathioudakis, and F. Casalini. Flow in rotating stall cells of a low speed axial flow compressor. In *6th International Symposium on Air Breathing Engines, Paper 83-7073*, June 1983. 25, 124

[81] A.P. Saxer, H.M. Saxer-Felici, F. Ginter, A. Inderbitzin, and G. Gyarmathy. Structure and propagation of rotating stall cells in an axial compressor stage. In *iMechE, 605-618*, 1999. 25

[82] I.J. Day and C. Freeman. The unstable behavior of low and high-speed compressors. *Journal of turbomachinery*, 116(1):194–201, 1994. 27

[83] E.M. Greitzer. Surge and rotating stall in axial flow compressor - part1: Theoretical compression system. *Journal of engineering for power*, 98(2):190–198, 1978. 27

[84] C. H. Sieverding, T. Arts, R. Dénos, and J.-F. Brouckaert. Measurement techniques for unsteady flows in turbomachines. *Experiments in Fluids*, 28:285–321, 2000. 39

[85] R. W. Ainsworth, R. J. Miller, R. W. Moss, and S.J. Thorpe. Unsteady Pressure Measurement. *Meas. Sci. Technol.*, Vol. 11:1055–1076, 2000. 39

[86] M. Mersinligil, J.-F. Brouckaert, and J. Desset. Unsteady pressure measurements with a fast response cooled probe in high temperature environments. *Transactions of the ASME, Journal of Engineering for Gas Turbines and Power*, 133(8):081603, August 2011. 39

[87] W. George, P. Beuther, and R. Arndt. Pressure spectra in turbulent free shear flows. *Journal of Fluid Mechanics*, 148:155–191, 1984. 41

[88] S.W. Rienstra and A. Hirschberg. *An introduction to acoustics.* TU Eindhoven, January 2003. 42

[89] J.M. Tyler and T.G. Sofrin. Axial flow compressor noise studies. *Transac. Soc. Automotive Engrs*, pages 309–332, 1961. 42, 91

[90] H. Griepentrog. Transonic compressor cascades. VKI Course Notes 73, Rhode-Saint-Genese, Belgium, December 1969. 62

[91] *Numeca international - Theoretical manual - FINE/Turbo v9.0.* Numeca international, 2013. 63

[92] W. Ning and L. He. Computation of unsteady flows around oscillating blades using linear and nonlinear harmonic euler methods. *Journal of Turbomachinery*, 120(3):508–514, 1998. 63

[93] N. Pallag. Unsteady numerical analysis of the performance and stability of a low pressure axial compressors. Master's thesis, von Karman Institute for Fluid Dynamics, 2014. 66

[94] A.H. Epstein, J.B. Gertz, P.R. Owen, and M.B. Giles. Vortex shedding in high-speed compressor blade wakes. *Journal of Propulsion and Power*, 4(3):236–244, 1988. 80

[95] J. Sans, G. Dell'Era, J. Desset, J.-F. Brouckaert, and S. Hiernaux. Time resolved measurements of the unsteady flow field in a single stage low pressure axial compressor. In *ASME Turbo Expo 2013, Paper GT2013-94264*, San Antonio, USA, 3-7th June 2013. 81

[96] Y. Wu, Z. Chen, G. An, J. Liu, and G. Yang. Origins and structure of rotating instability - part 1: Experimental and numerical observations in a subsonic axial compressor rotor. In *ASME Turbo Expo, Paper GT2016-56221*, Seoul, South Korea, Jun. 13th - 17th 2016. 88

[97] Y. Wu, G. An, Z. Chen, J. Liu, and G. Yang. Origins and structure of rotating instability - part 1: Numerical observations in a subsonic axial compressor rotor. In *ASME Turbo Expo, Paper GT2016-56223*, Seoul, South Korea, Jun. 13th - 17th 2016. 88

[98] N. Courtiade, X. Ottavy, and N. Gourdain. Modal decomposition for the analysis of the rotor-stator interactions in multi-stage compressors. *Journal of Thermal Science*, 21(3):276–285, 2012. 91

[99] F. Lin and J. Chen. Wavelet analysis of rotor-tip disturbances in an axial flow compressor. *Journal of Propulsion and Power*, 20(2):319–334, 2004. 101

[100] N.G. Diez, J.P.M. Smeulers, L. Tapinassi, A. Scotti del Greco, and L. Toni. Predictability of rotating stall and surge in a centrifugal compressor stage with dynamic simulations. In *ASME Turbo Expo 2014, Paper GT2014-26712*, Dusseldorf, Germany, 16-20th June 2014. 117

[101] R.C. pampreen. *Compressor stall and surge*. Concepts ETI, 1993. 117

[102] Y. Levy and J. Pismenny. The number of stall cells during rotating stall. In *ASME Turbo Expo, Paper GT2003-38221*, Atlanta, Georgia, U.S., Jun. 16th - 19th 2003. 120

[103] G. Dell'Era. Experimental characterization of unsteady flows in a high speed axial compressor. In *7th Symposium of VKI PhD Research*, March 2016. 122

[104] American National Standards Institute and American Society of Mechanical Engineers. *ANSI/ASME PTC 19.1-2005 Measurement Uncertainty*. American Society of Mechanical Engineers, 2006. 145

[105] International Organization for Standardization. *Guide to the expression of uncertainty in measurement, Supported by BIPM, IEC, IFCC, ISO IUPAC, IUPAP and OIML*. International Organization for Standardization, Geneva, 1995. 145

[106] R.H. Dieck. *Measurement uncertainties - methods and applications*. ISA, 2007. 145, 148

[107] Nist atomic spectra database, http://www.nist.gov/pml/data/asd.cfm. Last Checked: 25.05.2015. 147